8-2011

In Situ Preconcentration by AC Electrokinetics for Rapid and Sensitive Nanoparticle Detection

Kai Yang
kyang@utk.edu

To the Graduate Council:

I am submitting herewith a dissertation written by Kai Yang entitled "In Situ Preconcentration by AC Electrokinetics for Rapid and Sensitive Nanoparticle Detection." I have examined the final electronic copy of this dissertation for form and content and recommend that it be accepted in partial fulfillment of the requirements for the degree of Doctor of Philosophy, with a major in Electrical Engineering.

<div style="text-align: right">Jie Wu, Major Professor</div>

We have read this dissertation and recommend its acceptance:

Shigetoshi Eda, Jeremy Holleman, Nicole McFarlane

<div style="text-align: right">Accepted for the Council:</div>

<div style="text-align: right">Carolyn R. Hodges</div>

<div style="text-align: right">Vice Provost and Dean of the Graduate School</div>

(Original signatures are on file with official student records.)

In Situ Preconcentration by AC Electrokinetics

for Rapid and Sensitive Nanoparticle Detection

A Dissertation Presented for the

Doctor of Philosophy

Degree

The University of Tennessee, Knoxville

Kai Yang

August 2011

ACKNOWLEDGEMENTS

ABSTRACT

Reducing cost and time is a major concern in clinical diagnostics. Current molecular diagnostics are multi-step processes that usually take at least several hours or even days to complete multiple reagents delivery, incubations and several washing processes. This highly labor-intensive work and lack of automation could result in reduced reliability and low efficiency. The Laboratory-on-a-chip (LOC), taking advantage of the merger and development of microfluidics and biosensor technology, has shown promise towards a solution for performing analytical tests in a self-contained and compact unit, enabling earlier and decentralized testing. However, challenges are to integrate the fluid regulatory elements on a single platform and to detect target analytes with high sensitivity and selectivity.

The goal of this research work is to develop an AC electrokinetic (ACEK) flow through concentrator for in-situ concentration of biomolecules and develop a comprehensive understanding of effects of ACEK flow on the biomolecule transport (in-situ concentration) and their impact on electronic biosensing mechanism and performance, achieving automation and miniaturization. ACEK is a new and promising technique to manipulate micro/bio-fluids and particles. It has many advantages over other techniques for its low applied voltage, portability and compatibility for integration into lab-on-a-chip devices. Numerical study on preconcentration system design in this work has provided an optimization rule for various biosensor designs using ACEK technique. And the microfluidic immunoassay lab-chip designed based on ACET effect has showed promising prospect for accelerated diagnostics. With

optimized design of channel geometry, electrode patterns, and properly selected operation condition (ac frequency and voltage), the preconcentration system greatly reduced the reaction time to several minutes instead of several hours, and improved sensitivity of the assay. With the design of immunoassay lab-chip, one can quantitatively study the effect of ACET micropumping and mixing on molecular level binding. Improved sensors with single-chip form factor as a general platform could have a significant impact on a wide-range of biochemical detection and disease diagnostics including pathogen/virus detection, whole blood analysis, immune-screening, gene expression, as well as home land security.

TABLE OF CONTENTS

LIST OF FIGURES

Figure 3-1. Mechanisms of AC electroosmosis. (a) AC signal is applied to the electrodes, resulting in the induced charge formation in the double layer and tangential electric field to drive the ions, (b) The interaction of the tangential field at the surface with the induced

Chapter One: Introduction

1.1 Microfluidics and Lab-on-a-chip technology

With its emergence in early 1980s, the research on microfluidics has been carried on for almost 30 years. Microfluidics deals with the behavior, precise control and manipulation of fluids that are geometrically constrained to a small scale, typically sub-millimeter. The fluid sample used in microfluidics is usually in micro or nano-liters. It is a multidisciplinary field intersecting engineering, physics, chemistry, microtechnology, and biotechnology, with practical applications to the design of systems in which very small volumes (pL to μL) of fluids will be used. Microfluidics has many advantages over conventional diagnostic methods, such as decreased reagent consumption and waste generation, reduction of cost per analysis, shorter analyses time, improved data quality, and better controllable processes.

When microfluidics is applied to biotechnology, it is also known as μTAS or lab-on-a-chip (LOC) technology. μTAS stands for Micro Total Analysis System, and refers to a microfluidic device which can perform highly efficient, simultaneous processes or analyses of a large number of biologically important molecules for genomic, proteomic, and metabolic studies. The concept of lab-on-a-chip is to shrink a whole laboratory to chip-size, through the integration of functional units such as pumping, mixing, separation, concentration, and detection systems onto one device in micro scale. Because of its small size, such a system is portable, low cost, and can be placed close to the sampling site for fast analysis and detection.

Reducing cost and time is a major concern in clinical diagnostics, particularly in molecular diagnostics. Current molecular diagnostics are highly labor-intensive and lack automation, and have to be done in central clinical laboratories with trained technicians. Laboratory-on-a-chip, taking advantage of the merger and development of microfluidics and biosensor technology, has shown promise towards a solution for performing analytical tests in a self-contained and compact unit, enabling earlier and decentralized testing. However, obstacles exist for lab-on-a-chip to become a viable product, and two key challenges are to integrate the fluid regulatory elements on a single platform and to detect target analytes with high sensitivity and selectivity [1]. It is the goal of this work to overcome the two obstacles.

1.2 Bio/nano particle manipulation

One of the most important functions in lab-on-a-chip technology is to deal with bio/nano particles that are suspended in aqueous solution. A wide range of particles can be manipulated in microfluidic devices, from cells (~10s μm) and bacteria down to viruses (~100 nm), protein molecules, and DNAs.

Preconcentration, separation, and identification of macromolecules such as DNA and proteins play an important role in sample processing and analysis of (bio) chemistry and life sciences. Recent development of nanometer scale sensing elements has enabled biomolecular detection at a level of femtomolar (fM) concentration [2]. By scaling down a sensor, the detection system can increase its signal-to-noise ratio for more sensitive detection. However, as the concentration of target analytes is lowered,

the diffusion and absorption to the sensor takes longer and longer, to the extent that the detection becomes limited by the absorption of the target analytes to the sensor. Theoretical analysis [3] reveals that for diluted bio-solution in femtomolar (fM) range, the detection is usually a transport-limited process. It is found that if diffusion is the sole mechanism for the delivery of nanoparticles to the sensor, it would take impractically long incubation time in static fluid, from weeks to months, for the analytes at the sensor to reach critical mass (theoretical study results shown in figure 1-1).

To speed up the detection, it is necessary to break the diffusion barrier in static fluid, so a flow-through system is often used, in which analytes are flowed pass the sensor with a stream of buffer solution. Reference [4] investigates the effects of the surface reaction, convection, and diffusion processes on the binding rate in a flow through system, and enhancing the diffusion was found to have the most pronounced effect on detection. As the response time of a biosensor is inversely proportional to the local concentration of the analyte in the vicinity of the sensor, replenishing the local analyte rapidly will significantly reduce the sensing response time. The binding rate at the sensor is shown to increase for microsensors [3] with a low to moderate channel Peclet number (Pe=LU/D, L: channel characteristic length, U: flow rate, D: diffusivity) [5]. It can also be noted that the enhancement is less for smaller sensors, still due to the diffusion limit. Because of the small dimensions of the microchannels and the limited flow rates, flow in microchannels is generally confined to laminar regime, i.e. no mixing. The travel of analytes to the sensor therefore relies on the molecular diffusion

Figure 1-1. Time required for a 10 μm long hemicylindrical sensor to accumulate 1, 10, and 100 molecules by pure diffusion. The sensor lies at the bottom of a channel whose width is equal to the sensor's length and which is filled with a 1 fM analyte solution. For radii smaller than 10 μm, the required time varies linearly with the radius. The inset shows the sensor geometry [3].

to transverse the streamlines. A smaller sensor allows less time for diffusion before the analytes stream past the sensor. As analytes are pumped through the microchannel, the nanoparticles need to diffuse across the height of the channel to reach the sensor on the channel bottom. A protein with $D=10$ μm^2/s takes 10 seconds to diffuse across a 10 μm channel. Given a sensor of 5 μm width with 100 μm/s flow stream velocity, reagents only have 0.05 second passing the sensor, so certainly most of the analytes just flow by.

To speed up the detection, it is necessary to break the diffusion barrier in static fluid, so a flow-through system is often used, in which analytes are flowed pass the sensor with a stream of buffer solution. Reference [4] investigates the effects of the surface reaction, convection, and diffusion processes on the binding rate in a flow through system, and enhancing the diffusion was found to have the most pronounced effect on detection. As the response time of a biosensor is inversely proportional to the local concentration of the analyte in the vicinity of the sensor, replenishing the local analyte rapidly will significantly reduce the sensing response time. The binding rate at the sensor is shown to increase for microsensors [3] with a low to moderate channel Peclet number (Pe=LU/D, L: channel characteristic length, U: flow rate, D: diffusivity) [5]. It can also be noted that the enhancement is less for smaller sensors, still due to the diffusion limit. Because of the small dimensions of the microchannels and the limited flow rates, flow in microchannels is generally confined to laminar regime, i.e. no mixing. The travel of analytes to the sensor therefore relies on the molecular diffusion to transverse the streamlines. A smaller sensor allows less time for diffusion before the analytes stream past the sensor. As analytes are pumped through the microchannel, the

5

nanoparticles need to diffuse across the height of the channel to reach the sensor on the channel bottom. A protein with D=10 μm^2/s takes 10 seconds to diffuse across a 10 μm channel. Given a sensor of 5 μm width with 100 μm/s flow stream velocity, reagents only have 0.05 second passing the sensor, so certainly most of the analytes just flow by. Hence, only a small fraction of available samples can be analyzed, and flow-through provides merely marginal improvement in binding rate.

Therefore, to improve the detection limits for micro/nano sized sensors, preconcentration becomes a necessary step to enrich the sample for downstream analysis. A number of strategies are currently available to provide sample preconcentration in liquids, including field-amplified sample stacking, isotachophoresis, chromatographic preconcentration, and membrane preconcentration. Most of them require special buffer arrangements, reagents, or both, which may not be feasible for in-situ detection. So in this dissertation, an electrokinetic method is presented and discussed, which is label-free with minimal requirements on pretreatment of the sample.

In our design of nanoparticle preconcentrator, electrode arrays are used to pump biofluid through microchannels and enhance the binding on the sensor. When excited with ac signal, AC electrothermal (ACET) effect would generate vortices that will give active guidance of targets towards the sensor. There have been prior research efforts using ACET effect for particle concentration [6, 7]. References [6] and [7] presented experimental results on concentrating particles in a closed microchamber. In reference [6], particles were concentrated on to the electrode surfaces. Particle count increased three times in two minutes. In some applications, such an arrangement may not be

applicable since the operation of the sensors and ACET electrodes may interfere with each other. In reference [7], the sensor is placed between the ACET electrodes on the bottom of a microchamber. The binding rate increased by a factor of close to nine with 10 V_{rms} applied ACET voltage. There are also simulation studies on combining ACET stirring with a flow through channel. References [8] and [9] simulated a flow through microfluidic system in which the sensor and ACET electrodes are located on separate channel walls facing each. Reference [8] predicted a 7x increase in bound antigen after 6 V_{rms} ACET voltage being applied for 100 seconds. Our work [10, 11] shows more improvement in binding if the sensor is placed between the electrodes instead of facing the electrodes on another channel wall.

A numerical study to design and optimize the ACEK induced preconcentration is presented in this dissertation. Because fluid convection is used to route the particles, the sensitivity enhancement is independent of the specific type of sensing method used. Therefore, the nanoparticle preconcentrator investigated in this dissertation can be viewed as a generic platform to work with various sensor systems.

The optimized preconcentrator can be integrated as a functional unit onto an immunoassay lab-chip, which can perform parallel diagnostic analyses in high automation for clinical and environmental applications.

Immunoassay is based on the specific antibody-antigen reaction, which is highly selective and sensitive. Conventional immunoassay test is a multistage, labor-intensive process that usually needs at least several hours or even days to complete multiple reagents delivery, incubations and several washing processes. The lack of automation

7

becomes the major obstacle between the studies of miniaturized immunoassay system and the clinical applications. The multi-step processes involve sequential sample loading and washing, and are prone to human error when the operations are done manually. This could result in reduced reliability and low efficiency.

The development of immunoassay lab-on-a-chip has been carried on for a decade, but little work has been done on the automation of the multi process assay tests. The fact is that most of the previous studies were based on pressure-driven flow to achieve the sample delivery. This requires capillary tubes or syringe pumps in the system, and these mechanical moving parts are a great obstacle towards automation since they are very difficult to integrate at chip size level.

Fortunately, electrokinetic methods have been introduced to advance the development of automated immunoassay systems. An integrated nanoliter DNA analysis device was designed by a research group at the University of Michigan [12], which can achieve DNA sample mixing, separation, reaction, and detection. The DNA samples were electrokinetically loaded into gel by electrophoresis. However, air tubes were used to apply air pressure to position sample in reaction region. Dongqing Li's group developed an electrokinetically-controlled immunoassay microfluidic system [13-15], for the detection of specific biomolecules. DC electroosmosis (DCEO) was used to load primary and secondary antibodies into the reaction areas. The drawback of using DC signal is that it requires high applied voltage (usually in ~kV) between two channel ends to reach certain level of electric field strength. And this high voltage can induce side effects such as bubble generation and pH gradient change in the solution.

Both external pressure driven pumping and DC electroosmosis cannot provide mixing. Low Renolds number in microchannels indicates laminar flow patterns, and flow through without mixing has very limited effect on the trapping of bio/nano-particles.

A fully automated portable immunoassay system using lab-on-a-chip technology is proposed in this dissertation. The goal is to reach rapid and sensitive nanoparticle detection, and make it a portable, low cost, and environment-friendly (less sample consumption and less waste) device. The schematic of the device is shown in figure 1-2. The immunoassay lab-chip uses a poly-(dimethylsiloxane) (PDMS) microfluidic channel. Reagents are pumped from the individual reservoir through the reaction area sequentially into the waste reservoir. Emerging technology AC electrokinetics (ACEK) is used for fluid transport and mixing, which enhances binding at the sensor due to its swirl-like flow patterns. Flow control units contain arrays of electrode patterns. When excited by appropriate ac signal, sample solutions will be pumped from storing well towards reaction channel. When ac signal is turned off, the pumping motion will stop and fluid is held by hydraulic pressure generated between sample reservoir and waste reservoir. Reaction channel has electrode arrays to induce pumping and mixing motion by AC electrokinetic effect. The whole microsystem is electrically controlled by low ac voltage (several volts), so the processes such as reagents delivery, incubation and washing can be readily automated.

With optimized design of channel geometry, electrode patterns, properly selected operation condition (ac frequency and voltage) and modified incubation procedures, the microsystem can greatly reduce the reaction time and improve sensitivity of the
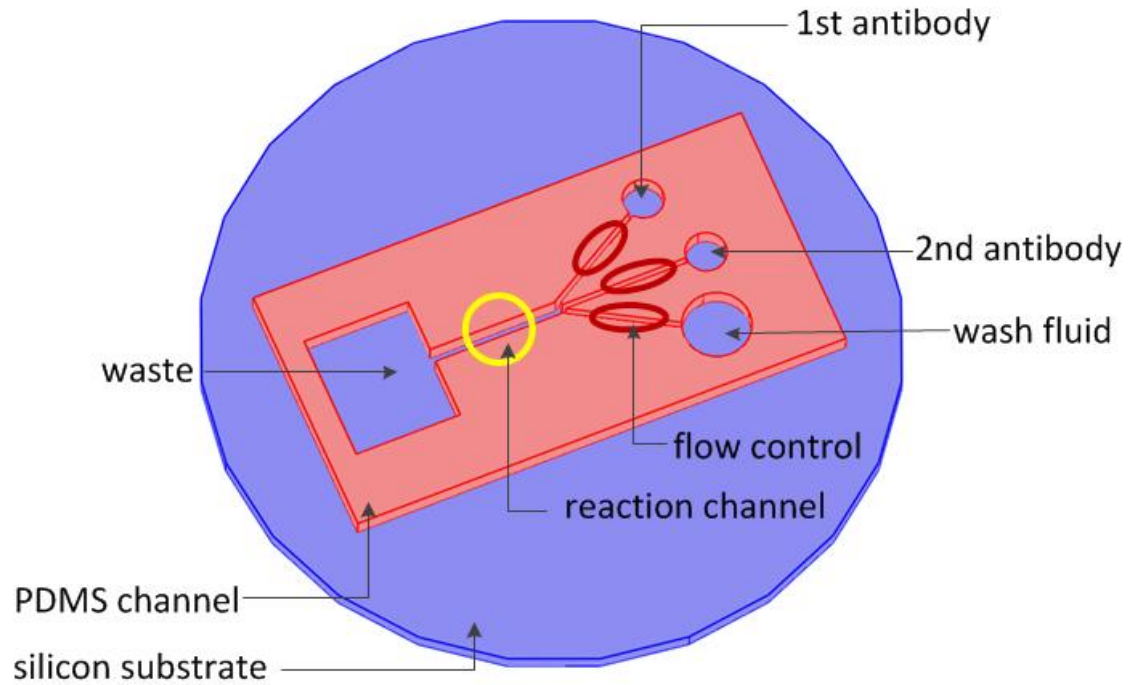
Figure 1-2. Prototype of ACEK enhanced immunoassay lab chip. Flow control units and reaction channel have electrode patterns that can pump and mix the sample fluid when excited by ac signal. Microfluidic channels and reservoirs are made of transparent PDMS. No mechanical moving parts are involved in this automated immunoassay lab-chip design.

assay. Our test results showed that primary antibody can selectively bind with specific antigen in the microchannel. And disease status can be easily distinguished by fluorescent light intensity change through binding of 2nd antibody (fluorescence labeled) with antigen-antibody conjugates. With the aid of ACEK, reaction time can be reduced to several minutes instead of conventional 30 minutes. We have successfully demonstrated pumping of 0.2x PBS solution, which has conductivity of 0.34 S/m, by AC electrothermal (ACET) effect. With immunoassay, the effect of ACET mixing on molecular level binding can be quantitatively studied. The results can be used to improve the sensitivity of biosensors. Improved sensors with single-chip form factor as a general platform could have a significant impact on a wide-range of biochemical detection and disease diagnostics including pathogen/virus detection, whole blood analysis, immune-screening, gene expression, as well as home land security.

Objectives of this research work:

I. Develop an ACET flow through concentrator for in-situ concentration of biomolecules. The system will use electrokinetic micropump to deliver conductive and viscous biofluids (e.g. serum) and capitalize on ACET vortices to direct target molecules across the channel towards the sensor.

II. Develop a comprehensive understanding of effects of ACET flow on the biomolecule transport (in-situ concentration) and their impact on electronic biosensing mechanism and performance. And develop the design rules for both the fastest ACET pump and most effective biomolecule concentration, and the optimal location of sensors, etc. The biosensing study will reveal the effects of

11

guided biomolecule transport and applied E-fields on the limit of detection (LOD), detection time, binding dynamics, selectivity and detection noise, many of which remains unknown but important to unleash the full potential of biosensors.

1.3 Outline of this dissertation

Chapter one introduces the concept of microfluidics and motivation of this research, which is to use ACEK technology to enhanced particle trapping and to design an automated lab-on-a-chip device for immunoassay purpose. Chapter two gives a detailed literature review on various trapping methods and applications in microfluidics. The theory of ACEK and related particle dynamics are discussed in chapter three. Chapter four presents a numerical study and optimization of in-situ preconcentration for rapid and sensitive nanoparticle detection. The design of an ACEK immunoassay lab chip for accelerated diagnosis is presented in chapter five, in which incubation and operation parameters are optimized. The conclusions and future work are presented in chapter six.

Chapter Two: Literature Review on Particle Concentration in Microfluidics

The ability to concentrate and manipulate particles, molecules, and atoms has revolutionized many fields of science and engineering. Over the past decades, a diverse set of methods has been developed to confine and manipulate microscale and nanoscale particless in aqueous solution through direct control of particle position and velocity. The review of particle concentration in this chapter will be based on non-electric and electrokinetic induced trapping methods.

2.1 Non-electric trapping methods

Non-electric trapping methods include optical trapping, magnetic trapping, acoustic trapping, and hydrodynamic trapping. These methods are developed to manipulate microscale and nanoscale particles in aqueous solutions and have been used to investigate a broad range of physical and biological problems. Each method has its own advantages and limitations.

2.1.1 Optical trapping

Optical manipulation of particles has been developed for over 30 years [1-5]. Many of the most powerful optical manipulation techniques are derived from single-beam gradient induced optical traps known as optical tweezers. Optical tweezers are formed by tightly focusing a laser beam with an objective lens of high numerical aperture.
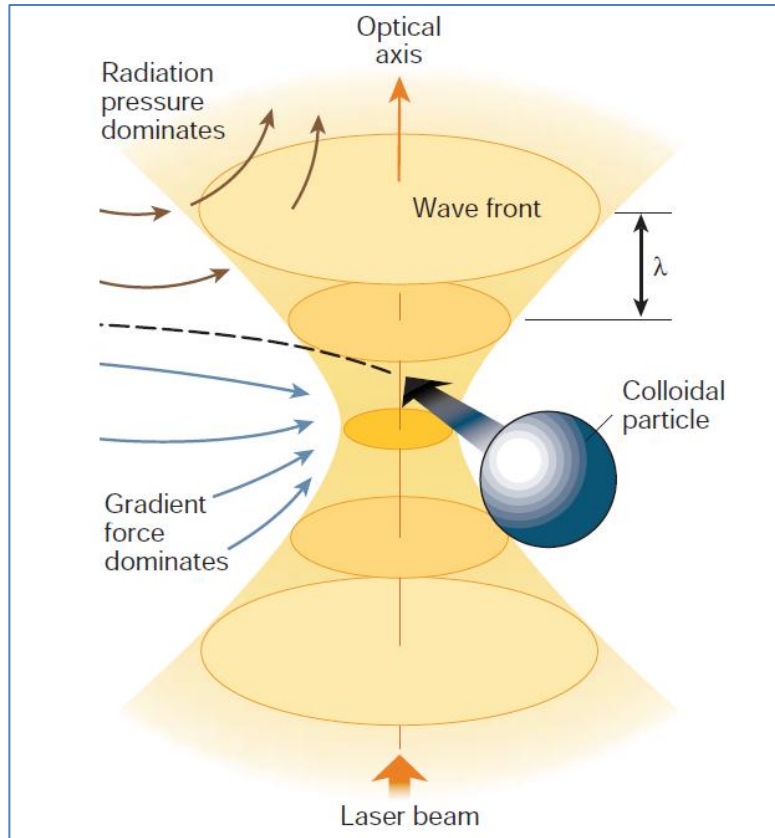
Figure 2-1. Optical tweezers use a strongly focused beam of light to trap objects. Intensity gradients in the converging beam draw small objects, such as a colloidal particle, toward the focus, whereas the radiation pressure of the beam tends to blow them down the optical axis. Under conditions where the gradient force dominates, a particle can be trapped, in three dimensions, near the focal point [2].

Dielectric particles near the focus develop an electric dipole moment, and the dipole interacts with the inhomogeneous electric field induced by laser fluctuation, which will experience a force due to the transfer of momentum from the scattering of incident photons. Intensity gradients in the converging beam draw small objects, such as a colloidal particle, towards the focus, whereas the radiation pressure of the beam tends to blow them down the optical axis. Under conditions where gradient force dominates, a particle can be trapped in three dimensions, near the focal point. Figure 2-1 demonstrates the principle of optical trapping [2].

Novel optical trapping approaches have been developed, which includes combined optical trapping with single molecule fluorescence, optical rotation and torque, and holographic optical traps [3]. Optical tweezers can be used to precisely trap and move objects ranging in size from tens of nanometers to tens of micrometers. Reference [1] was the first to report using optical tweezers to trap dielectric particles with sizes from 10 μm down to about 25 nm. Reference [4] developed sub-wavelength-scale slot waveguides for optical capture, trapping, and transporting of both dielectric nanoparticles (75 nm) and λ-DNA (48 kilobase). The slot waveguides were imbedded in the fluid path and can intercept particles flowing through when laser was activated. An optically induced microfluidic manipulation technique was developed in reference [5], in which optoelectronic tweezers were used to create high resolution dielectrophoresis (DEP) electrode patterns on a photoconductive surface. By programming the optical images on the photoconductive surface, different electrode patterns can be used to manipulate single particle. This optically induced electrical

15

manipulation of particle technique can achieve both high resolution and high throughput, and uses 100,000 times lower energy than conventional optical tweezers. More applications of optical trapping methods can be found in references [2, 3].

2.1.2 Magnetic trapping

While optical tweezers may have the potential to photo-damage the molecules due to the intense laser spot, using magnetic force to manipulate particles is more biocompatible. Magnetic tweezers [6-8] use magnetic force to confine the target particles into a certain potential well. Biological particles, such as cells, DNAs, and proteins, need to be treated so magnetic beads are attached to the target to experience magnetic force. It has been proved successful in monitoring and manipulating micrometric particles in three dimensions (3D) using magnetic field gradients. In reference [6], magnetic field was generated and controlled by six vertical coils. Particles with a diameter of 4.5 μm were actuated by magnetic force to have translational and rotational movement. Reference [7] reported manipulation of biological cells using a microelectromagnet matrix. The matrix consists of two layers of straight Au wires, aligned perpendicular to each other. By adjusting the current passing through independent wire, the microelectromagnet matrix can create versatile magnetic field patterns to control the motion of individual cells in fluid. The manipulation of individual yeast cells attached to a magnetic bead as well as separation of viable and nonviable cells were demonstrated. The manipulation of single DNA molecule using magnetic field was reported in reference [8]. Single λ-DNA (attached to

16

magnetic beads) was trapped by placing a permanent magnet as close as 10 μm away. The force on DNA can reach 200 pN (pico-Newton). This near-field-magnetic tweezer can be a powerful tool for analysis of DNA-protein interactions.

2.1.3 Acoustic trapping

Like magnetic trapping, acoustic trapping [11, 12] also has the advantage of nonintrusive (non-contact) nature. Acoustic trapping uses ultrasonic standing wave to generate a harmonic potential cavity for particle trapping. The absorption of high frequency acoustic energy within the cell and fluid generates pressure forces that cause aggregation of cells at pressure node or antinodes. Compared with optical trapping methods, acoustic trap does not require particles to be transparent. The trapping force increases linearly with particle volume. Reference [11] reported a confocal standing-wave ultrasonic trap suitable for high spatial resolution positioning of microscopic particles. Glass spheres with average diameter of 2.1 μm were trapped at resonance frequency of 11 MHz. Reference [12] reported a microfluidic chip-based acoustic noncontact trapping method. Figure 2-2 shows a schematic of the ultrasonic transducer imbedded in a microfluidic channel. The transducer generates a near-field pressure distribution pattern that can trap particles to pressure minima. Polystyrene particles ranging from 0.87 to 10 μm in diameter were trapped with very high efficiency, at 7 Vpp, 12.4 MHz, with the help of hydrodynamic focusing flows.
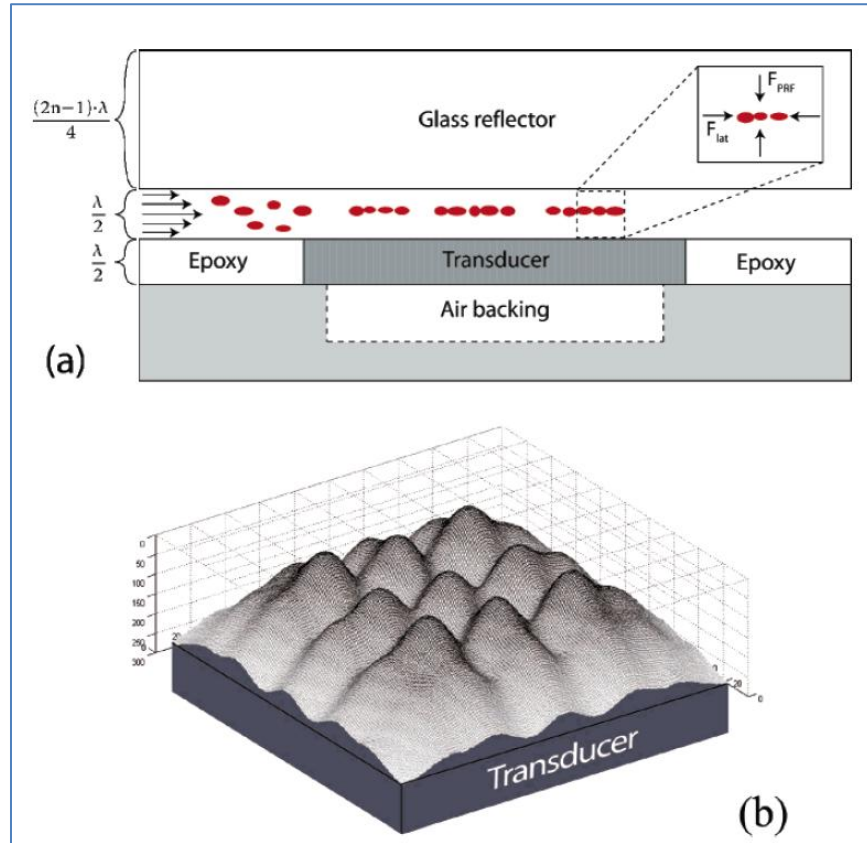
Figure 2-2. (a) side-view schematic of the acoustic transducer imbedded in a microfluidic channel. The acoustic forces focus the cells into clusters in the center of the channel as illustrated in the inset. (b) Actual trapping sites are given by the near-field pressure distribution as shown in 3D image. Cells will be trapped in clusters around the local pressure minima (peaks correspond to the pressure minima) [12].

18

2.1.4 Hydrodynamic trapping

Hydrodynamic forces have been used to confine and manipulate particles [13-18]. Trapping is achieved by controlling fluid dynamics to generate eddies [13], microvortices [14], stagnation points [15], and shear stress [16, 17]. Hydradynamic trapping is feasible for any particle with no specific requirements on the material composition or the chemical/physical nautre of the trapped objects. Reference [13] reported hydrodynamic tweezer for single cells trapping created by low frequency oscillations of fluid around a cylinder in a microchannel. Four eddies were formed around the cylinder and served as trapping centers. In reference [14], hydrodynamic trapping of bioparticles was demonstrated in a microfluidic device utilizing a resonating microplate to generate two counter-rotating microvortices. Trapping and releasing of 10 μm polystyrene beads, human embryonic kidney (HEK) cells, red blood cells (RBCs), and IgG antibodies were demonstrated. A stagnation trapping site was generated by a planar extensional and compressional flow field at the junction of two perpendicular microchannels, reported in reference [15]. References [16] and [17] reported using shear stress flow to confine cells in hydrodynamic cell traps. 3D cell trapping arrays were fabricated with poly-dimethylsiloxane (PDMS), and by controlling the flow stress, cells could be trapped on site to for cell culture or fusion. Reference [18] proposed a trap and release design of microfluidic device that use hydrodynamic force to trap particles, while use optical approach to form micro-bubbles that can squeeze the particle away from the trap.

2.2 Electrokinetic induced trapping methods

Applying electric fields over fluids may lead to forces on the particles and fluid motion. The study of such phenomena is referred to as electrokinetics (EK). Using electric signal to manipulate particles can be achieved with a DC or AC source, which is usually referred to as DC electrokinetics and AC electrokinetics. Compared with non-electric trapping methods, electrokinetic methods have several advantages. Electrodes can be easily positioned due to the advance of semiconductor microfabrication. Electrical signal is easy to control, giving it more freedom to design the trapping devices. No moving mechanical parts enable integration of devices to microchip size.

2.2.1 DC electrokinetics trapping

DC electrokinetics (DCEK) is to apply direct electric (current) field to induce fluid motion and manipulate particles within. The research on DCEK has been carried on for decades, so applications of DCEK are quite mature. Two important applications in DCEK are DC electroosmosis (DCEO) and electrophoresis (EP). Because the chemical equilibrium between a solid surface and an electrolyte solution typically leads to the interface acquiring a net fixed electrical charge, a layer of mobile ions, known as an electrical double layer, forms in the region near the interface. DC electroosmotic flow originates from the Coulomb force induced by an electric field on net mobile electric charge in the double layer. Electrophoresis is the motion of dispersed (charged) particles relative to a fluid under the influence of a spatially uniform electric field.

Electrodes with dc voltage are usually applied to the inlets and outlets of the channel.

On-chip capillary electrophoresis (CE) is one of the most widely used microchip assays for preconcentration and particle manipulations. Reference [19] developed a microfabricated porous membrane structure that enables electrokinetic concentration of DNA and protein samples. DNA samples were electrokinetically driven to the membrane through which only buffer ions could pass. Concentration of DNA particles increased 100-fold over time. Three most widely used CE techniques are field-amplified sample stacking (FASS), electric field gradient focusing (EFGF), and isotachophoresis (ITP). Depending on different applications, capillary channel walls may be treated for enhanced or reduced electroosmotic flow for better concentration results. FASS is the technique to set up electric field discontinuity across the concentration boundary and charged analytes will then automatically stack due to velocity changes after they cross the concentration boundary. Using this technique, concentration can increase by a factor of 1100 [20] using capillary and a factor of 70-100 using microchips [21, 22]. EFGF is a separation technique that uses an electric field gradient and an opposing hydrodynamic flow to separate and concentrate charged analytes. With the use of an EFGF device, green fluorescent protein was concentrated 10000-fold and the separation of a protein mixture was demonstrated [23]. In isotachophoresis (ITP), the sample is introduced between a fast leading electrolyte and a slow terminating electrolyte. After application of an electric potential a low electrical field is created in the leading electrolyte and a high electrical field in the terminating electrolyte. The sample constituents migrate at different speeds and the faster

constituents will create a lower electrical field in the leading part of the sample zone and vice versa. Then the constituents will concentrate at an equilibrium concentration, surrounded by sharp electrical field differences. A million-fold signal enhancement was reported using high-sensitivity on-chip CE detection system and an ITP/CE protocol with no manual buffer exchange steps [24]. Due to various operational constraints, such as reagent and material requirements, the above concentration processes are difficult to implement for in situ concentration and detection.

Using combined effects of electroosmosis and electrophoresis, particles can be trapped and manipulated in aqueous solution [25-27]. An anti-Brownian electrophoretic trap (ABEL trap) works by monitoring the Brownian motion of the particle via fluorescence microscopy, and then applying a feedback voltage to the solution so that the electrophoretic drift exactly cancels the Brownian motion [25, 26]. The ABEL trap works on any object that can be imaged optically and that acquires a charge in water. Trapping of fluorescent polystyrene nanospheres with diameters down to 20 nm was demonstrated. Reference [27] used a feedback control of microflows to independently steer multiple particles in the solution. Particle locations are identified in real-time by an optical system and transferred to a control algorithm that determines the electrode voltages necessary to create a flow field to carry all the particles to their next desired locations. This control allows manipulation of any visible particles, neutral (by EO flow) or charged (by EP force).

2.2.2 AC electrokinetics trapping

Unlike DCEK that electric filed is usually parallel and uniform, AC electrokinetics originates from the inhomogeneous electric field induced by ac signal applied over microelectrodes. ACEK has many advantages over DCEK, such as low applied voltage, portability and potential integration into lab-on-a-chip devices. ACEK need only several volts to implement, compared with thousands of volts for the same effect by DCEK. The reason is that the spacing of ACEK actuated electrodes is usually in micrometers, while for DCEK devices, voltages are applied over centimeters. So to achieve the same electric field strength, the voltage applied to DCEK devices should be two or three orders higher than that of ACEK devices. A primary advantage of ACEK is that the alternating electric fields significantly reduce electrolysis, suppress electrochemical reactions, and prevent bubble generation or pH gradient change at the interface of electrode/electrolyte surface. Detailed theory and mechanisms of ACEK is presented in chapter three.

Recent years have witnessed significant advances in the research of ACEK and development of lab-on-a-chip technology. ACEK mainly includes dielectrophoresis (DEP), AC electroosmosis (ACEO), and AC electrothermal effect (ACET). Each of them has different origin and mechanism to interact with fluid and particles.

2.2.2.1 Trapping of particles by DEP

Dielectrophoresis is a nondestructive electrokinetic mechanism with great potential to manipulate particles. It has been successfully used to deal with microparticles since

1960s. Manipulation of nano/bio-particles, such as cells, virus, proteins, and DNA molecules, with DEP forces have been reported in several aspects since 1990s. Unlike EP force that requires particles to be charged, DEP is a force exerted on a dielectric particle when it is subjected to a non-uniform electric field. A particle with polarizability (conductivity and permittivity) different from that of the suspending medium will influence the electric field distribution around it. The induced dipole around the particle will experience electric force by external nonuniform field, resulting in particle movement. When the particle is more polarizable than the medium, it tends to move towards the high-field region, known as positive DEP (p-DEP). The opposite leads to negative DEP (n-DEP), when the particle is less polarizable and tends to move to low-field region.

Theory (details in chapter 3.1.3) shows that DEP force is a function of particle volume, polarizability difference between particle and medium, electric field gradient, and signal frequency. So specially designed electrode patterns can manipulate particles in different way by carefully choosing electric signal frequency and magnitude. Figure 2-3 shows an example of negative and positive DEP traps, respectively, formed by polynomial electrodes [28]. The low-field region lies at the center of the electrode array and the high-field regions are along the edges of electrodes. Using 557 nm diameter latex spheres, at higher frequency (5 MHz), particles are less polarizable than the medium, and are repelled to low-field electrode gap. At lower frequency (500 kHz), particles are trapped to electrode edges where electric field is high.

Besides polynomial electrode pattern, other electrode designs for DEP
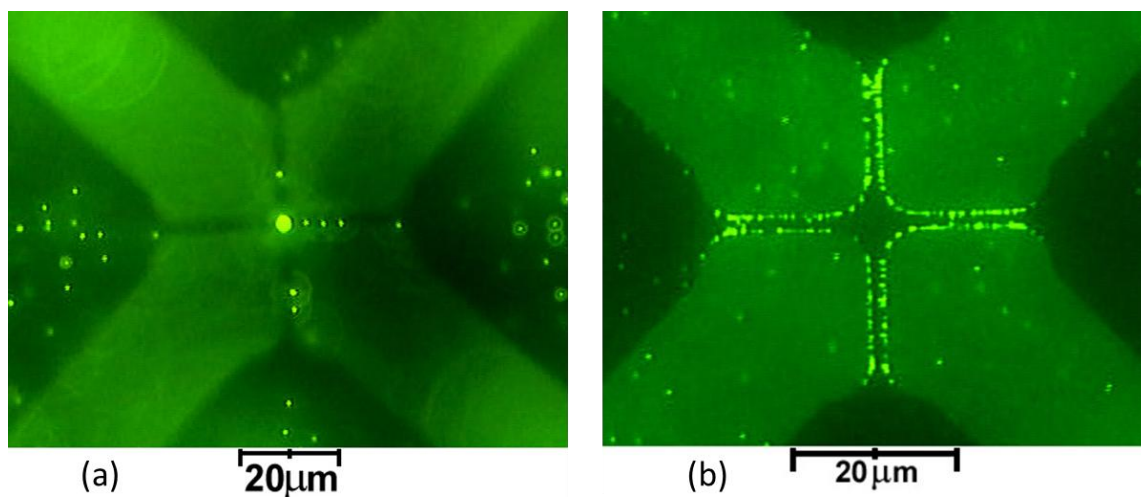
Figure 2-3. (a) Negative DEP of 557 nm latex spheres on polynomial electrodes for an applied signal of 5 volts peak-to-peak at 5 MHz. Particles are trapped to low-field region at electrode center gap. (b) Positive DEP of 557 nm particles trapped along the high-field electrode edges for an applied signal of 5 volts peak-to-peak at 500 kHz [28].

manipulation of particles have been reported in literatures, including castellated electrodes [28, 29], interdigitated electrodes [30-32], orthogonal electrodes (T electrodes) [33, 34], and 3D electrode structures [35, 36]. Electrodes are usually fabricated on glass slides or silicon wafers, and channels are built with PDMS.

Castellated electrode designs can generate distinctive field maxima and minima, and can be used to trap and characterize latex particles [28] as well as biological cells [29]. As frequency changed from 8 MHz to 700 kHz at 8 volt peak-to-peak (Vpp), in a solution with conductivity of 2 mS/m, latex particles experienced a transition from negative DEP to positive DEP [28]. Different particles and cells have different frequency response in specific solution, so at a certain condition (frequency and fluid conductivity), a mixture of particles can be separated and trapped to different regions of electrode patterns. Reference [29] demonstrated separation and trapping of live and dead yeast cells using castellated electrodes. Live cells can be attracted by positive DEP to the edges of the electrodes, whilst the dead cells are repelled from the electrodes into triangular-shaped aggregations.

Interdigitated electrodes, also known as planar or parallel electrodes, are widely studied to perform DEP trapping and separation [30-32]. Live and heat-treated Listeria cells were separately trapped to electrode edges and interelectrode gaps, respectively [30]. Time and frequency dependence on 12 kilobase pair plasmid DNA were studied using interdigitated electrodes in reference [31]. By comparing the different electrode orientations with respect to flow direct, reference [32] concluded that interparticle electric interactions do not affect the particle trapping in the high-field strength regions.

Orthogonal electrode pattern consists of one high field electrode and one low field electrode that are arranged perpendicular to each other, shown in figure 2-4(a). High field electrode tip is the p-DEP region and low field electrode gap is the n-DEP region. Using this device, erythrocytes (red blood cells, RBCs) cells are characterized to have the optimal mobilities at approximately 1 MHz, in a 0.1 S/m isotonic phosphate buffer saline (PBS) medium [33]. Figure 2-4 (b) and (c) demonstrated single-wall nanotube (SWNT) self-assembly test using orthogonal electrodes [34]. At 1 kHz frequency, SWNT self-assembly was confined to a thin boundary near the electrode and highly branched (b), while at 1 MHz frequency, SWNT self-assembled rapidly from both electrodes to form thin uniform wires that bridged the gap. Bulk CNT-pathogen docking was achieved using this method. E. coli bacteria were trapped 10 times more entangled within the SWNT in the solution than without SWNT presence.

3D focusing of nanoparticles in microfluidic channels was reported in reference [35], in which electrodes were fabricated on both top and bottom glass slides, separated by an insulator layer. Four tapered electrodes can focus nanoparticle to the negative DEP trap in the center of the channel. A three dimensional grid electrode system used to manipulate single biological cell was reported in reference [36]. Strip electrodes on top and bottom glass were aligned perpendicular to each other forming grid pattern. By controlling the signal frequency and phase on electrodes, biological cell can be trapped to grid junction by p-DEP or released by n-DEP.
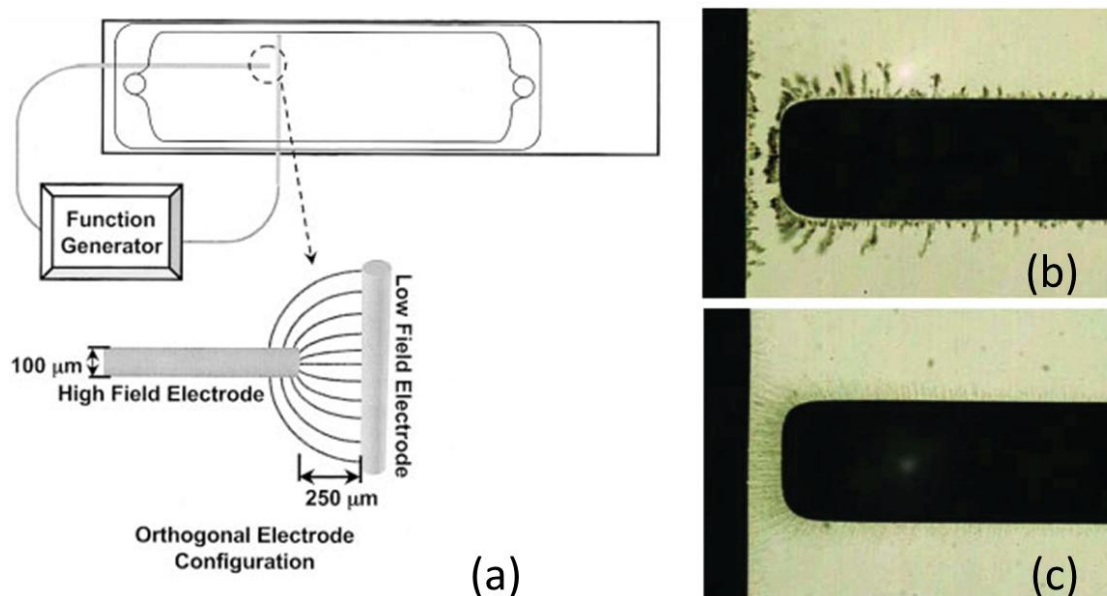
Figure 2-4. (a) Schematic of orthogonal electrode microdevice used for DEP trapping. High field and low field electrodes are arranged perpendicular to each other to induce nonuniform electric fields [33]. (b) SWNT self-assembly forms aggregates and confined in thin boundary layer near electrodes at 1 kHz [34]. (c) SWNT self-assembly forms thin uniform wires that bridged the gap at 1 MHz [34].

2.2.2.2 Trapping of particles by ACEK flow

While DEP is the direct force on particles, ACEK (ACEO and ACET) flow can manipulate particles through fluid viscosity. The applications of ACEK flow in collecting and concentrating particles have been studied extensively.

ACEO (details in chapter 3.1.1) refers to the microfluidic motions generated at electrode surfaces when ac signals are applied. The tangential electric field interacts with the induced charges in electric double layer that forms at interface of electrode/electrolyte interface, resulting in flow motion due to fluid viscosity. It typically happens at low frequencies when the interfacial impedance dominates. ACET effect (details in chapter 3.1.2) results from the interaction of ac electric fields and temperature gradients in the fluid. Nonuniform electric field generates nonuniform thermal gradient in the fluid through Joule heating. Thermal gradient induce spatial mobile charges that will move under electric field, resulting ACET flow.

Two major configurations of ACEK electrodes have been reported so far are the so called "side-by-side" electrodes [37-40] and "face-to-face" electrodes [41-44]. Side-by-side electrodes are fabricated on one side, usually on the bottom of the substrate, while face-to-face configuration uses electrode pair that is on top and bottom of the device, facing each other. Both designs create nonuniform electric field distribution, leading to ACEO and ACET flows.

One example of using side-by-side electrode configuration is shown in figure 2-5, in which the electrodes form dot-ring shape [37]. When excited by ac signal, ACEO force generates microflows that convey particles from the bulk of the fluid onto the
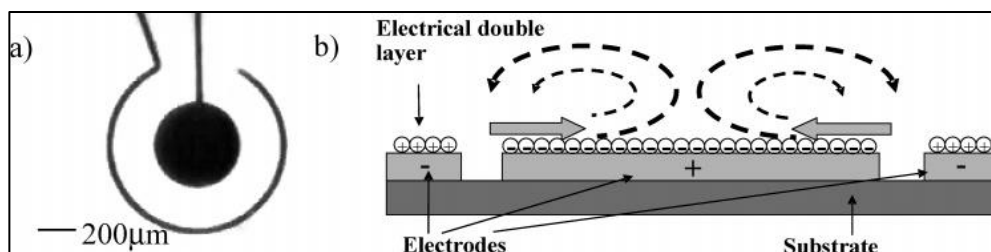
Figure 2-5. (a) Electrode design of the ac electroosmotic processor (top view). (b) Schematic (side view) illustrating electrode polarization and formation of ac electroosmotic flow. Solid arrows represent the ac electroosmotic force and dotted lines indicate the flow pattern [37].

electrode surface. The counter-rotating vortices generate flow stagnation point where particles can be trapped. Biological particles, such as E. coli bacteria, λ phage DNA, and single-stranded DNA fragments as small as 20 bases, have been concentrated using this device by ACEO flow. The other commonly used side-by-side electrode pattern is parallel electrodes [38-40]. One example to use planar electrodes for on-chip bioparticles trapping is shown in figure 2-6. ACEO flow generates two large vortices and two small vortices, and the counter-rotating vortices trap particles onto the stagnation locations. With a bias dc offset applied with ac signal, more ions are induced in double layer due to Faradaic charging, leading to enhanced ACEO flow, thus more particles can be trapped [38, 39].

One example of using face-to-face electrode configuration to concentrate particles is shown in figure 2-7. The device is formed by conductive corrals on bottom silicon substrate and top indium-tin oxide (ITO) electrode. Similar to side-by-side electrodes, face-to-face electrodes generate nonuniform electric fields in the chamber and induce
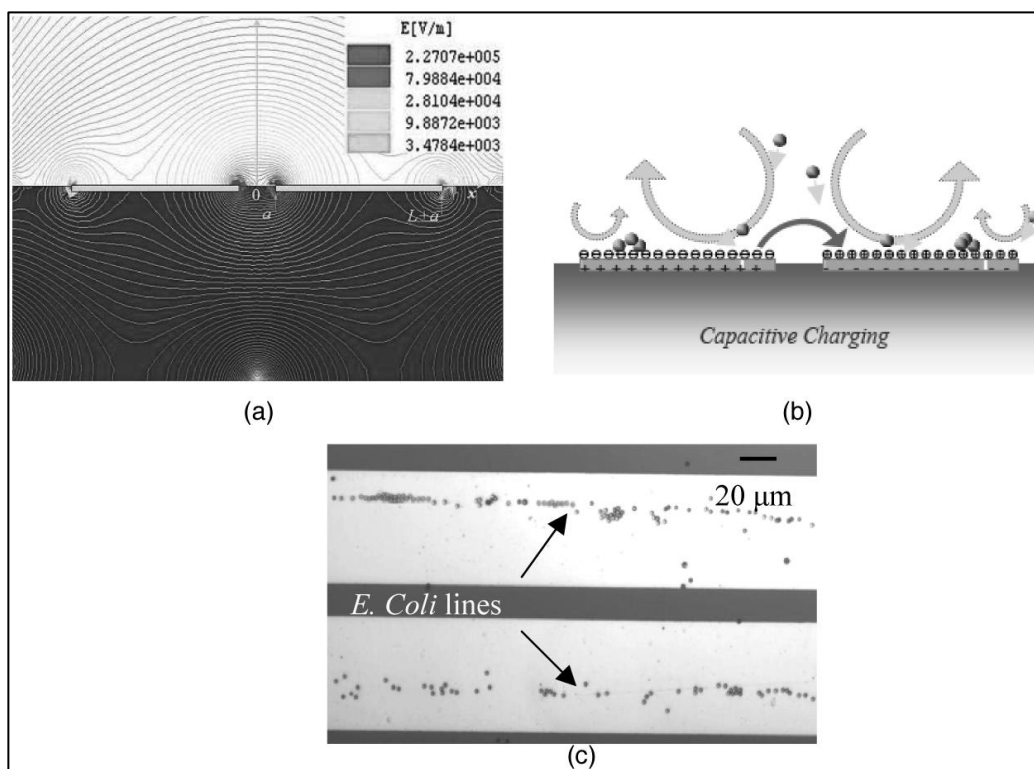
Figure 2-6. (a) Electric fields around a planar electrode pair. The tangential component changes sign at $1/\sqrt{2}$ of electrode width. (Axes: relative dimensions.) (b) Four counter-rotating vortices are formed above the electrodes due to changes in tangential electric fields, which facilitate particles aggregation on electrodes. (c) Assembled E. coli lines on Au electrodes [38].
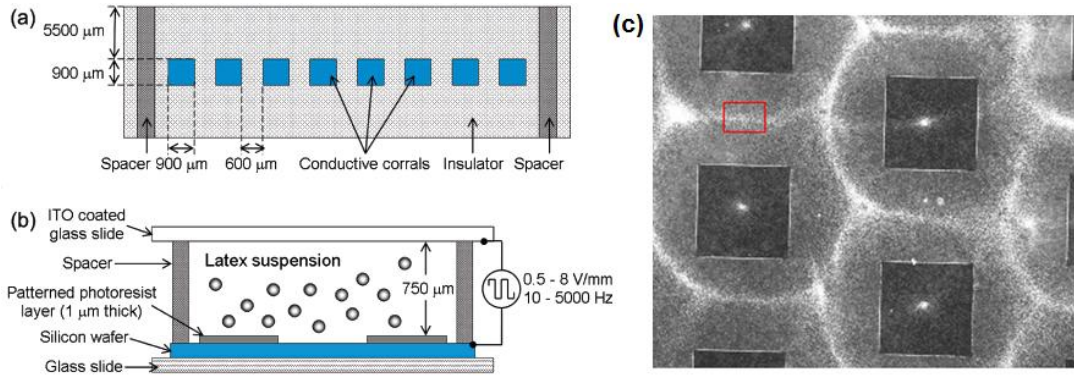
Figure 2-7. (a) Schematics of the patterned electrodes on silicon wafer [41]. (b) The experimental setup of the chamber used for particle collection [41]. (c) Observation of trapped particles (fluorescent) on conductive surface after applying ac signal for 5 minutes. Dark squares are nonconductive areas [42].

microflows. The converging flow will trap particles to conductive surface by ACEO [41] and ACET effect [42]. The face-to-face design can be easily integrated into other devices. One example is its integration with micro-cantilever sensor, as shown in Fig. 2-8. ITO glass serves as top electrode and metal coated cantilever acts as bottom electrode. By measuring the resonance frequency difference of the cantilever, the amount of trapped particles can be quantified. Experiemntal results of focusing 200 nm particles onto a micro-cantilever probe by ACEO flow was demonstrated in [43, 44].

2.2.2.3 ACEK flow enhanced DEP trapping of particles

DEP effect is very suitable for particle trapping, however, it is often required to use small electrodes and high voltage in order to achieve adequate electric field gradient.
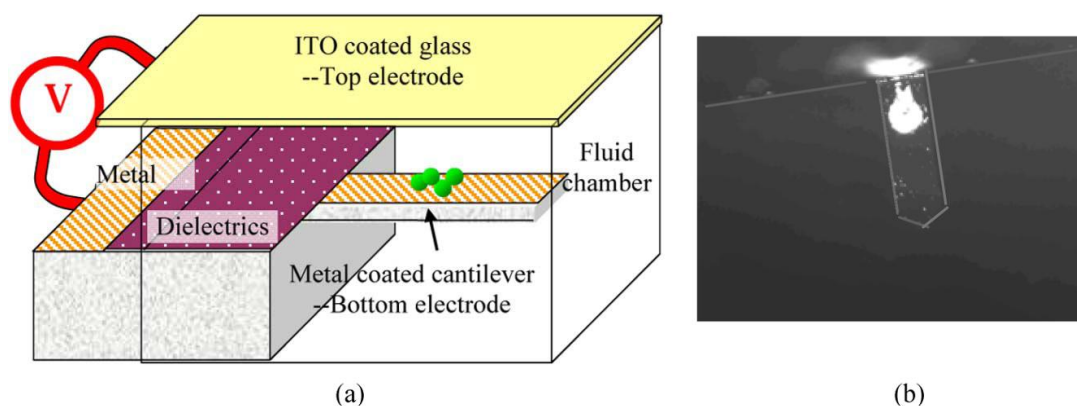
Figure 2-8. (a) Schematic of a micro-cantilever particle concentrator. (b) Experiemntal results of focusing 200 nm particles onto a micro-cantilever probe by ACEO flow [43, 44].

And DEP effective range is limited due to the rapid decay of the electric filed with the distance from the electrodes. It is also size dependent, making it less effective for submicron particles. On the other hand, electrofluidic focusing by ACEO or ACET is realized through fluid motion. It has no dependence on particle size and has longer effective range as long as particles stay suspended in the fluid. By combining the effect of ACEK flow together with DEP effect, particles can be conveyed by microflow to the trapping sites for concentration, and a highly automated system can be integrated for lab-on-a-chip applications.

There have been prior researches that use flow through to enhance DEP manipulation [45, 46]. The disadvantage of this setup is that a pressure driven mechanical pump is required to push fluid through the chamber. With the development of ACEK techniques, electrohydrodynamic (EHD) flow can replace conventional hydrodynamic flow to enhance trapping. Figure 2-9 shows a typical design diagram
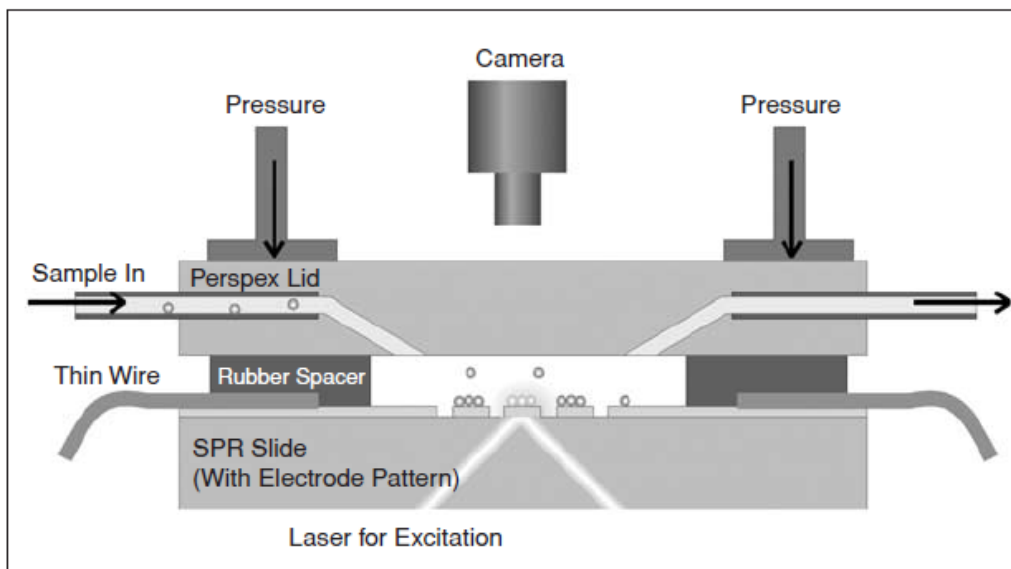
Figure 2-9. A schematic diagram of the combined DEP/EHD zipper electrode system combined with a flow cell and evanescent light scattering detection [47].

that combine EHD and DEP effects with detection system. The electrode designs can vary according the specific needs for concentration, and EHD flow can be ACEO [47-51] or ACET [52-55] induced.

For ACEO enhanced DEP trapping, sample solution is usually limited to low ionic strength. A high conductivity fluid will compress the thickness of the electric double layer, leading to ineffective ACEO flow. The highest conductivity with which ACEO has been observed is 85 mS/m. However, most biological applications involve with conductive fluids such as PBS solution, with conductivity as high as 1-2 S/m. To actuate fluid at such high conductivity, ACET effect can be the only possible method. Studies have been focused on ACET enhanced trapping in recent years, with both experimental results [52-54] and numerical simulations [55]. Reference [52]

demonstrated an electrode design that used ACET enhanced negative DEP trapping. There exists a competition between ACET flow and DEP force in the device, the trapping enhancement can be reduced if ACET flow dominates DEP effect, especially for smaller particles. ACET flow enhanced DEP trapping devices can generate well-defined electric field maxima/minima that can act as target-specific attachment/detection sites. ACET enhancement of heterogeneous assays in a microfluidic device was reported [53], in which ACET effect generated stirring flow that can enhance binding of antigen-antibody on the surface.

A new idea was proposed recently that one can combine ACEO and ACET flow in the same device to enhance the transporting of particles and DEP effect [54]. The name is given as ETEO, meaning that flow phenomena is driven by both double layer charging (EO) and thermal generating Joule heating (ET). A closed-loop electrode device was fabricated and yeast cells were trapped and separated according to their viability. By understanding the frequency and buffer dependence for both ETEO fluid flow and DEP induced cell behavior, and by integrating these phenomena into insulating PDMS microchannels, a wide array of cellular manipulation options becomes available.

ACEK is a very promising technique for both fluid and particle manipulation. Well-designed electrode patterns actuated with appropriate signal can achieve rapid and sensitive concentration of bio/nano particles for diagnostic applications. It has attracted wide attention and more applications are emerging.

Chapter Three: AC Electrokinetics and Forces on Particles

3.1 AC electrokinetics mechanisms

Applying electric fields over fluids may lead to forces on the particles and the fluid. The study of such phenomena is referred to as electrokinetics (EK). There are two main categories of electrokinetic phenomena, DC electrokinetics (DCEK) and AC electrokinetics (ACEK). ACEK [1-3] is a general term which refers to a range of techniques that ac electric fields are used to study and manipulate particles, particularly bio-particles, and fluids. It has been proved successful in the manipulation of fluids, characterization of cells and bacteria as well as the trapping and separation of diverse particle types.

ACEK has many advantages over DCEK, such as low applied voltage, portability and potential integration into lab-on-a-chip devices. ACEK need only several volts to implement, compared with thousands of volts for the same effect by DCEK. The reason is that the spacing of ACEK actuated electrodes is usually in micrometers, while for DCEK devices, voltages are applied over centimeters. So to achieve the same electric field strength, the voltage applied to DCEK devices should be two or three orders higher than that of ACEK devices. A primary advantage of ACEK is that the alternating fields significantly reduce electrolysis, suppress electrochemical reactions, and prevent bubble generation and pH gradient change at the interface of electrode/electrolyte surface.

ACEK is commonly categorized into three types, ACEO, ACET effect, and DEP. ACEO and ACET effect are two mechanisms that the applied electric field interacts directly with the fluid, while DEP is the force exerts on the particles suspended in the fluid. ACEO and ACET effect can be used to manipulate fluids at microscale and transport particles in the fluids, and together with DEP effect, particles can be separated and concentrated for detection and other diagnostic applications.

3.1.1 AC Electroosmosis (ACEO)

AC electroosmosis is a flow phenomenon that occurs below the charge relaxation frequency of a fluid [1]. Charge relaxation frequency of the liquid is defined as $\omega=\sigma/\varepsilon$, where σ and ε are conductivity and permittivity of the fluid, respectively.

At the interface of an electrode and electrolyte, a transition occurs from electronic conduction in the electrode material to ionic conduction in the fluid. When an electric potential is applied to the electrode in a solution, counter-ions are electrostatically attracted to the electrodes, and are of opposite polarity to the excitation voltage. This polarization process is termed "capacitive charging" [3]. The region of liquid at the interface has a higher density of counter-ions and a lower density of co-ions than in the bulk fluid. This region is usually referred to as the electrical double layer (EDL). The resulting change in the distribution of ions near the surface is governed by the spatial distribution of the surface electrostatic potential. When a particle or an electrode is immersed in an electrolyte, the surface charge is balanced by an equal (and opposite) amount of excess charge in the double layer. The net result is that the countercharge

37

from the solution effectively screens the surface charge so that on the global scale, the overall charge is zero. Characteristic thickness of this ion layer is given by

$$\lambda = \sqrt{\frac{\varepsilon k_B T}{2 z^2 q^2 n_0}} \tag{1}$$

where ε is the permittivity of the medium, k_B is Boltzmann's constant, T is the absolute temperature, z is the charge number of the ions, q is the charge of an electron, and n_0 is the number of ions per unit volume. λ is known as Debye length, which is usually in the order of 1-100 nm. For a typical 1 mM KCl (potassium chloride) solution, the calculated Debye length is 9.61 nm.

For ACEO, the relevant charges dominate in the double layers are no longer the naturally occurring surface charge (for DCEK) of the channel but are the induced charges from the bulk electrolyte to the electrode surface. Figure 3-1 shows how fluid flow is induced by ACEO. As shown in figure 3-1(a), AC signal with magnitude $\pm V$ are applied to two side by side electrodes, which gives rise to the electric field E with tangential component E_t outside the double layer and induced charges on the surface of each electrode. The induced charge in the double layer experiences a force F_q due to the interaction with the tangential electric field, resulting in fluid flow. The interaction of the tangential field at the surface with the charge in the double layer gives rise to a surface fluid velocity u_x and resulting in bulk flow due to fluid viscosity, as shown in figure 3-1(b). On the other half cycle of the signal, the induced charges in the double layer and electric fields change directions simultaneously, giving rise to a non-zero time averaged force and a steady-state flow pattern.
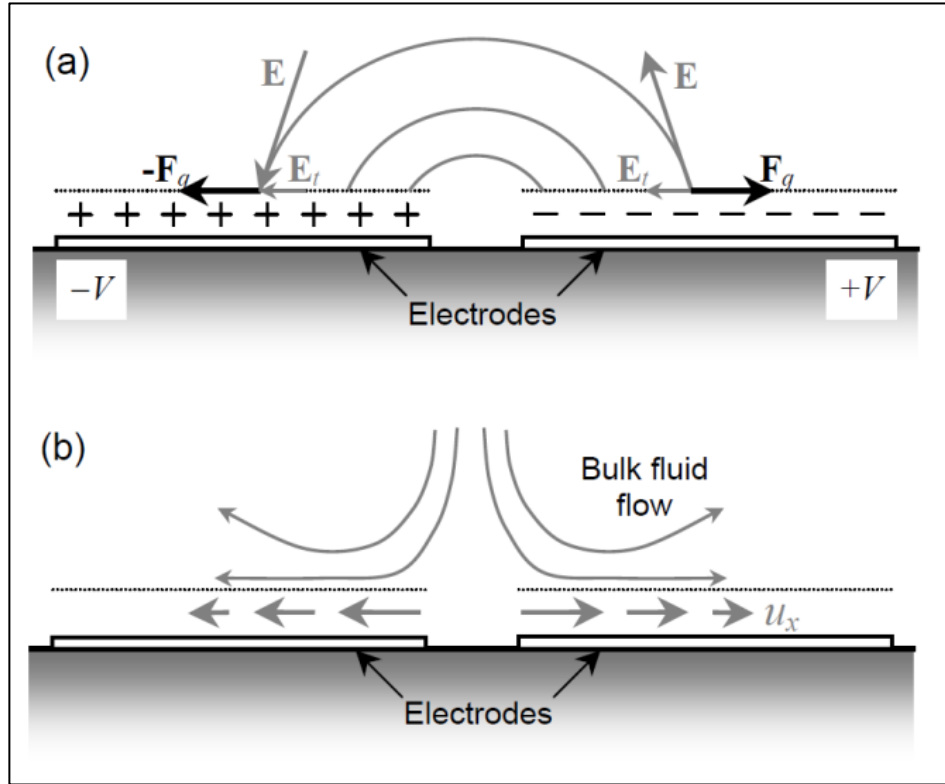
Figure 3-1. Mechanisms of AC electroosmosis. (a) AC signal is applied to the electrodes, resulting in the induced charge formation in the double layer and tangential electric field to drive the ions, (b) The interaction of the tangential field at the surface with the induced charge in the double layer gives rise to a surface fluid velocity u_x and a resulting bulk flow due to with fluid viscosity [1].

ACEO induced fluid velocity close to the electrode surface is expected to be proportional to the tangential field and the induced charge in the double. The velocity is then

$$u = -\frac{\varepsilon}{\eta}\Delta\phi_d \frac{d\phi}{dx} = -\frac{\varepsilon}{\eta}\Delta\phi_d E_x \tag{2}$$

where E_x is the tangential field outside the diffuse layer, ε is the permittivity of the medium, η is the viscosity of the fluid, and $\Delta\phi_d$ represents the difference between the potential on the outer side of the double layer and the potential on the inner side of this layer, at the no-slip plane, usually terms as zeta (ζ) potential.

The velocity of AC electroosmosis flow is frequency dependent. At very low frequencies all of the potential is dropped across the double layer and the tangential electric field outside the double layer is thus too small to generate flow. While at high frequencies, approaching the charge relaxation frequency σ/ε, the double layer has insufficient time to form and thus there is no charged fluid to interact with the electric field, resulting in zero flow. Experimental results [4] also showed that the velocity vs. frequency exhibits bell–shaped profile, with peak velocity at several hundred hertz to several kilo hertz, with respect to different solution conductivities.

ACEO capacitive charging process usually dominates at low applied frequency and voltage. Another electrode polarization process can also take place at low frequencies. When the electric field strength exceeds a certain threshold value, electrochemical reactions take place, and the surface charge polarities are inverted. Instead of the counter-ions that are induced by capacitive changing, co-ions are produced at the electrode and electrolyte interface, which is termed as Faradaic

charging. As a result, the electric fields tangential to the electrode drive the fluid towards the opposite direction because the signs of the charges change. Compared with capacitive charging, Faradaic charging can produce charge densities of several orders of magnitude beyond equilibrium values, resulting in stronger fluid flow. However, too high a voltage would degrade the electrodes and cause bubble generation, especially for high conductivity fluids.

In order to better understand the mechanisms lie behind each ACEK phenomena and determine optimum condition for implementation, the equivalent circuit can be extracted to represent the microfluidic system. Use parallel planar electrode for example, which is given in figure 3-2 [5], R_{lead} represents lead resistance, which arises from the thin film metal lines, bonding pads, etc, and therefore, they are in series with the electrolytic cell. C_{cell} accounts for direct capacitive coupling between the two electrodes. The value of C_{cell} depends on the dielectric properties of the electrolyte and electrode geometries. The bulk of the electrolyte obeys Ohm's law, so the bulk of the solution is modeled as a resistor R_{solu} in series with components at the interfaces of the electrodes and the electrolyte. R_{solu} is affected by the conductivity of the fluid. Two current-conducting mechanisms at the electrode/electrolyte interface are represented by different components. Hydrolyzed ions at the surface of metal electrodes cause a double layer capacitance, C_{dl}, which represents a capacitive charging process. There are also electrode reactions at the interface, which is represented by a battery and a resistor in the equivalent circuit for Faradaic charging, as shown in figure 3-2(b). If there is electrochemical reaction, electric charges are transferred across the interface in parallel
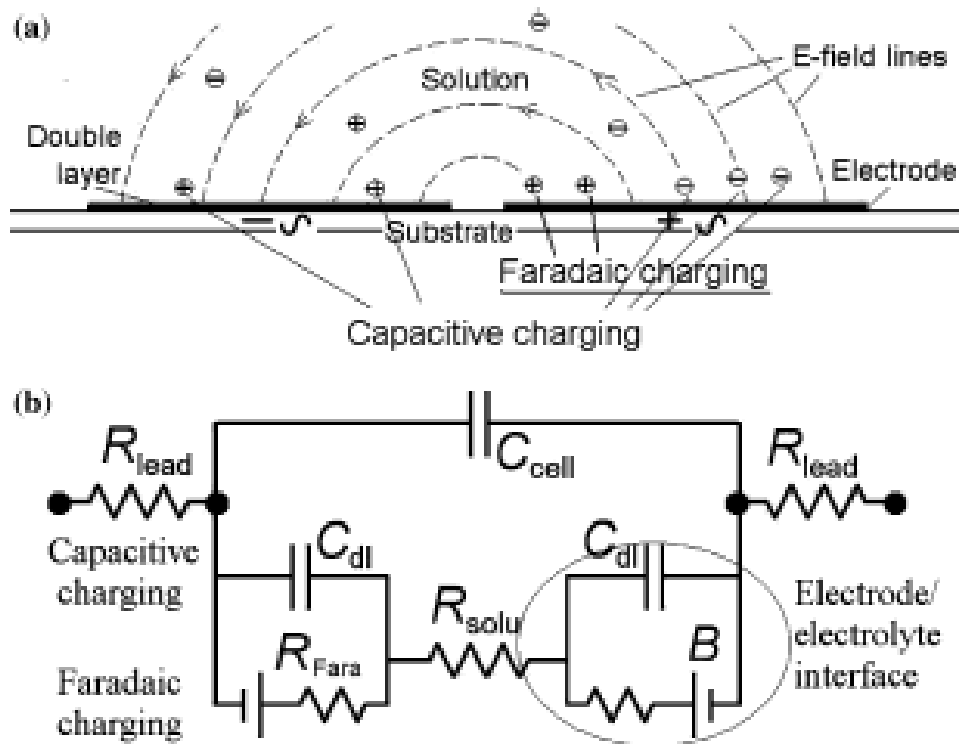
Figure 3-2. Equivalent circuit models for electrode/electrolyte system. (a) Capacitive charging for induced charges and Faradaic charging for electrochemical reaction, (b) equivalent circuit consisting of all the components that form the electrode/electrolyte interface [5].

to the charging of the double layer, so the Faradaic components are in parallel with C_{dl}.

3.1.2 AC Electrothermal effect (ACET)

ACEO is typically limited to fluids with low ionic strength. High conductivity solution compresses the thickness of the electric double layer, making electroosmosis ineffective.

Non-uniform electric fields produce spatially varying power densities in the fluid and therefore non-uniform temperature fields in the fluid. Temperature variations will lead to local gradients in electric conductivity and permittivity, which in turn induces free, mobile charges in the bulk of the fluid. The applied electric field interacts with the mobile charges, giving rise to electrothermal forces in the liquid, hence induce micro flows. This mechanism is termed AC electrothermal effect (ACET effect). Higher conductivity leads to higher fluid velocity due to increased heat generation and temperature gradients.

When the electric field E is applied to the fluid with conductivity σ, Joule heating of the fluid will occur. In the fluid, energy balance will be reached at steady state, according to energy balance equation

$$k\nabla^2 T + \frac{1}{2}\langle \sigma E^2 \rangle = 0 \qquad (3)$$

where k is the thermal conductivity, T is the temperature, and σ is the electric conductivity of the fluid. σE^2 represents the power density generated in the fluid by Joule heating from the applied electric fields.

43

Non-uniform electric field results in non-uniform heat generation, which leads to temperature gradients ∇T in the fluid. In turn, the temperature gradient produces spatial gradient in fluid conductivity and permittivity by

$$\nabla \varepsilon = \left(\frac{\partial \varepsilon}{\partial T}\right)\nabla T \qquad (4)$$

and

$$\nabla \sigma = \left(\frac{\partial \sigma}{\partial T}\right)\nabla T \qquad (5)$$

$\nabla \varepsilon$ and $\nabla \sigma$ induce mobile space charges ρ_e in the bulk fluid according to

$$\frac{\partial \rho_e}{\partial t} + \nabla \cdot (\sigma E) = 0 \qquad (6)$$

and

$$\rho_e = \nabla \cdot (\varepsilon E) \qquad (7)$$

As a result of fluid non-uniformity, electric fields can exert body force on induced space charges

$$F_{et} = \rho_e E - \frac{1}{2}|E|^2 \nabla \varepsilon \qquad (8)$$

The time averaged force is then

$$\langle F_{et} \rangle = -0.5(\frac{\nabla \sigma}{\sigma} - \frac{\nabla \varepsilon}{\varepsilon})\frac{\varepsilon |E|^2}{1+(\omega \tau)^2} - \frac{1}{4}|E|^2 \nabla \varepsilon \qquad (9)$$

where σ and ε are the electrical conductivity and permittivity of the medium, $\tau = \varepsilon/\sigma$ is called charge relaxation time, and $\omega = 2\pi f$ is radian frequency. Equation (9) can be rewritten as

$$F_{et} = -0.5\left[(\frac{\nabla\sigma}{\sigma} - \frac{\nabla\varepsilon}{\varepsilon})E_0\frac{\varepsilon E_0}{1+(\omega\tau)^2} + 0.5|E_0|^2\nabla\varepsilon\right] \qquad (10)$$

E_0 is the magnitude of the applied electric field. The first term in equation is the Coulomb force, and is dominant at low frequencies. The second term is the dielectric force, and is dominant at high frequencies. The crossover frequency scales inversely with the charge relaxation time of the fluid. Well below the crossover frequency ($\omega \ll \tau$), the electrothermal force is dominated by the first term in equation (10) and scales according to

$$\vec{F}_{et} \sim (\nabla T \cdot \vec{E})\vec{E} \qquad (11)$$

Since the temperature scales with E^2, this relation reveals a 4th power dependence of electrothermal force on E. this indicates a small increase in applied voltage can result in a large increase in velocity.

For aqueous media at 293K, we have

$$\frac{1}{\varepsilon}\frac{\partial\varepsilon}{\partial T} = -0.004 \Rightarrow \frac{\nabla\varepsilon}{\varepsilon} = \frac{1}{\varepsilon}\frac{\partial\varepsilon}{\partial T}\nabla T = -0.004\nabla T \qquad (12)$$

and

$$\frac{1}{\sigma}\frac{\partial\sigma}{\partial T} = 0.02 \Rightarrow \frac{\nabla\sigma}{\sigma} = \frac{1}{\sigma}\frac{\partial\sigma}{\partial T}\nabla T = 0.02\nabla T \qquad (13)$$

Giving

$$\langle F_{et}\rangle = -0.012\cdot\nabla T\cdot\frac{\varepsilon|E|^2}{1+(\omega\tau)^2} + 0.001\cdot\nabla T\cdot\varepsilon|E|^2 \qquad (14)$$

From the above equation (14), it can be deducted that the fluid body force F_{et} follows the direction of electric field and is proportional to the temperature gradient ∇T. The fluid behavior is governed by Navier-Stokes equation

$$\rho \frac{\partial u}{\partial t} + \rho(\nabla \cdot u)u - \eta \nabla^2 u + \nabla P = F_{et} \qquad (15)$$

where ρ is the fluid density, η is the dynamic viscosity, P is the external pressure and u is the velocity of the fluid. Together with $\nabla \cdot u = 0$ for incompressible fluid, fluid velocity can be determined for ACET flow.

ACET effect is ubiquitous as long as electric current flows through fluid. And it is also frequency dependent like ACEO. From the impedance analysis, one can determine the optimum frequency for ACET effect. Figure 3-3 shows a typical impedance measurement of a side by side electrode configuration in microfluidic channel. Fluid
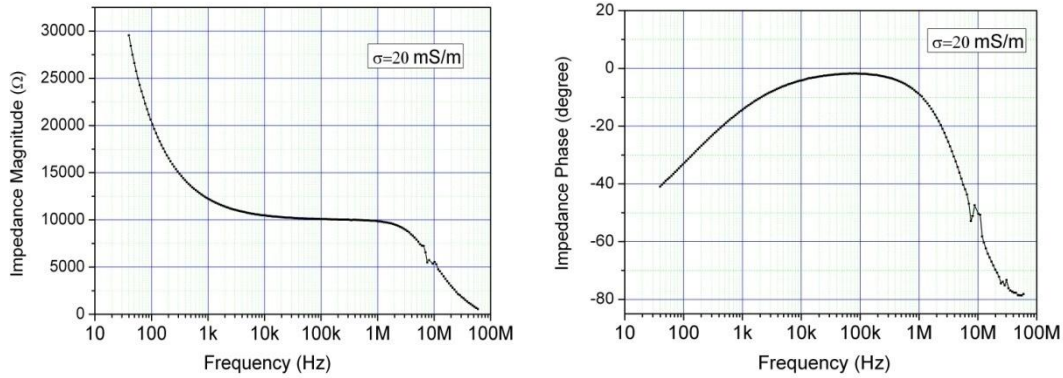
Figure 3-3. Impedance measurement of an electrode pair in microfluidic channel with σ=20 mS/m. The measurement is excited by 0.5 volt signal. Magnitude and phase information are plotted separately.

conductivity is 20 mS/m. Impedance data is obtained with Agilent 4294a Precision Impedance Analyzer. Magnitude and phase information are plotted separately.

So in order to maximize ACET effect, operating frequency is chosen so that impedance is most close to resistive nature.

3.1.3 Dielectrophoresis (DEP)

While ACEO and ACET effect are the mechanisms of fluid flow, dielectrophoresis (DEP) [6-9] is a phenomenon in which a force is exerted on a dielectric particle when it is subjected to a non-uniform electric field. The strength of the force depends strongly on the medium and particle's electrical properties, on the particle's shape and size, as well as on the frequency of the electric field. Consequently, fields of a particular frequency can manipulate particles with great selectivity. This has allowed the separation of cells or the orientation and manipulation of bio/nano-particles.

DEP force does not require the particle to be charged. When a small particle is suspended in an aqueous electrolyte (such as potassium chloride, KCl), in the presence of an applied electric field, charges are induced at the interface between the particle and the electrolyte, as shown schematically in figure 3-4. The amount of charge at the interface depends on the field strength and the electrical properties (conductivity and permittivity) of both the particle and the electrolyte.

Figure 3-4 shows the induced charge distribution in particle surface by symmetric electrodes. When the polarisability of the particle and electrolyte are the same, it is as if the particle does not exist and the field lines are parallel and continuous everywhere.

47
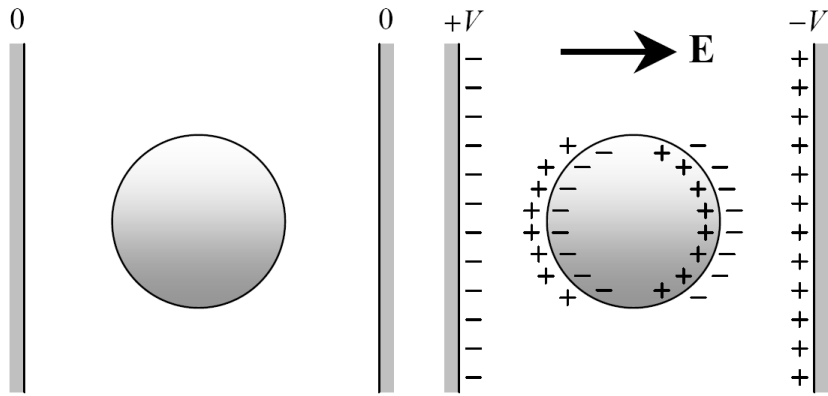
Figure 3-4. Schematic diagram of how a dielectric particle suspended in an aqueous electrolyte polarizes in a uniform applied electric field E [1].

Consider the same particle subjected to a non-uniform electric field generated by asymmetric electrode pair, as shown in figure 3-5. The electric field is non-uniform, and the distribution of induced charges at the particle surface is non-uniform as well, thus the electric field will have a net force onto the particle. In figure 3-5(a), when the particle is more polarisable than the medium, it will move towards higher field region, and this is defined as positive DEP (p-DEP). When the particle is less polarisable than the mdeium, it will move towards lower field region, which is termed as negative DEP (n-DEP), as shown in figure 3-5(b). Simulation is done with Comsol Multiphysics software.

Under AC electric field, complex permittivity is used to describe the frequency dependent response of the dielectric to the field. It consists of both real and imaginary parts, which is given in the expression below

$\sigma_m = 10^{-4} S/m$

$\sigma_p = 1 S/m$

$\sigma_m < \sigma_p$

Particle more polarisable

$\sigma_m = 10^{-4} S/m$

$\sigma_p = 10^{-6} S/m$

$\sigma_m > \sigma_p$

Particle less polarisable
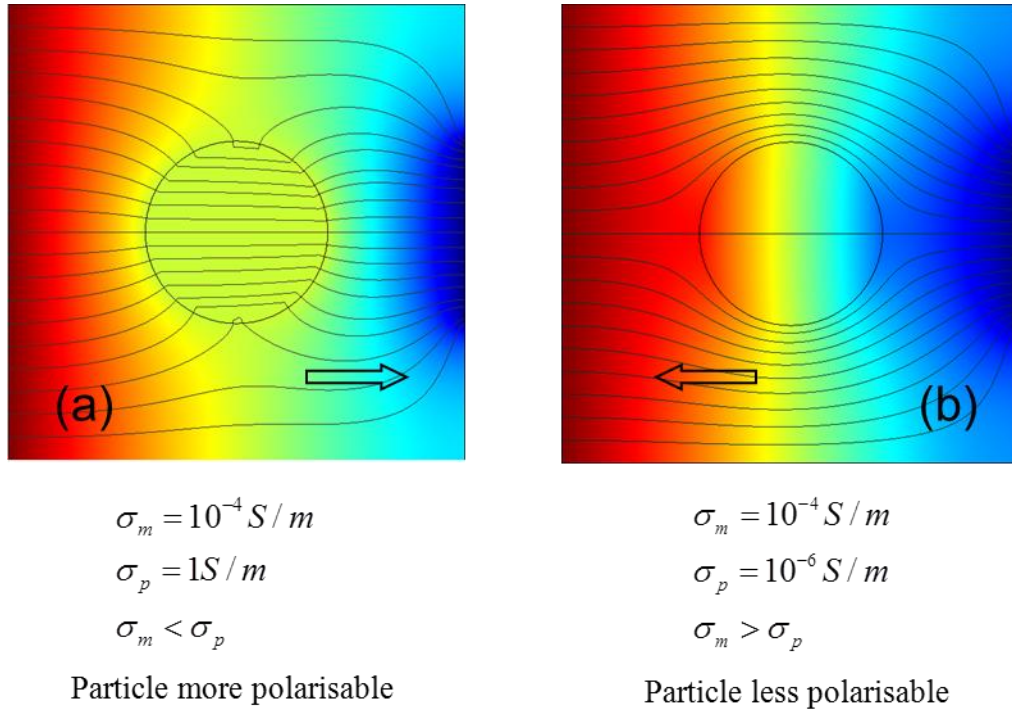
Figure 3-5. Numerical simulations of electric field distribution by asymmetric electrodes with (a) particle more polarisable (b) particle less polarisable than the suspending medium. Positive (left plot) and negative (right plot) DEP are defined according to whether the particle is more polarisable than the medium or not. Arrows in the plot indicate the movement of particles and stream lines indicate electric field distribution.

$$\tilde{\varepsilon} = \varepsilon_0 \varepsilon_r - i \frac{\sigma}{\omega} \qquad (16)$$

In practical, a dipole moment forms due to the interaction of a polarisable particle and electric field. In a non-uniform electric field the force imbalance on the dipole moves the particle. The effective dipole moment of a spherical particle is given

$$p = 4\pi\varepsilon_m \left(\frac{\tilde{\varepsilon}_p - \tilde{\varepsilon}_m}{\tilde{\varepsilon}_p + 2\tilde{\varepsilon}_m} \right) a^3 E \qquad (17)$$

Clausius-Mossotti factor (CM factor)

$$K(\omega) = \frac{\tilde{\varepsilon}_p - \tilde{\varepsilon}_m}{\tilde{\varepsilon}_p + 2\tilde{\varepsilon}_m} \qquad (18)$$

is used to describe the effective dipole moment of the particle, where m denotes medium and p denotes particle, which is frequency dependent according to equation (16).

The real part of the CM factor reaches a low frequency limiting value

$$f \to 0 \Rightarrow K(\omega) \to \frac{\sigma_p - \sigma_m}{\sigma_p + 2\sigma_m} \qquad (19)$$

which depends solely on the conductivity of the particle and suspending medium. Conversely, the high frequency limiting value is dominated by the permittivity of the particle and suspending medium

$$f \to \infty \Rightarrow K(\omega) \to \frac{\varepsilon_p - \varepsilon_m}{\varepsilon_p + 2\varepsilon_m} \qquad (20)$$

CM factor has strong influence on the particle behavior responding to electric field. For a spherical particle, the variation in the magnitude of the force with

frequency is given by the real part of the CM factor. The time average of the DEP force on a spherical particle is given by

$$\langle F_{DEP}(t) \rangle = 2\pi\varepsilon_m a^3 \, \text{Re}\big[K(\omega)\big] \nabla |E_{rms}|^2 \tag{21}$$

From the equation, we can see the magnitude of the force depends on the particle volume, the permittivity of the suspending medium, and gradient of the field square. From equation (19) and (20), the low frequency (<50 kHz) DEP force arising from interfacial polarization thus depends on the conductivity properties of the particle and suspending medium, whilst at high frequencies (> 50 MHz) the permittivity vlaues are important. At intermediate frequencies, both the conductive and the dielectric properties of the medium and particle dictate the magnitude and polarity of the force. So the sign of the real part of CM factor decides whether the particle acts as positive or negative DEP

$$F_{DEP} \propto \nabla |E_{rms}|^2 \propto \frac{V^2}{r^3} \tag{22}$$

As equation (22) indicates, DEP force scales with the square of the voltage and inversely with the cube of the distance, so that decreasing the characteristic dimensions of the electrode by one order of magnitude can lead to three orders of magnitude increase in the DEP force. This means that DEP effect is short range sensitive, and this is a clear advantage for using microelectrodes with small spacing apart.

For a sphere particle, the real part of the CM factor is bounded by the limit $-0.5 < \text{Re}[K(\omega)] < 1$ and varies with the frequency of applied field and the complex permittivity of the medium.

Equation (21) applies to spherical, homogenous particles. But most particles, especially biological ones, are not homogenous. Bacteria and cells can be modeled to take account of their heterogeneous structures using the so-called multishell model, as illustrated in figure 3-6 [9].

Cross-over frequency for micro-particles, especially biological cells, is an important characteristic parameter in the study of their DEP behavior. An example of DEP frequency response of a viable cell is shown in figure 3-7. At cross-over frequency, the effective dielectric properties of the cell exactly balance those of the suspending medium, so that the DEP force is zero. Also, this is the frequency when DEP force changes sign, either from negative to positive DEP or from positive to negative DEP. If we know and can control the dielectric properties of the suspending medium, we can deduce and also control the DEP behavior of the suspended cells or particles. This has important implications for applying DEP to characterize and selectively manipulate cells. The formula for calculating the cross-over frequency can be derived by setting $\mathrm{Re}\big[K(\omega)\big]=0$, we have

$$f_{xo} = \frac{1}{2\pi} \sqrt{\frac{(\sigma_m - \sigma_p)(\sigma_p + 2\sigma_m)}{(\varepsilon_p - \varepsilon_m)(\varepsilon_p + 2\varepsilon_m)}} \tag{23}$$

The value of f_{xo} depends principally on the cell radius and membrane capacitance. Since it is hard to measure conductivity and permittivity of the particles, the cross-over frequency is usually determined in the experiment by observing the particle motion change as the direction change of the DEP force.
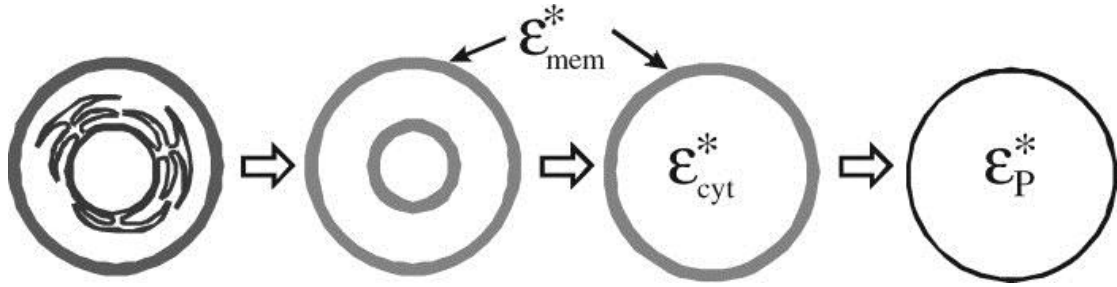
Figure 3-6. Schematic representation of how a nucleated cell can progressively be simplified to a homogeneous sphere of effective permittivity $\varepsilon_p{}^*$ that mimics the dielectric properties of the nucleated cell. The first step in simplification shown is to represent the endoplasmic reticulum as a topographical feature that increases the effective capacitance of the nuclear envelope. The penultimate step represents the cell as a smeared-out cytoplasm surrounded by a membrane of complex permittivity ε_{cyt}^* and ε_{mem}^*, respectively [9].
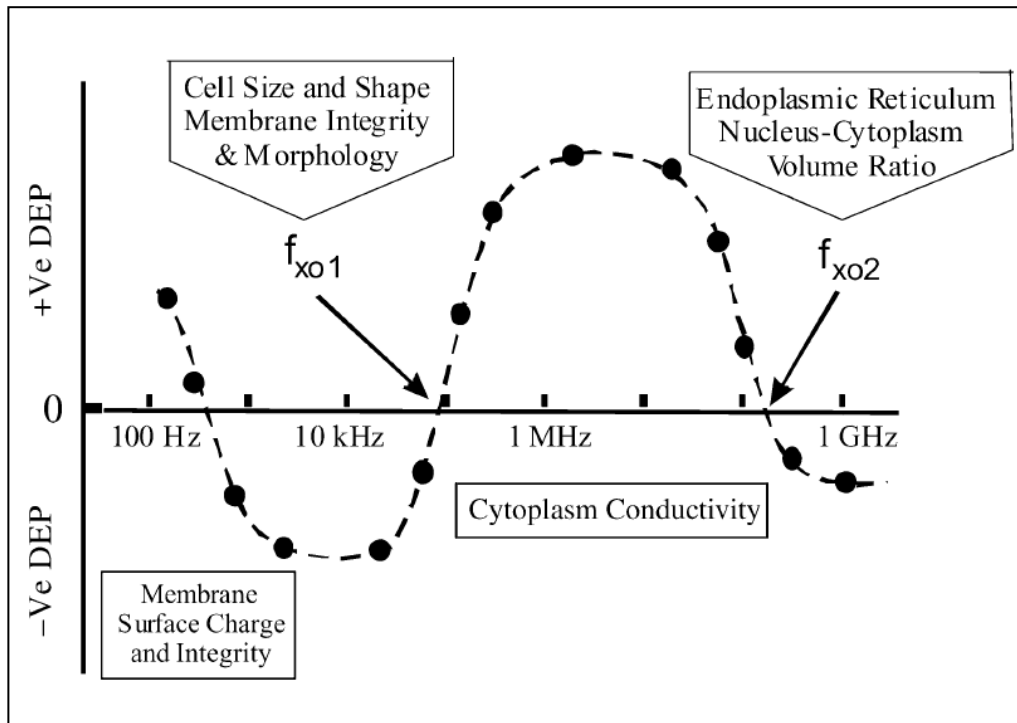
Figure 3-7. The DEP frequency response exhibited by a viable cell is characterized by two "crossover" frequencies f_{xo1} and f_{xo2} whose values are determined by the various cell parameters listed in the figure. Membrane surface charge and the physical integrity of the membrane influence the behavior below 1 kHz, whilst the cytoplasm conductivity is an important factor for frequencies between about 100 kHz and 100 MHz [7].

3.2 Review of particle dynamics in aqueous solution

Bioparticles have sizes that range from 0.1 μm up to 10 μm, e.g. viruses (0.01-0.1 μm), bacteria (0.5-5 μm), or plant or animal cells (5-15 μm). They are usually suspended in an aqueous saline solution with a conductivity that ranges between 10^{-4} and 1 S/m. Typical system lengths of the microelectrodes (interelectrode gaps) used in the manipulation of bioparticles vary from 1 to 500 μm. The signals applied to these electrodes can be up to 20 volt, giving rise to electric fields that can be as high as 10^6 V/m. the applied signals have frequency in the range 10^2-10^8 Hz. This section reviews particle dynamics in aqueous solution.

When a particle is suspended in aqueous solution, it experiences various forces [10-12]. These forces include viscous drag, gravity, Brownian, dielectrophoretic, and hydrodynamic forces. An electrical field can also induce fluid motion that will drag the particle which is termed electrohydrodynamic (EHD) force, including electroosmosis (EO) and electrothermal (ET) forces.

A particle moving in the fluid experiences a drag force (a.k.a. Stokes force) –*fv* where *v* is the velocity of the particle and *f* is the friction factor of the particle. The friction is related to particle size, shape, and surface characteristics of the particle. For a smooth spherical particle, *f=6πηa*, where *a* is the radius and *η* is the viscosity of the medium. Following a constant force F at time t=0, the solution for the time dependence of the velocity is

$$v = \frac{F}{f}(1 - e^{-(f/m)t}) \tag{24}$$

where m is the mass of the particle. The velocity of the particles increases until it reaches a constant terminal velocity. For cells and submicron particles, the characteristic time $\tau_a = m/f$ is smaller than 10^{-6} s. Therefore, the particle can be considered to move at its terminal velocity $v_t = F/f$. We can assume that particle will respond to external force instantly, and any change in measured velocity is simply proportional to a change in the force.

The main external influence on a particle suspended in a fluid is gravity. For a particle of mass density ρ_p in a fluid of density ρ_m, the gravitational force is given by

$$F_g = v(\rho_p - \rho_m)g \tag{25}$$

where g is the acceleration due to gravity and v is the volume of the particle. Considering friction factor $f = 6\pi\eta a$, the magnitude of the velocity of a spherical particle in a gravitational field is

$$F_g = \frac{v(\rho_p - \rho_m)g}{f} = \frac{2}{9}\frac{a^2|\rho_p - \rho_m|g}{\eta} \tag{26}$$

To a first order approximation, assume $|\rho_p - \rho_m|$ is of the order of ρ_m, the magnitude of the gravitational velocity can be estimated to be

$$u_g \sim 0.2\frac{a^2\rho_m g}{\eta} \tag{27}$$

For submicron particles, gravitational force is usually negligible but can be seen over long periods of observation (sedimentation).

Thermal effects also influence colloidal particles. Brownian motion (named after the Scottish botanist Robert Brown) is the seemingly random movement of particles suspended in a fluid. The force and velocity associated with Brownian motion have zero average. However, the random displacement of the particle follows a Gaussian profile with a root-mean-square displacement (in one dimension) given by

$$\Delta x = \sqrt{2Dt} = \sqrt{\frac{k_B T}{3\pi a \eta} t} \tag{28}$$

where D is the diffusion constant of particle, k_B is Boltzman's constant, T is absolute temperature, and t is the period of observation. To move an isolated particle in a deterministic manner during this period, the displacement due to the deterministic force should be greater than that due to the random (Brownian) motion.

A temperature gradient gives rise to a change in fluid density and thus natural convection is to be expected. The magnitude of this effect (buoyance force) is given by

$$f_g = \nabla \rho_m g = \frac{\partial \rho_m}{\partial T} \Delta T g \tag{29}$$

If buoyance force is caused by Joule heating, a typical velocity magnitude for a buoyance force (by numerical simulation) is

$$u_{max} \sim 2 \times 10^{-2} (\frac{\partial \rho_m}{\partial T}) \frac{\sigma V^2 g r^2}{k \eta} \tag{30}$$

where V is applied ac voltage, r is characteristic length, and k is the thermal conductivity of the fluid.

Particles in electric fields are subjected to dielectrophoretic forces. Details of DEP have been discussed in section 3.1.3. Assume that the instantaneous velocity is

57

proportional to the instantaneous dielectrophoretic force, DEP velocity can be obtained by DEP force (Eqn. (21)) divided by a friction factor $f=6\pi\eta a$. For spherical particle, DEP velocity is given as

$$v_{DEP} = \frac{F_{DEP}}{f} = \frac{2\pi\varepsilon_m a^3 \operatorname{Re}\left[K(\omega)\right]\nabla\left|E_{rms}\right|^2}{6\pi\eta a} = \frac{\varepsilon_m a^2 \operatorname{Re}\left[K(\omega)\right]\nabla\left|E_{rms}\right|^2}{3\eta} \quad (31)$$

According to equation (22), assuming CM factor of 1, the magnitude of the DEP velocity of a particle in a typical co-planar electrode system (figure 3-1), at a distance r from the electrode center, is given

$$u_{DEP} \sim 0.03 \frac{a^2\varepsilon}{\eta}\frac{V^2}{r^3} \quad (32)$$

Electrohydrodynamic forces, such as ACEO and ACET forces, can induce fluid motion that will drag the particles due to Stokes force. Reference [12] gives estimation of particle velocity under ACEO and ACET effect.

Particle velocity influenced by ACEO flow is given by

$$u_{ACEO} \sim 0.1\Lambda \frac{V^2\varepsilon}{\eta r}\frac{\Omega^2}{(1+\Omega^2)^2}, \ \Omega=\Lambda\frac{\omega\varepsilon\pi r}{2\sigma\lambda_D}, \ \Lambda = \frac{C_s}{C_s+C_D} \quad (33)$$

where λ_D is Debye length, C_s and C_D are capacitances in Stern and diffuse layer, which form the electric double layer.

Particle velocity influenced by ACET flow (Joule heating) is given by

$$\begin{aligned} u_{\max_{\varepsilon\omega/\sigma\gg1}} &\sim 5\times10^{-4}\frac{\varepsilon\sigma V^4}{k\eta r}\left|\frac{1}{\sigma}\frac{\partial\sigma}{\partial T}\right| \\ u_{\max_{\varepsilon\omega/\sigma\ll1}} &\sim 2.5\times10^{-4}\frac{\varepsilon\sigma V^4}{k\eta r}\left|\frac{1}{\varepsilon}\frac{\partial\varepsilon}{\partial T}\right| \end{aligned} \quad (34)$$

And particle velocity influenced by incident light source (external heat source) is given

$$u_{light} \underset{\varepsilon\omega/\sigma\ll1}{\sim} 3\times10^{-3}\frac{\varepsilon V^2}{\eta}\left|\frac{\partial T}{\partial y}\right|\left|\frac{1}{\sigma}\frac{\partial\sigma}{\partial T}\right| \tag{35}$$

Figure 3-8 shows displacement of a particle under each force mentioned (equations 27, 28, 30, 32, 33, 34, and 35) for a time of 1 second in an electrolyte with conductivity 10^{-2} S/m, plotted as a function of particle radius [12]. Particle displacement is determined by particle size, as well as applied signal frequency and magnitude.
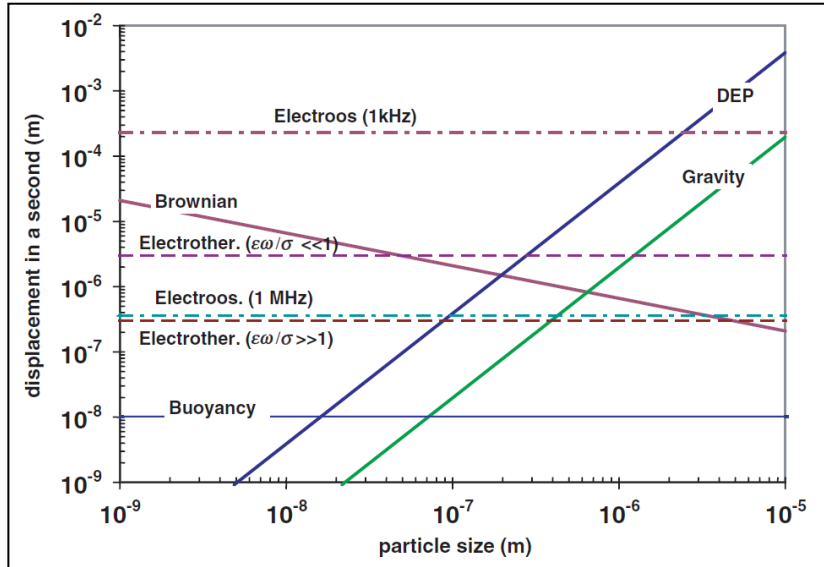
Figure 3-8. Particle displacement influenced by various forces in 1 second versus particle radius (V=5 volt, r=25 μm, σ=0.01 S/m) [12].

Chapter Four: Numerical Study and Optimization of In Situ Preconcentration for Rapid and Sensitive Nanoparticle Detection

Mass transfer over reactive surfaces in microfluidic devices is central to exploring and quantifying biochemical reactions, such as DNA hybridization and antigen-antibody binding. Reference [1] and [2] give conprehensive and fundamental study of different regimes of diffusion and laminar flow convection combined with bimolecular surface reactions relevant to biochemical assays performed in microfluidic devices.

It has been discussed in chapter one that flow-through system alone has limited effect to enhance surface binding since flow in microfluidic devices is always confined to laminar flow region. In order to enhance surface reaction, a pair of stirring electrodes is placed besides the sensor in the detection. When excited with ac signal, AC electrothermal (ACET) effect would generate vortices that will give active guidance of targets towards the sensor. This chapter presents a numerical study and optimization of an in situ preconcentor for rapid and sensitive nanoparticle detection. Most of the results are published in reference [3], and additional data and discussions are provided.

4.1 Simulation setups

The proposed preconcentrator consists of a flow-through microchannel with a pair of micro-stirring ACET electrodes integrated on its bottom. The sensor is to be placed

in the gap between the two electrodes. The 2D side view of the preconcentrator is shown in figure 4-1.

The characteristics of the designed preconcentrator were studied with finite-element analysis software COMSOL Multiphysics. The height of the microchannel, H, will vary in the simulation to study their effects on the performance of the preconcentrator. The sensor width is denoted as L, which can vary from micron to submicron sizes. The two stirring electrodes are 20 μm in width, and the spacing between them is set at 5 μm, which is sufficient to accommodate most nano- to micro-sensors. Sample solution at a concentration of 1 fM (femtomolar) is pressure-driven in from the left boundary, assuming a parabolic profile with a mean velocity of uin (peak velocity in the middle of the channel with $1.5 \times u_{in}$) at inlet. The flow exits the chamber at the right boundary.

The simulation of ACET stirring involves several physical modules including
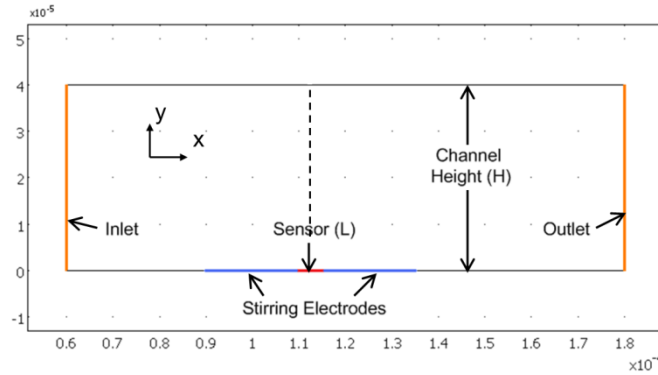
Figure 4-1. Schematic of the preconcentrator in numerical simulation (2D side view). Sensor is placed between two stirring electrodes. Fluid with a given target concentration flows in from left boundary and exit on the right boundary.

61

electrostatics, heat transfer, Navier-Stokes, and convection-diffusion models. For the boundary conditions in electrostatics module, electrodes are given electrical potential, while other boundaries are electrically insulated. For thermal boundaries (Convection and Conduction module), metal electrodes are set at room temperature, as they are good thermal conductor, while the top and bottom of the channels are assumed thermal insulation (bottom glass substrate and top polymer channel wall). Although very small, convective heat flux boundary conditions are applied to the inlet and outlet boundaries. For fluid dynamics (Incompressible Naiver-Stokes module), both top and bottom channel walls assume no-slip boundaries. Parabolic pressure driven flow profile is applied to left inlet boundary. Fluid exits the outlet boundary with zero normal stress. In the simulation, electric field is solved first, and then thermal field and flow velocity field are solved simultaneously since they are coupled in the equations.

With solved flow velocity field, diffusion and convection module and surface reaction module are solved for the concentration effect on the sensor. The distribution (convection and diffusion) of the target molecules within the microchannel can be described as

$$\frac{\partial c}{\partial t} + \vec{u}\nabla c = D\nabla^2 c \qquad (36)$$

where c is the molecule concentration, u is the fluid velocity and D is the diffusivity of the antigen. When a target molecule strikes the sensor surface, it will be immobilized by surface modification such as antigen-antibody docking. On the sensor surface, we assume a first order reaction profile

$$\frac{\partial B}{\partial t} = k_{on}c_s(b_m - B) - k_{off}B \tag{37}$$

where b_m is the surface concentration receptors on the sensor. c_s is the target concentration on sensor surface and k_{on} and k_{off} are reaction and dissociation constants, respectively. The binding rate of the molecules to the sensor surface must be balanced by the diffusive flux of molecules at the binding surface. This boundary condition along with equation (36) and (37) determine the molecule distribution in the channel and on the sensor.

At the left inlet boundary, concentration is fixed at 1 fM. The outlet boundary is set as convective flux. On the sensor surface, according to equation (37), first order reaction is assumed, with k_{on}=10^8 m^3/ (mol*s), k_{off}=0.02, total receptors on the sensor is b_m=1.67×10^{-8} mol/m^2. Diffusivity of target molecule is 10^{-11} m^2/s, which is typical for single stranded DNA. The total concentration accumulated can be found by integration unit point concentration over the whole sensor surface. Parameters used in the simulation are comparable to the values in a real world setting, as given in table 4-1.

Whether the system is diffusion limited or reaction limited can be determined by sensor and channel characteristics, represented as Damköhler number Da (reaction velocity over diffusion velocity). Our model applies to a strongly diffusion limited case, since calculated Da ($k_{on}b_mH/D$, H is characteristic channel height) is much greater than 10, which is in agreement with other groups' results.

In the simulation, external forces on the particle have been considered, and the particle size is assumed to be 0.1 μm in diameter. The forces include dielectrophoretic force, for which positive DEP is assumed with a Clausius -Mossotti factor of 1. No

Table 4-1. Device parameters used in the simulation.

Parameter	Value [unit]	Description
ε_r	80.2	Relative permittivity of fluid
k	0.598 [W/(m*K)]	Thermal conductivity of fluid
ρ	1000 [kg/m3]	Density of fluid
C_p	4.184 [kJ/(kg*K)]	Heat capacity of fluid
η	1.08×10^{-3} [Pa*s]	Dynamic viscosity of fluid
σ	0.36 [S/m]	Electric conductivity of fluid (BSA in PBS)
D	10^{-11} [m^2/s]	Diffusion coefficient of analyte
f	100 [kHz]	AC signal frequency
c	10^{-12} [mol/m^3]	Analyte concentration at the inlet (1 fM)
k_{on}	10^8 [m^3/(mol*s)]	Association rate constant
k_{off}	0.02 [1/s]	Dissociation constant
b_m	1.67×10^{-8} [mol/m^2]	Total surface concentration of antibody ligand
V	variable	Electric potential (RMS value)
u_{in}	variable	Average flow velocity at the inlet

difference in simulation results is observed between the models with DEP and without DEP effect. So it is safe to conclude that DEP force does not play any appreciable role in nanoparticle trapping. Another force considered is Saffman life force. Small particles in shear flow experience a lift force that is originated from the pressure variations around the particle, and this is call Saffman force. Its expression

$$F_{sa} = \left| u_f - u_p \right| \left[6.64\eta R^2 \sqrt{\frac{\rho_f}{\eta} \nabla \left(u_f - u_p \right)} \right] \tag{38}$$

indicates that Saffman force is a function of fluid viscosity η, density ρ_f, particle size R and velocity difference between particle (u_p) and fluid (u_f). This force is always perpendicular to the direction of flow, which means velocity gradient of horizontal flow will result in the vertical lift force. The effect of the force is taken into account in the simulation. With 8 Vrms ACET voltage, 1000 μm/s inlet velocity, concentration on the sensor is reduced by 0.0012% for nanoparticles. The calculation reveals that Saffman force is not a significant factor under our simulation conditions.

4.2 Results and discussions

Many parameters will contribute to the trapping of nanoparticles on the sensor, such as ACET signal strength, inlet velocity, channel height and diffusivity of target particles. In the following, the effect of each factor will be discussed.

4.2.1 Effect of ACET and Proof of concept

From equation (14) we can see that ACET effect is a function of signal frequency

and strength. Figure 4-2 gives a qualitative view of how ACET stirring would guide bio-molecules. Pseudo colors in figure 4-2(a) and (b) show electrical potential and thermal distribution in the channel, respectively. When excited by AC signal, non-uniform electric field is generated by the electrode pair, giving rise to ACET effect. At a fluid conductivity of 0.36 S/m and 10 Vrms signal (figure 4-2(b)), total temperature rise is around 7.6 Kelvin (shown in color bar), while maximum temperature gradient can reach as high as 20 K/μm.

Total flow pattern in the channel is a combination of pressure-driven flow and the induced ACET microflows. Figure 4-2 also shows simulated flow patterns for two different applied voltages (indicated by arrows in plots). The parameters used are H=40 μm and u_{in}=100 μm/s. In the simulation, particles representing bio-molecules are introduced to reveal the flow traces. It is obvious that ACET effect induces vortices that generate a vertical velocity component right above the sensor surface, and this can effectively convey particles toward the sensor. As a result, binding rate at the reaction surface is greatly enhanced.

The induced ACET vortices function as an adjustable aperture to constrict the target molecule streamlines to very close vicinity of the sensor surface so as to enhance binding. According to equation (14), ACET velocity increases rapidly with applied voltage ($\sim V^4$), so the vortices increase in size with voltage as well. As a result, the sample streams become more confined as they are squeezed by the vortices, and the aperture becomes smaller with increasing AC voltage. At a higher voltage (e.g. 10 Vrms in figure 4-2(b), compared with 6 Vrms in figure 4-2(a)), most of the target
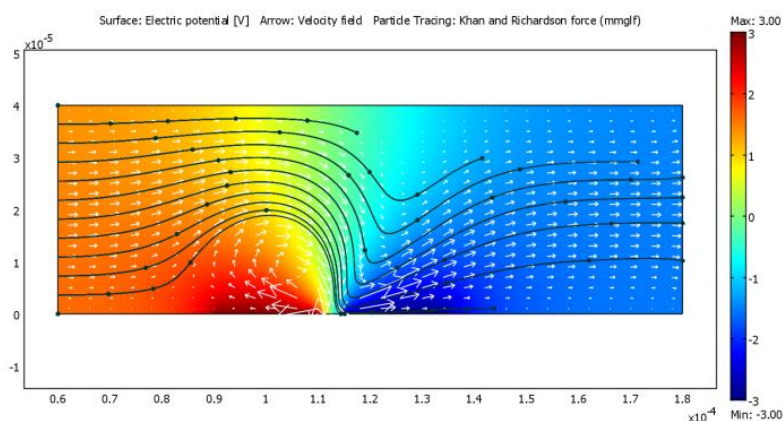
(a) 6Vrms 100μm/s inlet velocity
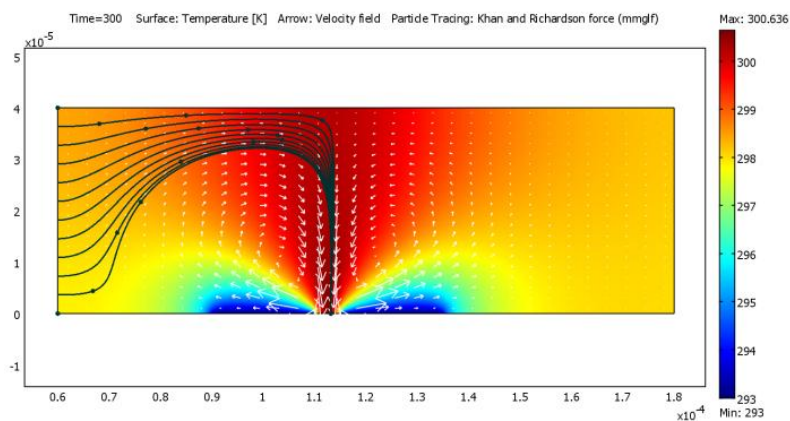
(b) 10Vrms 100μm/s inlet velocity

Figure 4-2. Simulated ACET flow fields for guiding bio-molecules. Electrode gap is 5 μm and channel height is 40 μm. Pump in velocity is 100 μm/s. (a) Applied voltage is 6 Vrms. Color shows electrical potential, and arrow shows microflows and their relative magnitudes. (b) Applied voltage is 10 Vrms. Color shows temperature distribution, and arrow shows microflows and their relative magnitude. Dots and lines in both plots show molecule traces, which are indications of ACET stirring effect.

67

particles are routed through the narrow pathway pinched by two vortices toward the sensor surface, and even those at the other side of the channel become captured. So increasing the voltage will enhance the molecule count on the sensor.

Cumulative concentration of bonded molecules can be integrated over time. Figure 4-3 shows the concentration effect by ACET stirring as a function of time. Channel height H=20 μm, inlet flow through velocity u_{in}=100 μm/s. With ACET effect, binding rate is shown to be increased by 9 times compared with flow through alone. Note that y-axis shows average concentration of bonded molecules on the sensor (point concentration on 2D model). Total concentration can be obtained by multiplying it with sensor area (width (L) x length). Note that the concentration on the sensor increases linearly since concentration on sensor is far from satuation (available trapping site b_m=1.67×10^{-8} mol/m^2). For real time detection, ACET stirring would greatly reduce incubation time, in the case above, by nine times.

4.2.2 Effect of flow through velocity

In the following, the combined effect of flow through velocity and ACET stirring is studied, and the results are shown in figure 4-4. The parameters used here are 20 μm channel height, 5 μm spacing between the ACET electrodes, and 5 μm sensor in width. Convection, diffusion and reaction processes are solved for 300 seconds using time-dependent solver. With given parameters, calculated Da number ($k_{on}b_mH/D$) is 3.3×10^6, which indicates strong diffusion limited nature. For easy comparison, the data points are normalized against the value at 0 Vrms and 0.1 μm/s inlet velocity. Reference

68
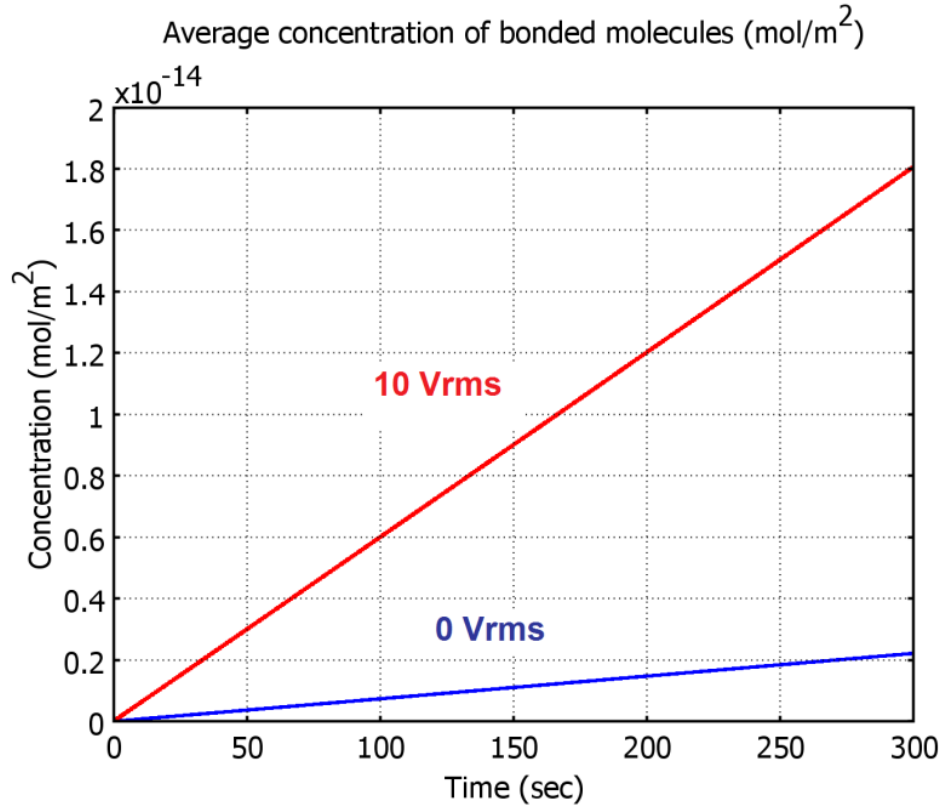
Figure 4-3. Binding rate as a function of time. With ACET stirring at 10 Vrms, concentration increased by 9x than with flow through alone. Channel height H=20 μm and inlet velocity u_{in} =100 μm/s. Unit of the ordinate is average concentration of bonded molecules on the sensor (point concentration on 2D model) taken at the end of 300 seconds.
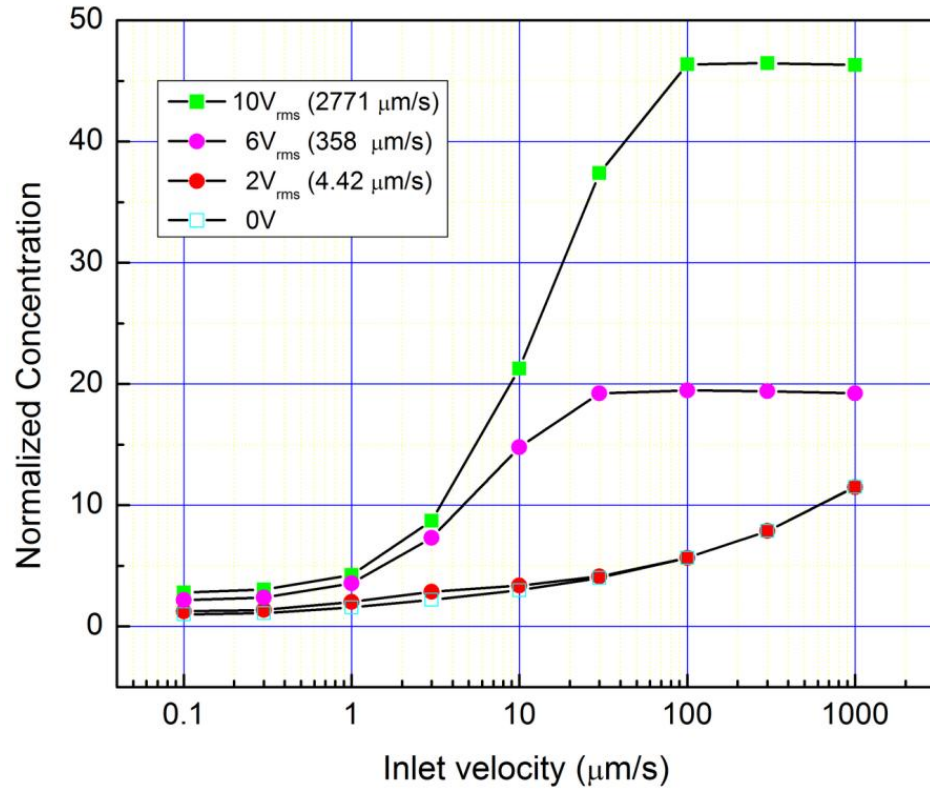
Figure 4-4. Concentration effect at different signal level against inlet velocity. The data points are normalized against the value at 0 Vrms and 0.1 μm/s inlet velocity. A reference velocity is given at each signal level in the legend showing a representative downward velocity generated by ACET effect.

velocities showing in the legend are the averaged downward (Vy) velocities in the middle of the channel above the sensor surfaceas an indicator of ACET velocity.

When there is no ACET stirring (0 V), increasing the inlet velocity by 1000 times (from 0.1 μm/s to 100 μm/s) only increases the concentration on the sensor by a factor of ~5.6. The preconcentration effect increases to above 10x at extreme high velocity like 1000 μm/s, which however is difficult to maintain due to high pressure required for small channels. This indicates that flow-through alone only have a limited effect on concentration. From figure 4-4, it can be seen that ACET stirring and flow-through will work together to increase the binding on the sensor. A higher ACET voltage will increase the binding rate. When the stirring is weak (2 Vrms ACET signal), the increase of concentration against inlet velocity is minimal. The 2 Vrms curve almost overlaps with the 0 Vrms curve. At the same 100 μm/s fluid velocity, a 6 Vrms ACET signal will provide a gain of 20 and 10 Vrms signal can reach a gain of 46, indicating the benefits of adding ACET stirring mechanism.

However, the improvement in concentration flattens out at high flow-through velocities. The concentration starts to saturate at 30 μm/s and 100 μm/s of flow-through velocity, for 6 Vrms and 10 Vrms AC signal, respectively. At very high flow through velocity, ACET flows can only carry the molecules into the compressed depletion region around the sensor to a limited extent. At increasing flow-through velocity, most of molecules simply get carried down the stream. So with ACET stirring, only a moderate flow-through velocity is needed, easing the requirements on pumping pressure and the strength of device bonding.

71

4.2.3 Effect of channel height

Channel height can affect ACET preconcentration in two ways. Firstly, the ACET velocity is determined by electric field strength and thermal gradient, so it is the strongest near the electrode edges (arrows in figure 4-2). The ACET flow gets weaker with its distance away from the electrodes. So beyond a certain height in the channel, ACET vortices cannot effectively guide the target molecules down towards the sensor. Besides, small channel diameter will reduce the distance that analytes are required to travel to the sensor. On the other hand, ACET flows can get suppressed at small hydraulic diameter. Therefore, the effect of channel height on the concentration needs to be investigated.

Simulation results on the effect of channel height are shown in figure 4-5, with three different signal strengths. The electrode separation is 5 μm and the sensor is also 5 μm wide, i.e. completely filling up the electrode gap. In almost all cases, concentration on the sensor increases with inlet velocity. Also there are two regimes. One regime is at low flow-through velocity where a larger channel will produce higher binding rate, and the other regime is at high flow-through velocity where a smaller channel will lead to higher binding rate.

Without ACET guidance (0 V), the capture of analyte molecule is dominated by diffusion. So above a reasonable flow-through velocity (>2 μm/s), a smaller channel height produces higher concentration on the sensor, since the channel constrains the sample solution to be closer to the sensor. While at very low inlet velocity (<2 μm/s), the fluid is almost at rest, target molecule has sufficient time to diffuse to the sensor.

(a)

(b)

(c)
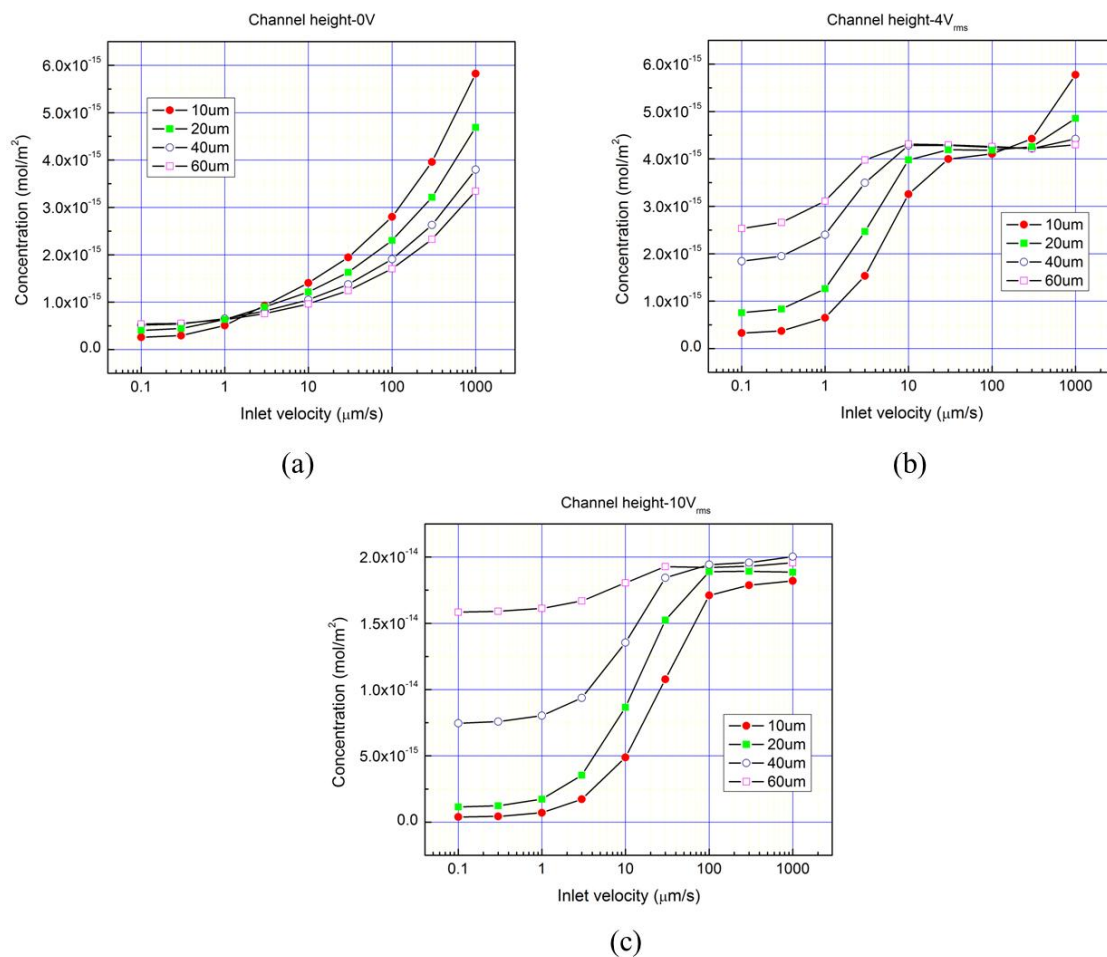
Figure 4-5. The effect of channel height on the sensor concentration with (a) ACET voltage at 0 V, (b) at 4 Vrms and (c) at 10 Vrms. Unit of the ordinate is point concentration (2D) accumulated on sensor surface.

So the sample depletion region above the sensor becomes thicker, and a higher channel will lead to a slightly higher concentration.

With ACET stirring (4 Vrms and 10 Vrms), it seems that the low velocity regime is extended to higher velocities with increasing ACET voltages (c.f. figure 4-5(b) and (c)). With 4 Vrms, the transition between the two regimes happens at 100~200 μm/s. Below 200 μm/s, a larger channel permits more effective mixing, hence higher capture rate at the sensor. At higher flow-through velocities, the data points start to coincide with those without ACET mixing (e.g. data at 1000 μm/s in figure 4-5(b)), and the binding rate is dictated by the flow through velocity. As the mixing strengthens rapidly with ACET voltage, at 10 Vrms, the binding process is dominated by ACET effect for most of the velocity range till above 1 mm/s.

It can also be observed that there is a plateau region for concentration, where binding rate is almost independent of flow through velocity. For example, at 4 Vrms with 60 μm channel, the binding rate stays almost the same from 30 μm/s to 1000 μm/s, and the similar is true with 10 Vrms ACET voltage. So by incorporating an ACET mixing mechanism, a larger channel and a slower flow rate can be used, which will reduce the pressure that microchannels have to sustain and ease the difficulty in fabrication.

The effect of channel height on concentration can be understood by studying the velocity profile at the center line between the two electrodes, indicated by dotted line in figure 4-1. The horizontal component Vx and vertical component Vy are plotted over the span of channel height for several sizes of channel, namely 2 μm, 5 μm, 10 μm, 20

μm and 40 μm. Vx is a superposition of inlet velocity and Vx of ACET flows, and Vy, the guiding flow for the targets, is solely attributed to the y-component of ACET flows. For all the curves in figure 4-6, the inlet velocity is set at 100 μm/s, which always exhibits a parabolic profile with peak velocity ($1.5u_{in}$ =150 μm/s) in the middle of the channel. The applied voltage is fixed at 10 Vrms with an electrode gap of 5 μm, if equation (14) alone is considered, the ACET velocities for all five heights would be the same.

From the development of Vy, it can be seen that channel height less than 20 μm will suppress ACET vortices, as the peak value of Vy keeps increasing till the channel height reaches 20 μm. This explains why in figure 4-5(c), the 10 μm channel height curve produces noticeably lower binding rate than the other larger channels. Calculations show that ACET vertical velocity Vy has peak value around 4 μm above the bottom, and the peak can be as high as 5800 μm/s if given enough channel height to develop the vortices. This peak velocity is orders of magnitude higher than inlet flow through velocity, which ensures the guiding ability of the vortices.

4.2.4 Effect of molecular diffusivity

For all the above discussions, target diffusivity is fixed at 10^{-11} m^2/s, which is a typical value for single stranded DNA sample. We have also studied the effect of diffusivity on ACET preconcentration, and the result is shown in figure 4-7. Equation (36) indicates the diffusivity will affect the distribution of concentration. Over a wide range of diffusivity from 10^{-13} to 10^{-9} m^2/s, improvement in binding rate can still be
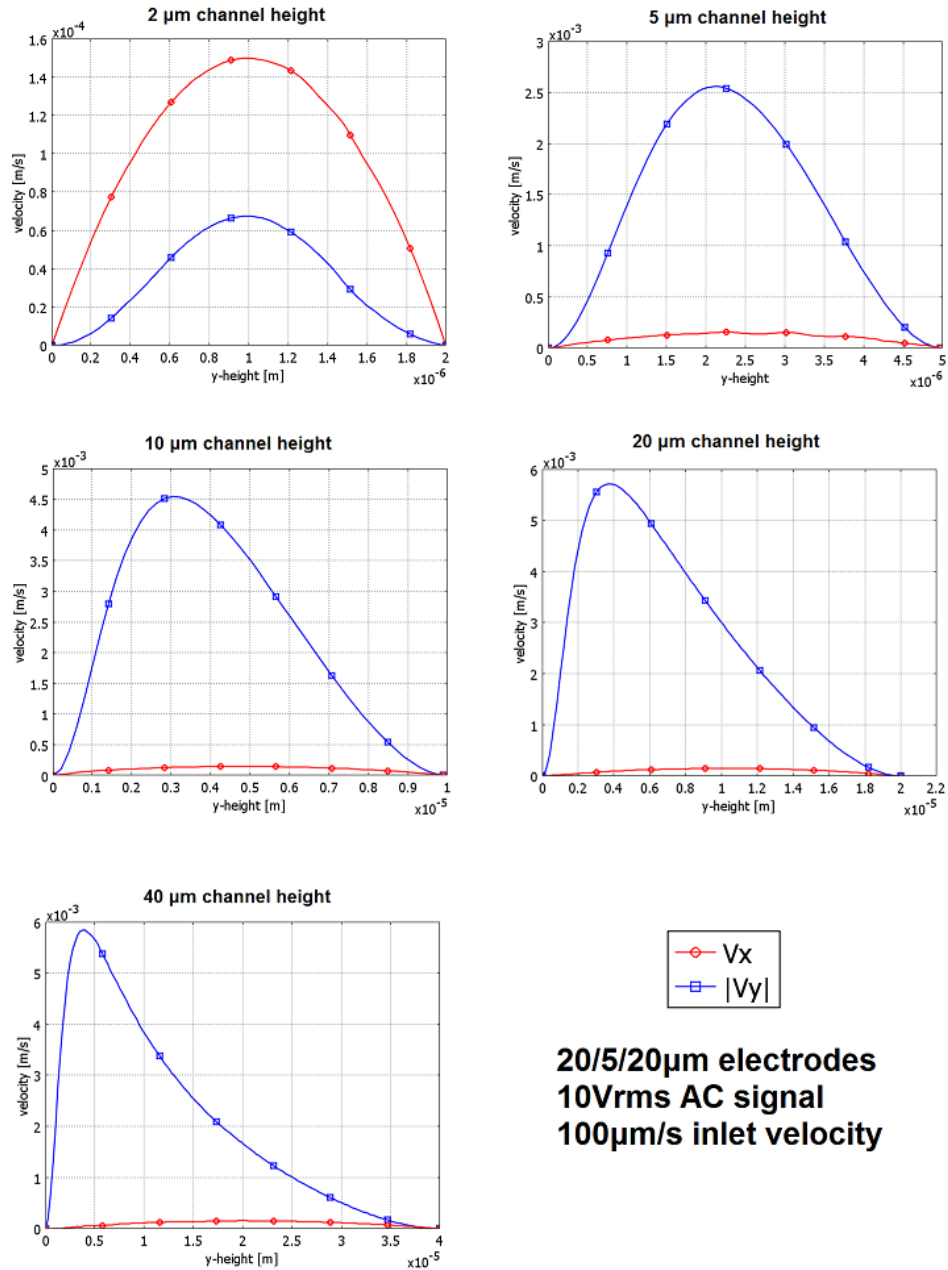
Figure 4-6. Cross-sectional fluid velocity along the centerline between the two electrodes, through the channel height. Vertical velocity is shown as blue square line and horizontal velocity is shown as red circle line. Inlet velocity is 100 μm/s and voltage is fixed at 10 Vrms for all cases.
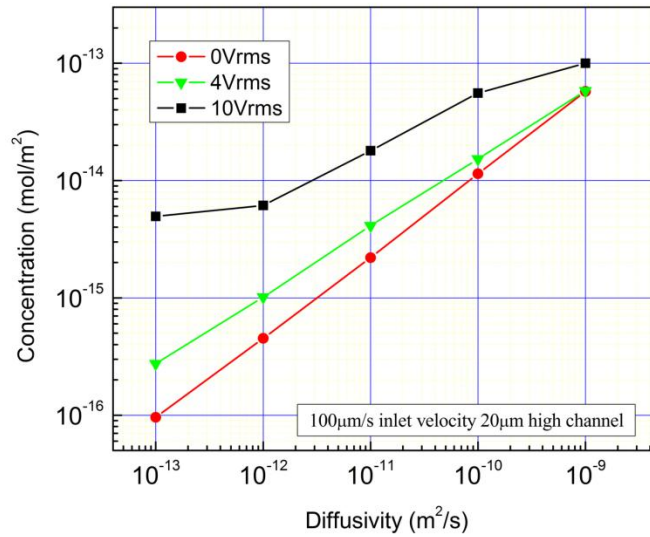
Figure 4-7. ACET concentration effect with molecular diffusivity change. Calculation assumes 100 μm/s inlet velocity and 20 μm channel height.

observed with ACET stirring, as shown in figure 4-7, with 4 Vrms and 10 Vrms, compared with flow through alone (0 Vrms). It is noticed that ACET stirring effect is most effective when diffusivity of analytes is very low, especially for large molecules such as proteins. With 10 Vrms signal at diffusivity of 10^{-13} m^2/s, improvement of concentration gain can reach 50. As diffusivity increases, stirring becomes less effective and necessary. 4 Vrms singal could not improve concentration further at diffusivity of 10^{-9} m^2/s.

4.2.5 Scaling down ACET devices

For the above discussion, sensor length is set at 5 μm, which is also the electrode gap size. What would happen if the sensor size is reduced to submicron? Is it feasible

77

to construct a preconcentrator for nanosensors by scaling down everything proportionally? The answer looks like a "yes" at first glance. Simulation was performed for which all dimensions were reduced by a factor of 10, i.e. a preconcentrator with a 0.5 μm gap between 2 μm electrodes, 0.5 μm wide sensor and 2 μm channel height. The voltage applied to electrodes thus changes from 10 Vrms to 1 Vrms in order to keep the same electric field strengths. Concentrator effect for such a preconcentration is shown in figure 4-8, which indicates no benefit from ACET mixing. A look at its velocity profiles (figure 4-9) reveals that scaling down the device size to a length scale of micron produces very different velocity profile. Even though the electric field strength remains the same, flow resistance increases by 10000 times due to a 10x smaller channel size. For the same electric field strength, ACET flow velocity as indicated by Vy is around 6 μm/s, while the corresponding velocity is ~6000 μm/s for its 10x larger counterpart (figure 4-6).

With lower channel height, ACET vortices are compressed. To improve the binding rate of nanosensors, one possible solution is to use large channel in which ACET flows can be effectively generated. Figure 4-10 shows improvement in binding rate when a larger 20 μm channel is used.

Another way to improve sensitivity of submicron sensor is to carefully choose sensor locations. Figure 4-11 shows a comparison of sensor placed close to electrode edge and sensor at the center of the electrode gap. Both sensors have 0.5 μm in width, with same applied signal and inlet velocity. It is clear that sensor close to electrode edge has better sensitivity. At electrode edge, electric field strength is stronger, leading
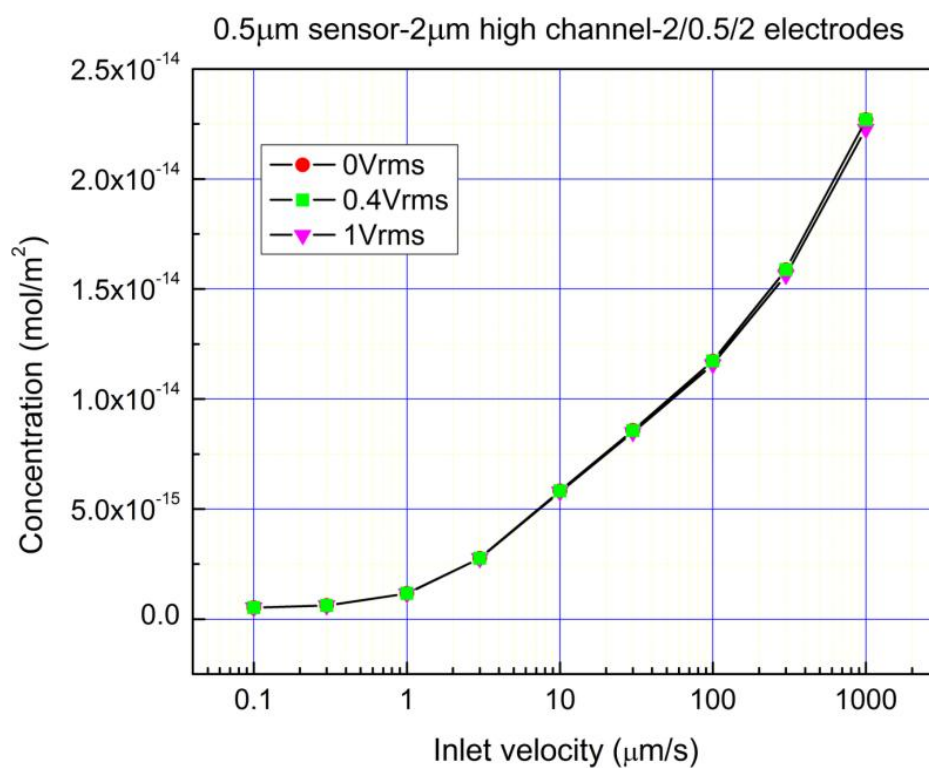
Figure 4-8. Concentration effect for a submicron sensor (0.5 μm wide) in a 2 μm high channel. No benefit from ACET stirring can be observed compared with its 10x larger micro- sized sensor.
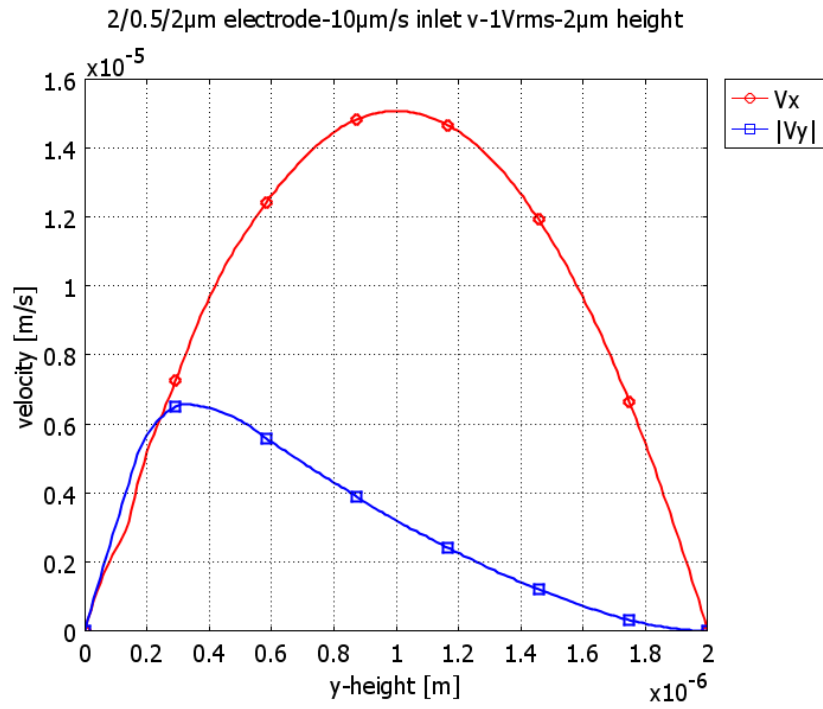
Figure 4-9. Fluid velocity distribution along the electrode centerline as a function of channel height for the scaled-down device (0.5 µm wide sensor and 2 µm channel height). Vertical velocity is shown as blue square line and horizontal velocity is shown as red circle line. Inlet velocity is 10 µm/s and voltage is 1 Vrms.
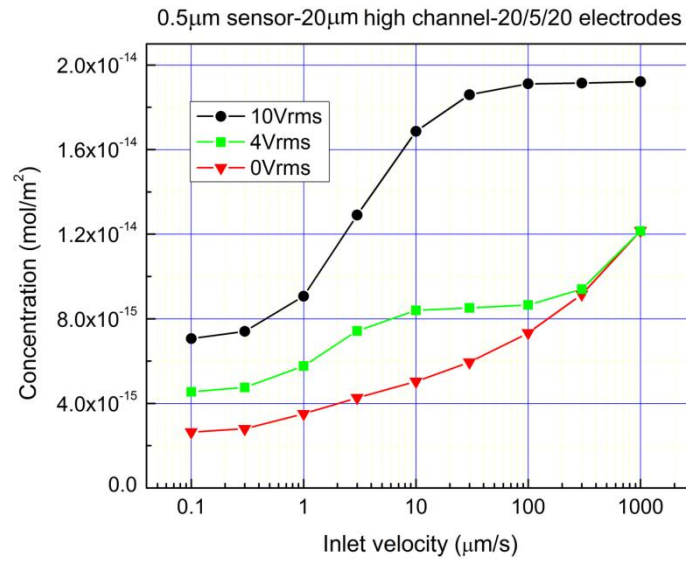
Figure 4-10. ACET concentration effect for a submicron sensor (0.5 μm wide) in a 20 μm channel.
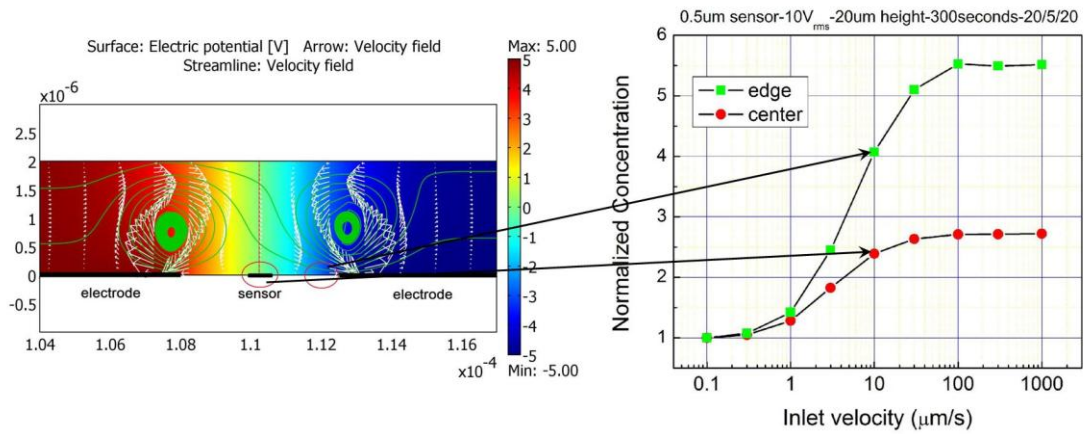
Figure 4-11. Improved sensitivity by carefully choosing sensor location. Simulation shows sensor placed close to electrode edge has better sensitivity than sensor placed at the center of the electrode gap.

to higher ACET stirring velocity. The stronger guiding forces would bring more target particles towards the sensor, improving concentration effect. The data showing at moderate inlet velocity (10 µm/s to 100 µm/s), binding rate has doubled if sensor is placed close to electrode edge.

4.3 Conclusions

This chapter presents a preconcentrator design that can achieve fast and in-situ concentration of nanoparticles for enhanced detection. Using ACET mixing, vortices can be generated locally to provide active guidance of analytes such as DNA and protein towards sensor. The configuration is simple yet effective, and it is easy to implement and integrate with the detection system.

Numerical simulation is used to study the effects of various design parameters on the binding rate at the sensor, including signal strength, flow velocity, channel height, sensor size, and molecule diffusivity. With sufficient advection from vortices generated by ACET effect, channels larger than 20 µm are more effective in trapping targets. Optimized preconcentrator design will also reduce the required flow rate so that reagent consumption can be reduced. While scaling down the device may not be viable for nano-scale sensors, it is possible to improve nanosensor binding rate by carefully choosing channel size and sensor locations.

Chapter Five: Development of AC Electrokinetic Immunoassay Lab-Chip for Accelerated Diagnosis

Immunoassay is one of the most widely used biomedical disgnostic methods due to its sensitivity, selectivity and specificity. It is based on the unique ability of an antibody to bind specifically to an antigen [1]. Conventional immunoassay test is a multistage, labor-intensive process that usually needs at least several hours to complete multiple reagents dispensing, incubations and several washing processes [2], which is not practical for on-site serodiagnosis of infectious diseases in human and wild animals. The advent of microfluidics lab-on-a-chip technology has shown promises for developing a system with portability, integration and automation, which is in great demand for on-site Point-of-Care (POC) diagnostic applications [3-5].

5.1 Immunoassay introduction

In general, immunoassay has two formats: homogeneous and heterogeneous assays. Homogeneous immunoassays take place in the solution phase while in heterogeneous immunoassays, the antibody or antigen is immobilized on a solid substrate. Heterogeneous immunoassays are popular because they are easy to design, but require extra incubation step to immobilize pathogen antigen or antibody. With the advantage of the microfluidic technology, many novel immunoassay designs based on microfluidics emerged in recent years. These systems include: diffusion-based (homogeneous) microfluidic immunoassay [6], surface/beads-immobilized

(heterogeneous) microfluidic immunoassay [7], separation-based (membrane) microfluidic immunoassay [8], and centrifugal-based (microfluidic compact disk, CD) microfluidic immunoassay [9].

In addition to binding specificity, another key feature of all immunoassays is a means to produce a measurable signal in response to a specific binding. Immunoassay detection can be classified as optical detection and non-optical detections, according to the label used. Optical detection includes: fluorescence detection (most commonly used) [10], chemiluminescence (CL) detection [11], thermal lens microscope detection [12], surface plasmon resonance (SPR) detection [13], and absorbance detection [14]. Non-optical detection includes: electrochemical detection [15], quartz crystal microbalance detection [16], etc. A comprehensive review on different types of microfluidic immunoassays and detection methods is present in [17].

To date, in most microfluidic immunoassays, reagent delivery is by pressure driven flow, and binding is by thermal diffusion. These characteristics pose the obstacles for chip integration and rapid, sensitive detection. We propose to use ACET mechanism to overcome the two obstacles. First, from the numerical study on the preconcentration in Chapter Four, ACET effect can greatly enhance the particle transport and mixing in the microfluidic devices. The vortices generated by ACET effect will break the diffusion barrier of the low diffusivity molecules toward the sensor and reduce the reaction (binding) time. Second, the ACET pumping electrodes are embedded in microchannels with no moving parts, making it easy to integrate with other functional units.

The immunoassay lab-chip designed in this research work is for detection of Johne's disease in dairy cattle. The conventional immunoassay protocol was originally developed by Dr. Eda, who specializes in the development of immunoassays for diagnosis of infectious diseases in animals and humans, from the department of Forestry, Wildlife, and Fisheries, UTK. The detailed processes and illustrations are shown in figure 5-1.

The original procedures of immunoassay are based on heterogeneous format using ELISA (enzyme-linked immunosorbent assay) techniques. As illustrated in figure 5-1, antigen is immobilized to microchannel surface, and then blocking buffer (10 mM phosphate buffered saline, pH 7.0, containing 0.05 v/v% Tween 20 and 10 v/v% SuperBlock, PIERCE Biotechnology, Rockford, IL) is used to reduce unwanted surface absorption of antibodies. After the binding of serum antibody onto immobilized antigen, 2nd antibody (fluorescent labeled) is introduced into the reaction channel. After it binds to the antigen-antibody conjugates, fluorescent image pattern will occur under proper fluorescence excitation. There is a wash process (PBST) after the introduction of both serum and 2nd antibody to flush away the unbounded excessive antibodies in the channel.

Here, all the binding and washing processes are achieved by pure diffusion in sample fluid, each step takes 30 minutes for sufficient binding and washing to achieve detectable induced fluorescence and differentiation between positive and negative serums. It is considered too long for on-site diagnostics. In order to reduce reaction time and improve sensitivity, we strive to develop an ACEK based immunoassay lab-

Original Protocol For Immunoassay

1. Load antigen into chamber, wait to dry, 2hours, 30 minutes.
2. Load buffer B, wait for 15 minutes.
3. Flush chamber with PBST, 4 times.
4. Load serum diluted in PBST (1:20), 30 minutes
5. Flush chamber with PBST, 4 times
6. Load secondary antibody diluted in PBST (1:100), 30 minutes
7. Flush chamber with PBST
8. Observe through microscope for fluorescent patterns

antigen
serum (+ or -)
2nd antibody
blocking buffer
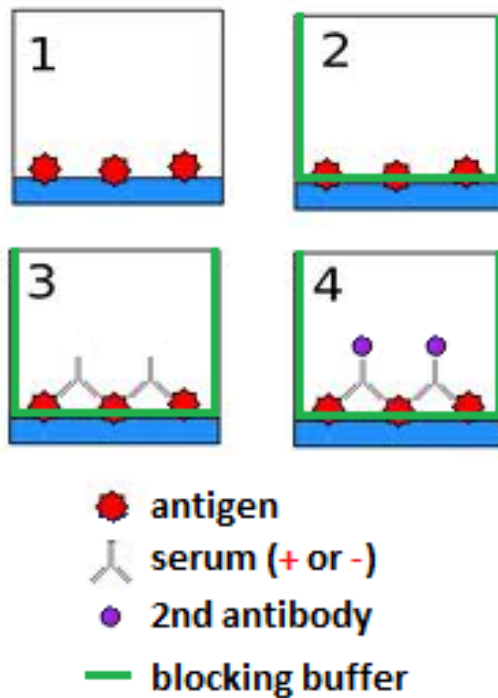
Figure 5-1. Original protocol and illustrations for immunoassay performaed in biology labs.

chip. The development of the lab-chip device and optimization of process is discussed in details in the following.

5.2 Reagents preparations

Reagents: In this study, we used the causative agent and serum samples of Johne's disease for experiment with ACET-based immunoassay system. Johne's disease is an economically important infectious disease in dairy industry and is caused by infection of cattle with bacterial pathogen, Mycobacterium avium subsp. paratuberculosis (MAP).

Pathogen-specific antigen: MAP was obtained from the USDA (Ames, IA) and was cultured in Middlebrook 7H9 medium (Becton Dickinson Microbiology Systems, Franklin Lakes, NJ) with 10% OADC (oleic acid-albumin-dextrose-NaCl) (Becton Dickinson Microbiology Systems, Franklin Lakes, NJ). The medium was supplemented with 2 μg/ml of Mycobactin J (Allied Monitor, Fayette, MO). The cultures were maintained at 37°C without shaking until they reached an optical density of approximately 0.7 at 600 nm. MAP was harvested from the liquid culture at stationary phase and centrifuged at $2,600 \times g$ for 10 minutes; the pellet was resuspended in 80 % ethanol, agitated by vortex at room temperature for 2 minutes, and centrifuged at $10,621 \times g$ for 10 minutes. The supernatant was collected, diluted in 100 % ethanol (1:80) and used as antigen for immunoassay.

Serum samples: Bovine serum samples were obtained from the National Animal Disease Center, USDA, Ames, IA. The positive serum was obtained from a dairy cow

(breed, Holstein; age, 2.8 years old; gender, female) that was tested positive for Johne's disease by bacterial culture method and enzyme-linked immunosorbent assay. The negative sample was obtained from a dairy cow (breed, Holstein; age, 2.4 years old; gender, female) that was tested negative for Johne's disease by the two procedures.

Secondary antibody: The secondary antibody, goat anti-bovine IgG (heavy plus light chain) labeled with the DyLight 488, was obtained from Jackson ImmunoResearch Laboratories (West Grove, PA). Before using in the immunoassay, the secondary antibody was diluted in PBST (10 mM phosphate buffered saline, pH 7.0, containing 0.05 v/v% Tween 20).

5.3 Immunoassay chip design and fabrication

The immunoassay microfluidic chip consists of Polydimethylsiloxane (PDMS) channels sealed over a silicon wafer. The silicon wafer forms the channel bottom and the layout of the microchannel is shown in figure 5-2. On the left side, three reservoirs are designed to house serum, secondary antibody and wash solution, respectively. For the final format, antigen will be coated on the bottom of the reaction channel, and all other surface will be blocked with buffer B. The three dispensing channels with embedded ACET pumping electrodes serve as pumps and passive valves for flow control. When electrodes in dispensing channel are excited by ac signal, ACET electrodes will produce pumping action to deliver reagents from corresponding reservoir into the reaction channel. When ac signal is off, hydraulic pressure will prevent cross contamination of solutions from one reservoir to another. Each of the
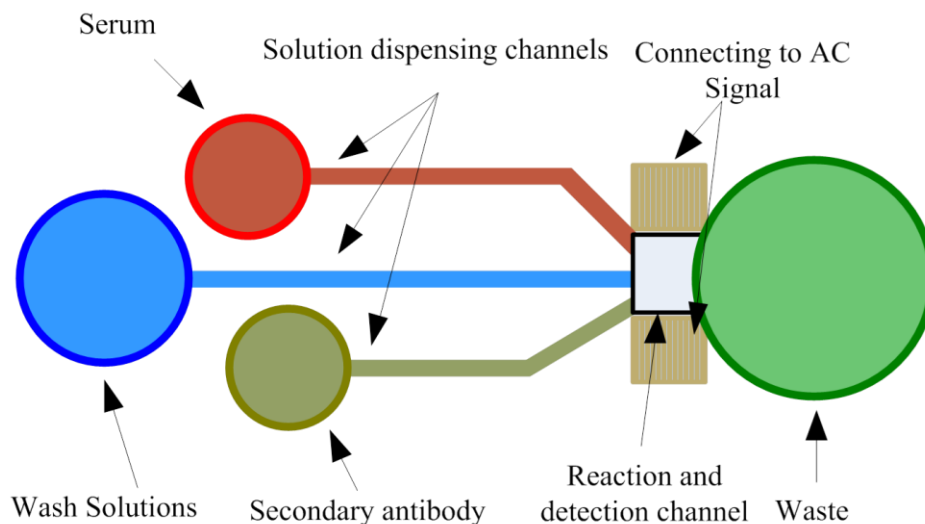
Figure 5-2. Layout of microfluidic channel consisting of three sample reservoirs, solution dispensing channels, reaction and detection chamber, and waste reservoir.

dispensing channels can be separately controlled for sequential loading of reagent from each reservoir. There are also ACET electrodes in the reaction chamber that generate vortices for accelerated binding.

Both dispensing channels and reaction chamber are covered with interdigitated planar electrode arrays to perform pumping and mixing functions. The mask for electrode patterns was drawn using CAD software and was fabricated using E-beam lithography. And the electrodes were fabricated on SiO_2 covered silicon substrate using standard lift-off process (shown in figure 5-3) in the cleanroom of CNMS (Center for Nanophase Materials Sciences), Oak Ridge National Laboratory (ORNL).

The detailed recipe for lift-off process performed at ORNL is listed below:

1) Coat LOR1A (lift-off photoresist) at 2 krpm for 45 seconds.

2) Prebake of LOR1A for 10 minutes at 190°C.

89

3) Coat SPR 955 0.7 photoresist (positive tone) at 2 krpm for 45 seconds, soft bake for 90 seconds at 90°C.

4) Exposure for 7 seconds.

5) Post-exposure bake for 90 seconds at 115°C.

6) Develop in CD-26-TMAA (photoresist developer) for 67 seconds.

7) 30 seconds descum in O_2 plasma (to remove residues from substrate).

8) Deposit metals by evaporation, 5 nm Cr (for adhesion), 60 nm Pt (as electrodes).

9) Soak wafers in CD-26 for LOR1A removal.
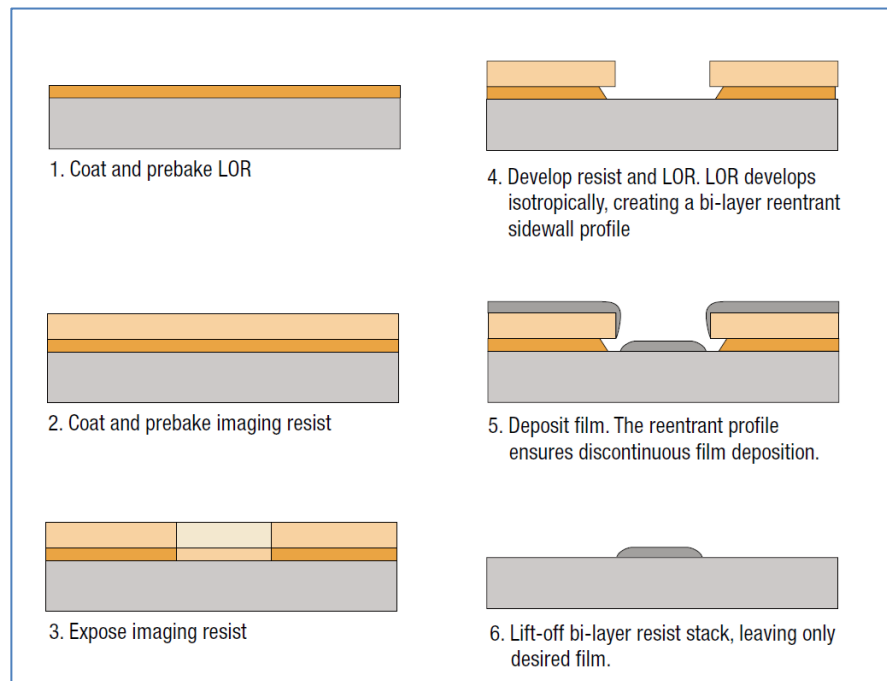
Figure 5-3. Schematics of standard lift-off process for electrode fabrication.

The microchannels are fabricated with PDMS by soft molding (shown in figure 5-4). A layer of photoresist is patterned and developed on silicon or glass surface, and serves as a master mold. The thickness of the photoresist will be the height of the microchannel. The PDMS (SYLGARD® 184 SILICONE ELASTOMER KIT, Dow Corning Corporation), mixture of silicone base and curing agent (10:1 in weight), is then poured over the master and cured at room temperature or heated plate. After curing, PDMS is removed from master. The cured PMDS layer is elastic and transparent, which is ideal for microfluidic channels.

The fabricated electrodes on silicon wafers and PDMS microchannels are shown in figure 5-5.
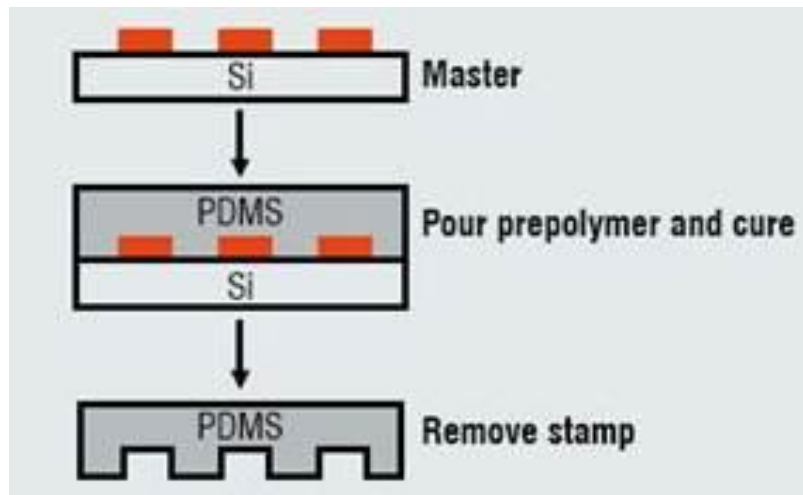
Figure 5-4. Schematics of PDMS soft molding for microchannel fabrication.
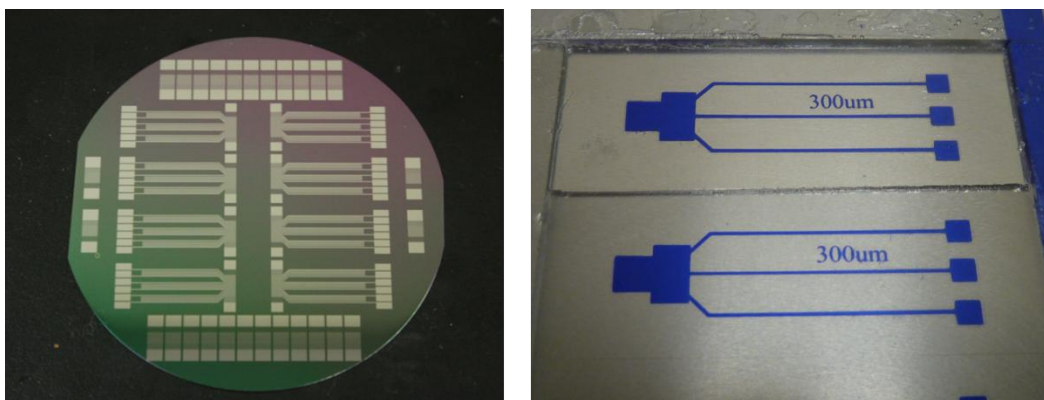
Figure 5-5. Left: fabricated electrode patterns on 4 inch silicon wafer. Right: PDMS layer as microchannels.

5.4 Lab-on-a-chip immunoassay compatibility issues

A compatibility test for immunoassay at 0.2x PBS was conducted in Dr. Eda's lab using original immunoassay protocol. The test results (shown in figure 5-6) proved that 0.2x PBS is compatible with antigen-antibody binding, blocking and wash procedure.

There is concern that biomolecules from the assay will adhere to the ACET electrode surface and the adhesion layer could pose high impedance between the ACET electrode and the sample solution to prevent effective application of AC voltages. Therefore, the impedance of the device was measured with Agilent Impedance Analyzer (Agilent 4294A, USA), before and after blocking buffer. Figure 5-7 shows a frequency sweep of the system impedance, with magnitude and phase information in separate plots. It is clear that blocking process did not change much of the system impedance, especially in active ACET frequency region ranging from 100 kHz to 1
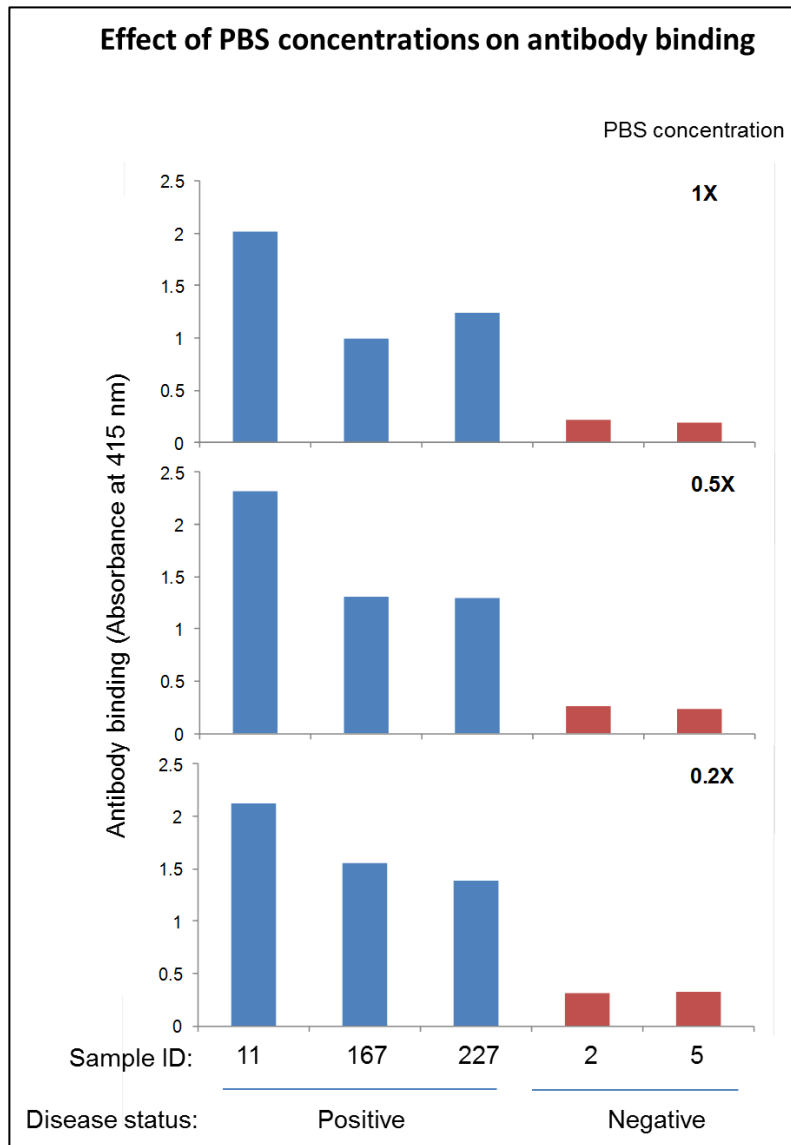
Figure 5-6. Effect of PBS concentration on antibody binding (tests performed at Dr. Eda's lab by Ashutosh). Disease status can be distinguished at 1x PBS, 0.5x PBS and 0.2x PBS.
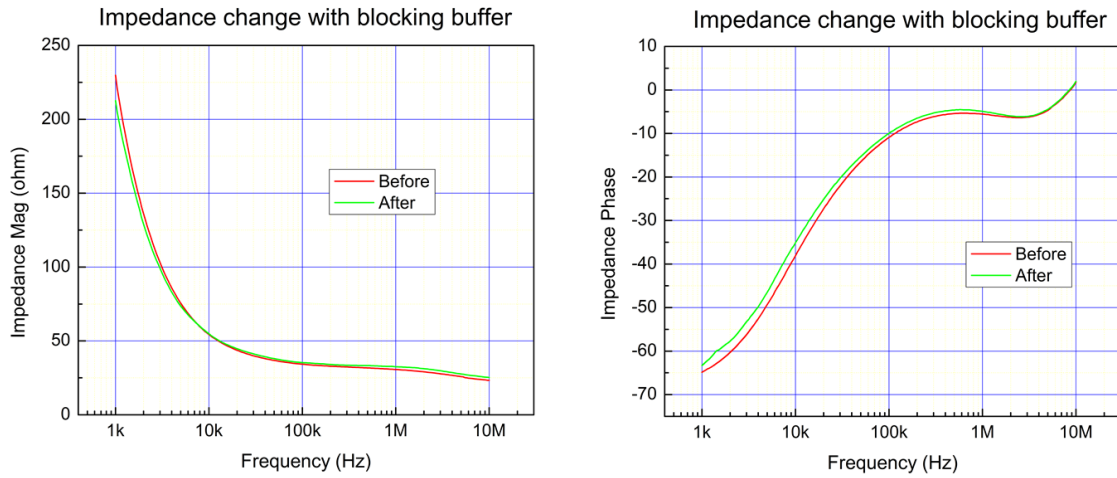
Figure 5-7. Impedance measurement before and after blocking buffer with frequency sweep. Left plot: impedance magnitude. Right plot: impedance phase angle. Blocking process has very limited influence on ACET effect.

MHz. From the discussion of ACET effect in chapter three, ACET effect is based on Joule heating and temperature gradient in bulk fluid, and the coating on electrode surface would only affect the double layer performance at low frequency (usually below 10 kHz). So the influence of coating blocking layer on channel surface can be neglected for ACET effect.

5.5 Proof of concept-ACEK enhanced immunoassay diagnosis

The proof of concept for ACEK enhanced immunoassay diagnosis lies in two parts: ACEK induced micro-pumping and ACEK enhanced concentration.

5.5.1 ACEK induced pumping motion

In order to control the fluid motion in the microchannel and replace pressure driven syringe pumps with electrokinetic pumps in the lab-on-a-chip design, ACEK induced pumping effect is investigated. Two mechanisms of ACEK can generating fluid motion, know as AC electroosmosis (ACEO) and AC electrothermal (ACET) effect. As has been discussed in detail in chapter three, ACEO is effective only for low ionic solutions. Highly conductive biological solutions would compress the thickness of the electric double layer, supressing the ACEO effect. On the other hand, ACET originates from the Joule heating in the solution, depending on thermal graident distribution. It is compatible with conductive biofluids and sample molecules.

Most of the bio-samples have to be preserved in a liquid environment with high salt content such as buffered saline (PBS) solution. The electrical conductivity of the PBS solutions is usually over 1 S/m. In the current project, ACET effect is used to safely pump the sample solution of up to 0.2x diluted PBS solution, as shown in figure 5-8 (video is available at presentation). Asymmetric electrode arrays were used in the pumping test, with 5 μm narrow electrode, 5 μm gap, 25 μm wide electrode, and 25 μm gap, forming 5/5/25/25 configuration. 100 kHz, 16.8 Vpp ac signal was applied to electrodes. Fluorescence labeled latex particles (diameter 1 μm) were added as tracers to indicate flow motion. The pumping direction is from narrow electrode to wide electrode, as the arrow shows in the figure. In the pumping test, concentration above 0.2x PBS might lead to electrical-chemical reaction and cause damage to electrodes.
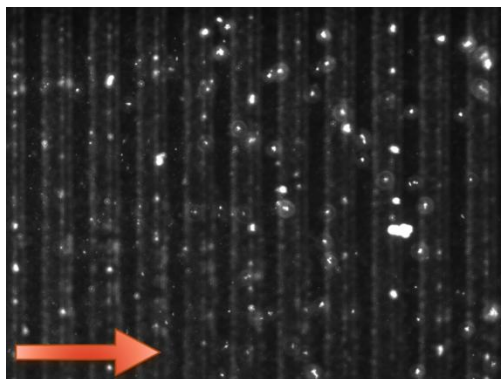
Figure 5-8. ACET pumping of biofluids with condutitivty of 0.2x PBS solution (measured at 0.34 S/m). 5/5/25/25 μm electrode patterns are used. 100 kHz, 16.8 Vpp ac signal applies to electrodes. The arrow indicates the flow direction.

5.5.2 ACEK enhanced concentration

Conventionally it takes hours or even days to complete the whole immunoassay process of sample incubation, loading, and multiple washing steps. The binding of antigen and antibody depend soly on diffusion. Large molecules such as DNAs and proteins have very low diffusivity, and this bottle neck has prevented time efficienct clinical diagnostics.

The setup for ACET enhanced immunoassay test is shown in figure 5-9. The microchannel has a height of 40 μm and a width of 800 μm. Interdigitated electrodes were covered by microchannel, with two reservoirs for sample injection. Electrodes were connected to signal generator through conducting tape.

The following is the modified protocol for the microfluidic immunoassay lab-chip. First, antigen (2 μL in volume) is loaded into the reservoir using a pipette. After incubation at room temperature for 15 minutes, surface will be uniformly coated
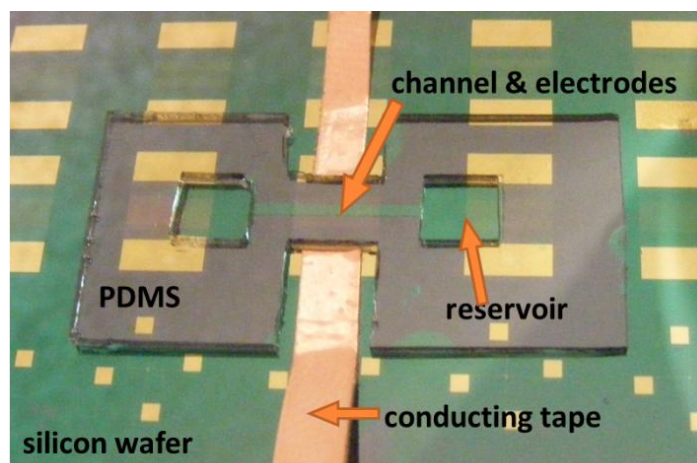
Figure 5-9. The microfluidic device used for preliminary immunoassay tests. Electrodes were fabricated on silicon wafer, and covered by PDMS channel. Conducting tape connected electrodes to signal generator.

with antigen. The blocking buffer solution is then loaded into the channel. The purpose of this step is to avoid non-specific binding of antibody to channel surface. Washing with PBST is followed after 15 minutes blocking process. The proceeding steps are preparing the LOAC for specific test. Actual on-site serum diagnosis starts with the injection of serum sample, i.e. the next step. At step 4, the serum (10-15 μL) with either positive or negative antibody is loaded to the channel. AC signal is applied to the electrodes for 1-10 minutes. After flushing with PBST solution, the secondary antibody (10-15 μL) is loaded. AC signal is turned on for 1-5 minutes. After washing step, fluorescent patterns are ready to be viewed under microscope or through optical detection, and further image and data processing can be performed.

Figure 5-10 shows a simulated illustration of ACET enhanced immunoassay process. Electrodes excited by ac signal would generate vortices by ACET effect,

which can bend flow streams and guide analytes towards reaction sites. Experimental results from the immunoassay tests have validated this hypothesis.

A numerical simulation was performed to study the distribution of the binding under ACET effect. The model was similar to models in chapter four, except that the sensor covers the whole bottom channel and pumping motion was solely contributed by ACET effect. The ac signal and geometry parameters used in simulation were the same as that we performed the experimental tests. The simulation result is shown in figure 5-11(a). 5/10/15/30 μm electrode arrays are used and channel height is 40 μm. 10 Vrms, 100 kHz ac signal applies to fluid with conductivity of 0.36 S/m (0.2x PBS has 0.34 S/m conductivity). The distribution of binding after 300 seconds is shown in figure 5-11(b). It agrees with experimental results that concentration on the electrode
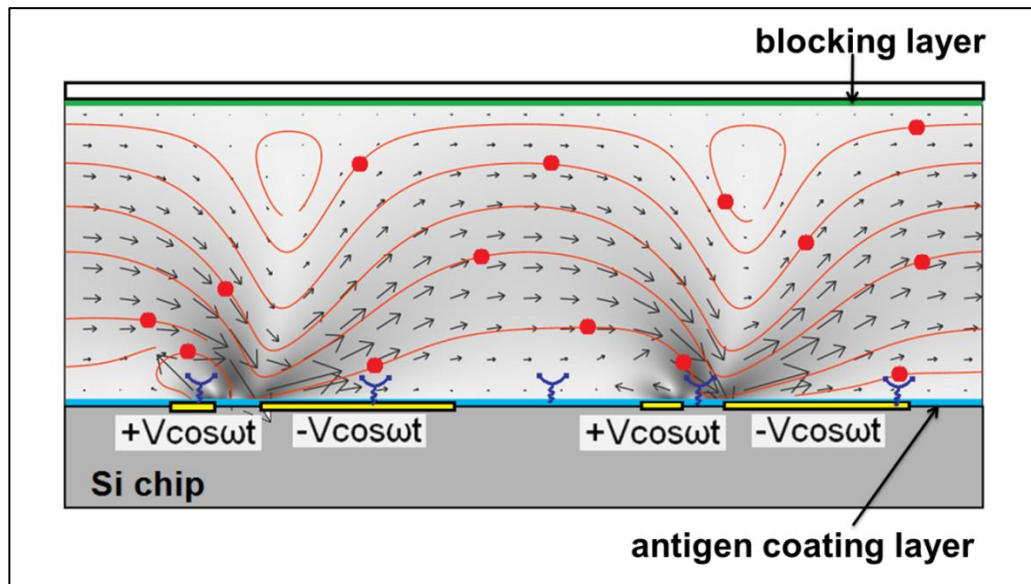
Figure 5-10. Simulated on-chip pumping and mixing by ACET effect with immunoassay process.
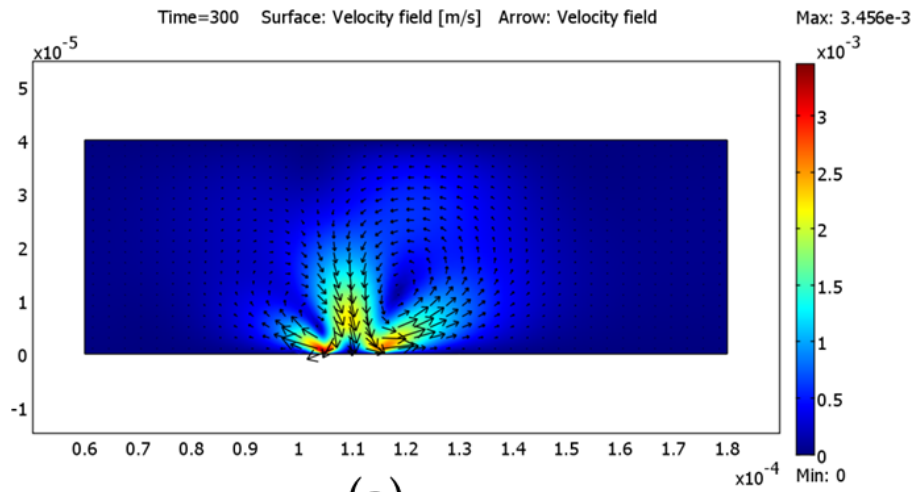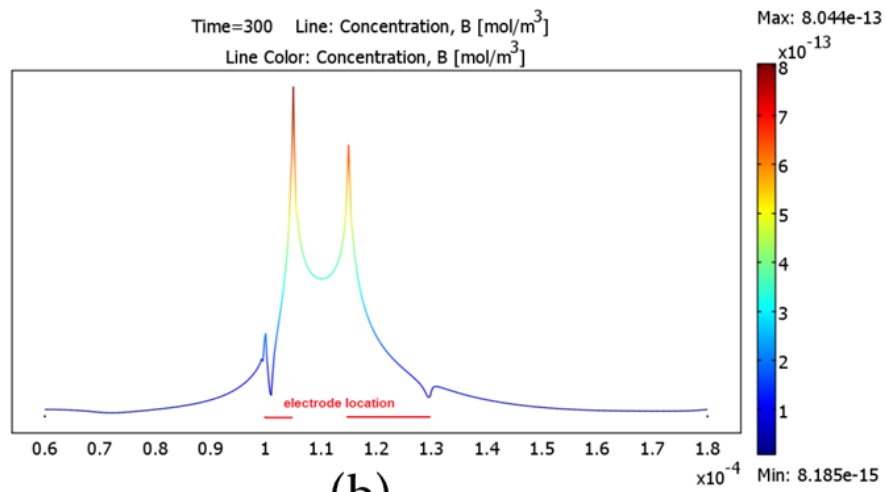
Figure 5-11. Numerical simulation of ACET enhanced concentration effect after 300 seconds. (a) Both pseudo color and arrows indicate velocity distribution. Two vortices were generated above the electrodes. (b) Concentration distribution along the bottom channel surface. Electrode surface has higher concentration, and peak concentration occurs on the electrode edges.

surface is higher than electrode gap, and peak concentration occurs at electrode edges, where electric field is strongest and ACET effect is most prominent.

Preliminary study was conducted to investigate the feasibility of lab-chip immunoassay of TB antigen, in which reagents were pumped through the reaction channel by ACET effect. Figure 5-12 shows one of the experimental results using both positive and negative serum antibodies. The bright line patterns in the figure are bounded 2nd antibody with antigen-antibody conjugates over an array of 10 μm wide electrodes (10/5/10/20 μm electrode pattern). With ACEK pumping and mixing, shorter incubation time is needed, and 3-10 minutes were used in the experiments to sufficiently differentiate the positive and negative serums, which is much faster than conventional 30 minutes incubations.

The fluorescent pattern was observed through the fluorescence illumination system (X-Cite 120, Lumen Dynamics Group, Canada) with Nikon B-2A filter cube (excitation 450-490 nm). The CCD camera (Photometrics CoolSNAP ES, Roper Scientific, Germany) attached to the Nikon microscope (Nikon Eclipse LV100, Japan) took high quality 12 bit depth grey-scale images, and 3D histogram plots based on intensity were generated by Image Pro software (Media Cybernetics, MD, USA). Intensity of each pixel of the image (696x520 pixels) was calculated and averaged. The quantification showed that negative and positive sample had values of 402.4 and 1231.9 (based on $2^{12}=4096$ grey scale), respectively. Positive and negative samples showed distinctive intensity values, and the difference is over three times.
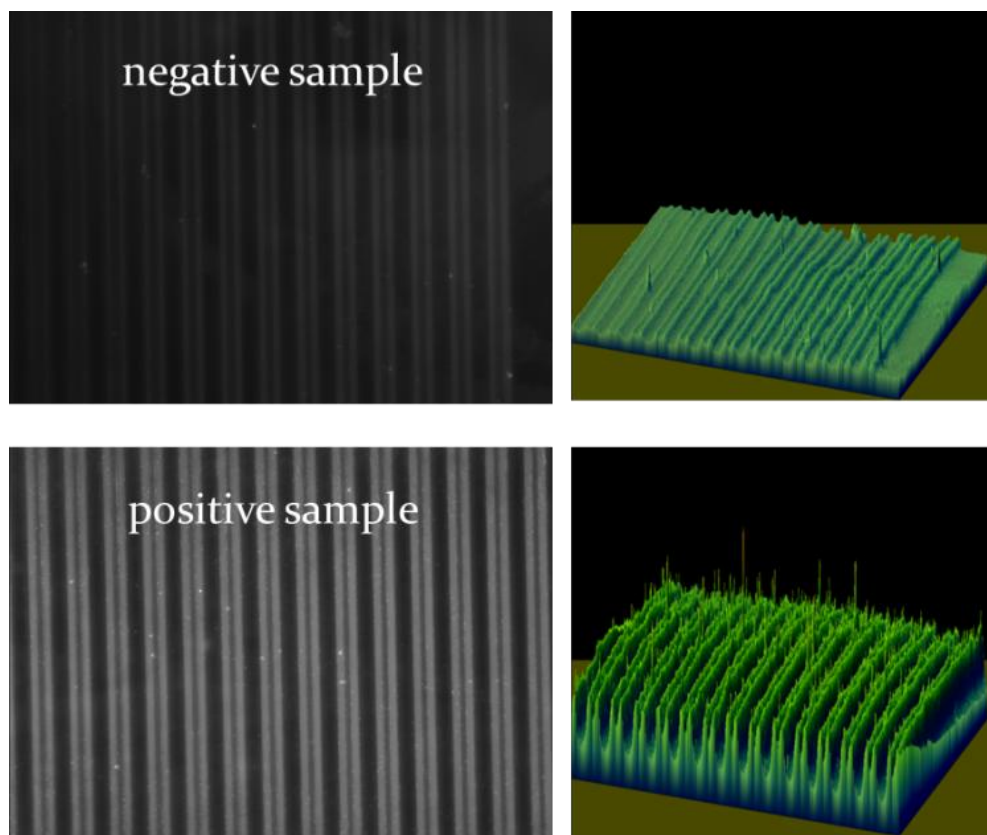
Figure 5-12. Left: fluorescence images over the microelectrode array 5 minutes after pumping through 2nd antibodies with ACET effect. Right: 3D surface histogram plots indicating the relative intensity difference between two samples. Quantification of image intensity showed that the positive sample was 3 times brighter than the negative one. Images were taken under 20x objective lens, with ac signal 100 kHz and 15 Vpp.

A control experiment was conducted to show proof of the benefit of ACEK pumping over pressure driven pumping. The control test followed the same procedure, except that no ac signal applied to primary and secondary antibodies. Fluid flows past the reaction channel by hydrolic pressure between the two reservoirs. The images shown in figure 5-13 were taken at 5 minutes after applying secondary antibody. 3D histogram plots were present and averaged image intensity was quantified. It is clear that with applied ac signal, concentration on the sensor was much higher than control counterpart. Higher light intensity was observed at the electrode edges. This pattern agreed with the theoretical prediction and numerical simulation. Because electric fields were stronger at the electrode edges, so higher flow velocities were expected to occur at the region, and consequently more biomolecules were carried through those regions by microflows and hence higher chances for antibodies to bind to the antigens. Average image intensity had increased by 70%. Under the same condition, positive and negative sample can also be distinguished.

This study shows that the benefit of ACET effect is two-fold, pumping of conductive fluids through the reaction channel and enhancing concentration binding on the sensor by generating mixing vortices.

5.6 Optimization of immunoassay procedure and lab-chip design

The preliminary results have proved that ACET effect would benefit in both pumping of biofluids and enhancing of immunoassay reactions. However, the operation conditions with ac signals were not optimized in preliminary tests. An in-depth study

positive serum signal   negative serum signal   positive serum control

avg intensity=1127.9   avg intensity=990.8   avg intensity=698.4
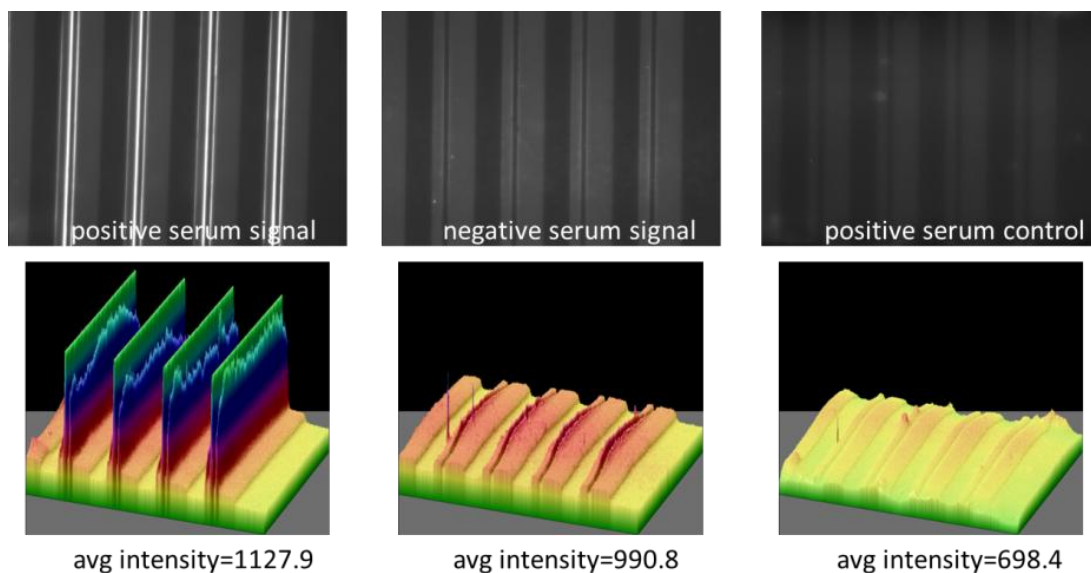
Figure 5-13. Comparison of concentration effect with and without ac signal, showing benefit of ACEK effect over pressure driven pumping. Images were taken at 5 minutes after applying secondary antibody. Concentration with ac signal showed higher intensity than control test. And positive and negative sample can be distinguished. 20/10/50/50 μm electrodes were used and 100 kHz, 16 Vpp ac signal was applied.

on experimental parameters is important to develop a comprehensive understanding of effects of ACEK flow on the biomolecule transport (in-situ concentration) and their impact on electronic biosensing mechanism and performance.

5.6.1 Optimization on ac signal frequency

In the immunoassay test, ACET effect is employed to speed up the binding of antigen and antibody. AC signal frequency would have an impact on the ACET pumping and mixing effect. An impedance plot shown in figure 5-14 reveals the fact that best frequency range for ACET effect lies between 100 kHz and 500 kHz. Within this frequency range, impedance phase angle is small, close to resistive nature, and the voltage applied to system would mostly drop in fluid bulk, favoring Joule heating and maximizing temperature gradient for ACET effect. To find the best frequency within this range to performance immunoassay tests, however, another important factor known as dielectrophoresis (DEP) needs to be taken into account. DEP (detailed theory in chapter 3.1.3) is a phenomenon in which an electric force is exerted on a dielectric particle when it is subjected to a non-uniform electric field. The strength and direction of the DEP force depend strongly on the medium and particle's electrical properties, on the particle's shape and size, as well as on the frequency of the electric field. Particle can experience either positive DEP or negative DEP depending on the AC frequency. For positive DEP, particles will be attracted towards high field regions such as electrode edges. For negative DEP, particles will be repelled from high field regions. Although primary and secondary antibodies are of nanometer size, they still have DEP
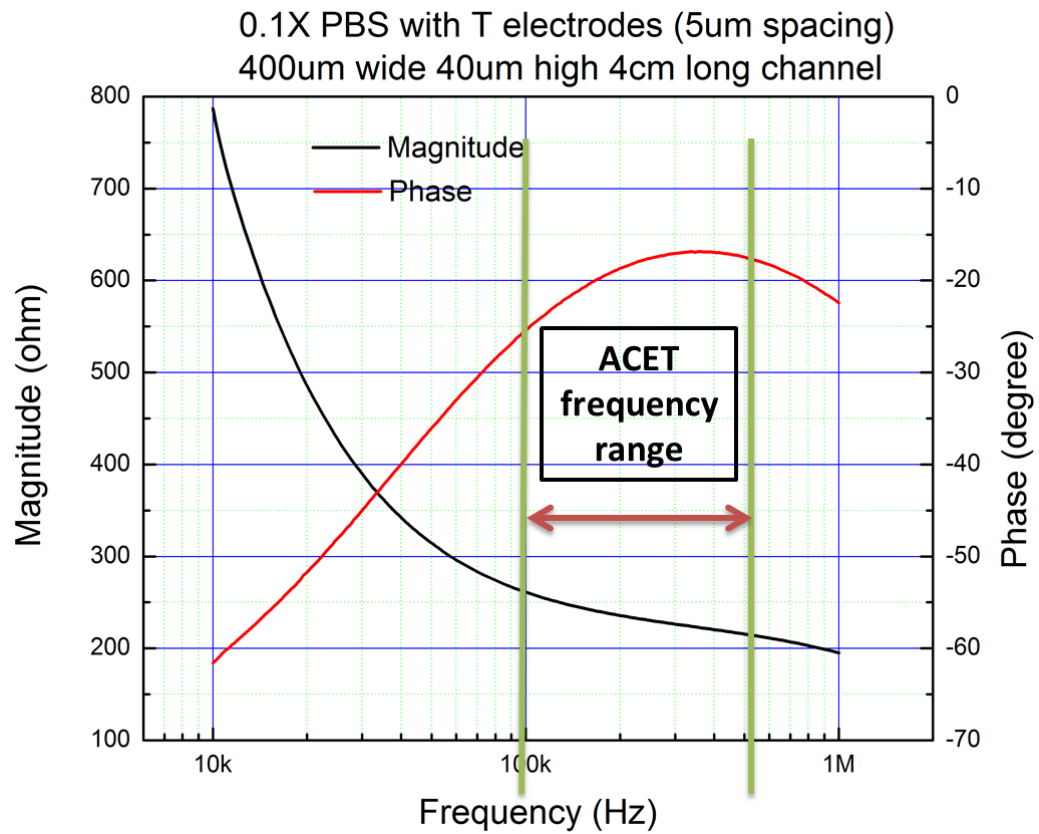
Figure 5-14. Typical impedance measurement of immunoassay lab-chip. Left scale shows impedance magnitude, right scale shows phase angle. Best frequency for ACET ranges from around 100 kHz to 500 kHz.

response to ac signal and will affect the binding process. One concern is the DEP response of the 2nd antibodies. When 2nd antibodies experience positive DEP, they are trapped to high electric field region, causing non-uniform intensity distribution and non-specific binding to electrode surface without antigen or serum antibody. The non-specific binding would add noise to the detection.

In order to obtain the DEP frequency response of 2nd antibody, a special electrode pattern was designed and fabricated, as shown in figure 5-15(a). The orthogonal electrodes, with 5 μm width and 5 μm gap between electrodes, are used to test DEP response of sub-micron particles. It has relative sharp electrode tip compared with interdigitated electrodes, and with the same applied voltage, the electric field gradient around the electrode tip is much higher. According to DEP theory, DEP force (Equation (22) in chapter three) scales with square of electric field gradient, and T electrode design can maximize DEP force around electrode tips. Figure 5-15(b) shows a simulation result of positive DEP force distribution around the electrode tip. The closer the particle is to the electrode tip, the large the DEP force it will experience. In the experiment, a PDMS channel similar to preliminary test was sealed over the T electrode arrays. Then only the 2nd antibody solution was loaded into the channel. 2nd antibody is diluted as 1:100 v/v% in 0.1x PBST solutions. The use of 0.1x PBS has been tested to be compatible with immunoassay process, and it is easier to apply ac signal to 0.1x PBS than 0.2x PBS because 0.1x PBS has higher impedance (larger than 50 ohm, standard output resistance for signal generator). Different frequencies were applied in the range of 100 kHz through 500 kHz, and image intensity was recorded for
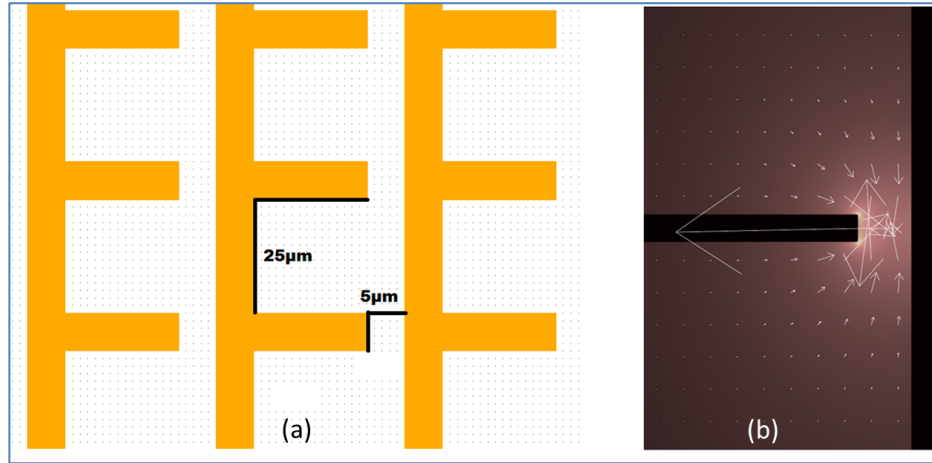
Figure 5-15. (a) Orthogonal (T) electrode configuration. (b) Simulation of positive DEP force around electrode tip (Arrows and pseudo color show the relative scale of DEP velocity).

each frequency after 3 minutes with ac signal. Average intensity for each frequency was calculated based on electrode tip areas (16x16 pixels). 12 bit grey scale image intensity ranges from 0 to 4095 (2^{12}).

The test result is shown in figure 5-16. The test covered 6 typical frequencies at 100 kHz, 200 kHz, 250 kHz, 300 kHz, 350 kHz, and 400 kHz, respectively. DEP response has changed quite distinctively through all these frequencies. At 100 kHz ac signal, it is obvious that 2nd antibody experienced strong positive DEP. The electrode tip trapped large amount particles, indicated by bright fluorescent patterns. When the frequency increased to 200 kHz, intensity on electrode tip decreased, but there were still signs of positive DEP. From 250 kHz, fluorescent patterns were different from 100 kHz or 200 kHz. There was no sign of particle trapped specifically to electrode tips,

indicating frequency has entered negative DEP range. It is a transition from positive DEP to negative DEP, and cross-over frequency lies between 200 kHz and 300 kHz.

Although 100 kHz produces almost twice as much of fluorescence intensity as 300 kHz, it comes from positive DEP trapping and will only lead to more severe non-specific binding, leading to false positive diagnosis. This study can also explain the bright lines occurring at electrodes edges at preliminary results were contributed a lot by positive DEP.

So the optimized frequency to reduce positive DEP of 2nd antibody is to work at around 300±50 kHz. It also gives more uniform intensity distribution at 300 kHz, suitable for optical detection units other than microscope.

Particle DEP property will not change with electrode configurations, so the optimized frequency applies to interdigitaged electrodes as well. Figure 5-17 shows a typical immunoassay test result. Interdigitated electrodes 5/5/25/25 were used, and test results at 100 kHz and 300 kHz were recorded (after 5 minutes), with positive and negative serum samples, respectively. The dilution of 2nd antibody was reduced to 1:500, which will be discussed in the next section. With the same test conditions, the differences between positive and negative serum reached 572.9 for 100 kHz and 570.1 for 300 kHz signals. At both frequencies, disease status can be easily distinguished. At 100 kHz there were bright lines along the narrow electrodes, showing combined positive DEP effect and converging ACET flowing enhanced trapping. At 300 kHz, non-specific binding of 2nd antibody has been greatly reduced and there was a more uniform fluorescent pattern.

	100kHz	200kHz	250kHz	300kHz	350kHz	400kHz
Intensity	1362.5	783.0	665.1	691.5	701.1	742.2
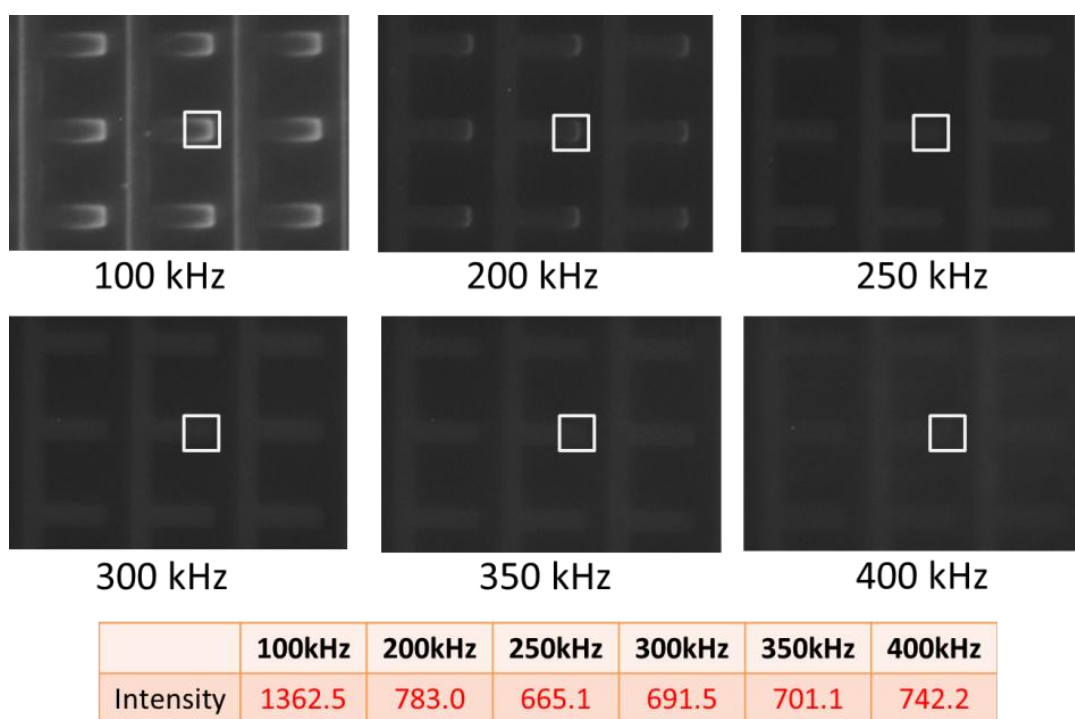
Figure 5-16. DEP frequency response for 2nd antibody (1:100 diluted in PBST). Average intensity is based on electrode tip area (16x16 pixels) with 12 bit grey scale images. Optimized frequency to reduce positive DEP is around 300±50 kHz.
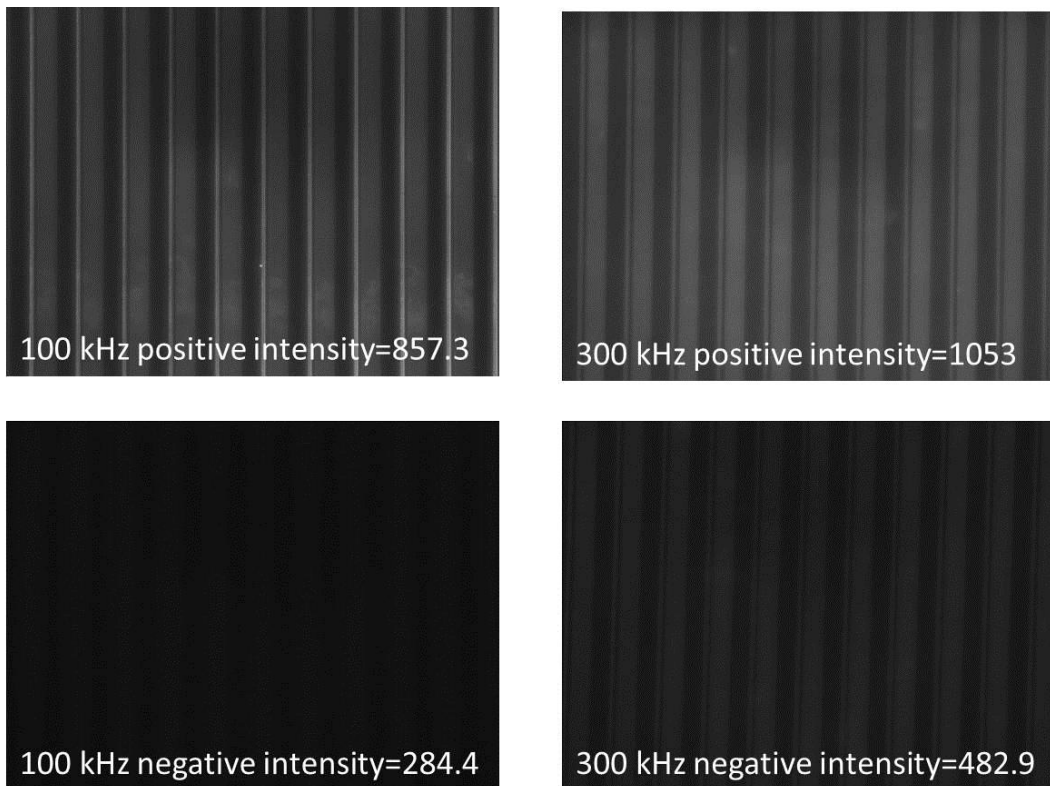
Figure 5-17. One set of immunoassay tests at both 100 kHz and 300 kHz with positive and negative serums. Both frequencies can distinguish disease status, but 300 kHz gives a more uniform intensity pattern.

5.6.2 Optimization of immunoassay procedure

In the ACET enhanced immunoassay tests, there were unstable results due to unoptimized incubation procedure or sample concentration. Some of the results are shown in figure 5-18. Time sequence of fluorescent intensity change was obtained from monitoring with CCD camera connected with microscope. Images were taken every 5 or 10 seconds, and intensity data was extracted and plot to the curves. The common problems were that intensity for positive and negative serum had very little difference (figure 5-18(a)), or negative having higher intensity (figure 5-18(b)). In figure 5-18(c) and (d), though disease status can be distinguished from intensity data after 3 or 5 minutes, the difference was so small that in practical performance, it could lead to false diagnosis. Also, the four curves in figure 5-18 indicated that for the first 20 seconds, intensity increased sharply with time, and then the slope went down. This indicated that one of the biomolecules (antigen, serum, or 2nd antibody) was depleted quickly and caused saturation in the binding process.

The antigen concentration used in test is 0.1 mg/mL, with molecular weight of 1000 and dilution of 1:20 (in 100 % ethanol), the final concentration for immunoassay is calculated as 5 μM (μmol/L). The serum prepared for immunoassay is 1 mg/mL at dilution of 1:20 in PBST. With a molecular weight of 150000 (much larger than antigen molecules), the molar concentration of the primary antibody in the channel is calculated to be 333 nM. Assuming a typical binding ratio of 1000:1, the effective concentration of the binding sites for the 2nd antibody is on the order of 333 pM. 2nd antibody has same concentration as serum antibody before dilution (1 mg/mL with

111

Unoptimized Results
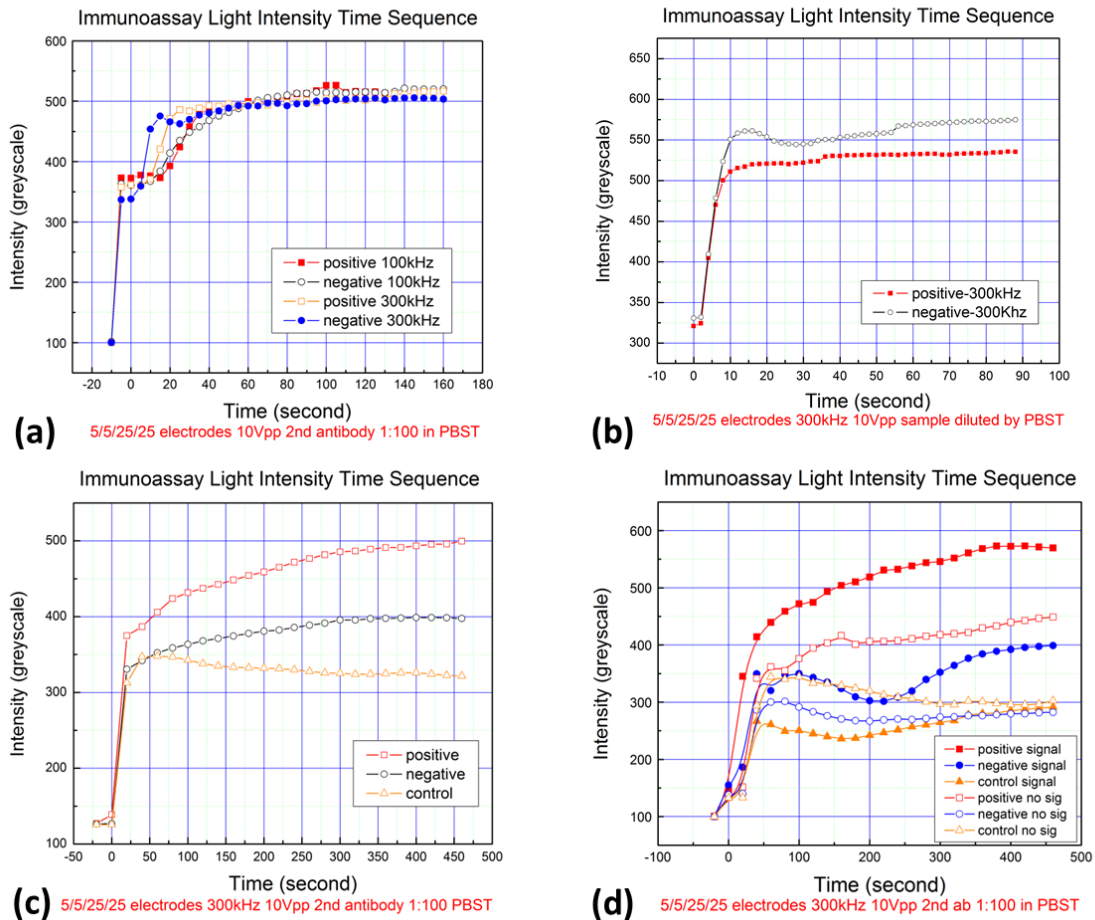
Figure 5-18. Several results from unoptimized experimental conditions.

molecular weight 150000). With dilution 1:100 in PBST, final concentration converts to 66.7 nM. A calculation of sample concentration revealed that with original concentration of sample solution, non-specific binding of 2nd antibody could be high and could add a lot of noise to the final intensity.

In the ACET enhanced immunoassay tests, microchannel has volume of 0.32 µL (40 µm high, 800 µm wide, and 10000 µm long). And the amount of antigen used in test is 1 µL, the amount of serum is 10 µL, and the amount of 2nd antibody is 10 µL. So the total amount of sample applied to channel are: antigen 5 picomole (10^{-12} of a mole), effective serum 3.33 femtomole (10^{-15} of a mole), 2nd antibody 0.67 picomole. Considering not all antigens will be immobilized to channel surface and effective serum binding as 1000:1, the calculated sample concentration indicated that the serum concentration is the limiting factor in the binding process, and it depletes faster than the other two. As there are more 2nd antibody in the solution compared with serum antibodies (0.67 picomole vs. 0.00333 picomole), excessive 2nd antibody would bind to antigen and electrode surface without serum. This could lead to excessive non-specific binding, causing positive and negative samples having similar fluorescent intensity.

In order to reduce unwanted binding by 2nd antibody and further differentiate positive and negative samples, concentration of sample solutions as well as the chip preparation procedure should be adjusted. The considerations and changes are listed below:

I. Chip preparation

113

(a) Increase antigen incubation time to ensure the immobilization of antigen onto the channel bottom (from originally 30-60 minutes to several hours or longer).

(b) Increase blocking incubation time for better surface blocking (from originally 15 minutes to several hours).

II. Sample concentration

(c) Dilute the serum and 2nd antibodies with blocking buffer instead of PBST wash fluid (adding blocking power when stirring with ac signal).

(d) Reduce 2nd antibody concentration (from 1:100 in PBST to 1:500 or higher in blocking buffer, reduce non-specific binding and cost).

With the improved preparation procedure and adjusted sample concentration, the times were adjusted to 18 hours for antigen, 2-3 hours for blocking. Serum and 2nd antibody were diluted in blocking solution at 1:20 and 1:500, respectively. The new results are shown in figure 5-19. Immunoassay tests were performed at 100 kHz and 300 kHz. Background intensity was subtracted so all curves started from 0 intensity at time 0. The timing started when the 2nd antibody sample was introduced to the reservoir. Both plots (a) and (b) showed a large difference between positive and negative of around 560 (based on 0-4095 grey scale) in intensity (also see figure 5-17 for intensity pattern) after 300 seconds, and the differences reached 6x and 4x, respectively. In figure 5-19(a), two control test results were included, one was positive serum with no ac signal simulating the pressure driven flow, and the other with no primary serum (step replaced by blocking buffer) with ac signal to study the effect of non-specific binding. These two tests indicated the benefit of ACET stirring (with and
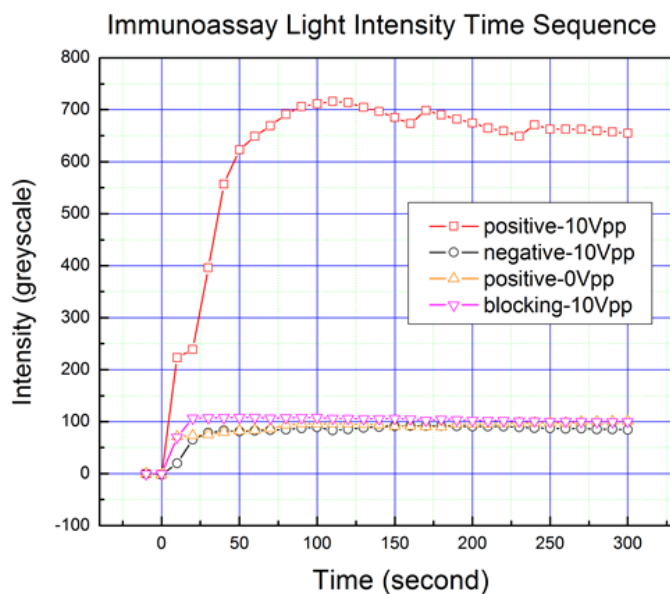
114
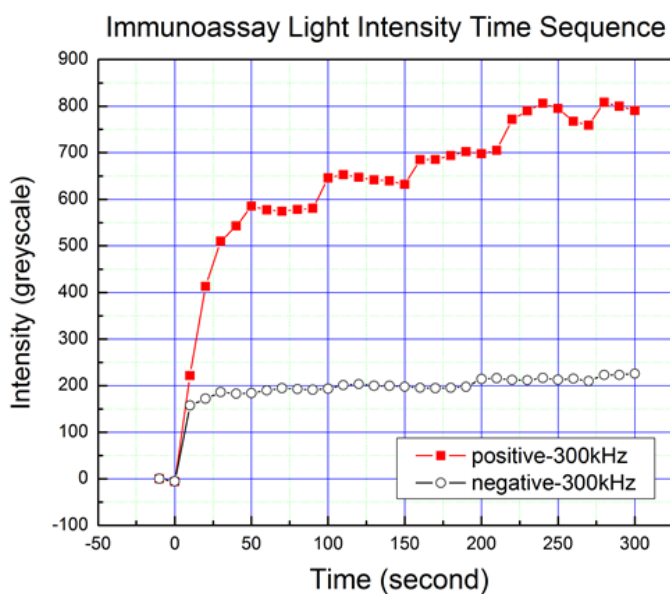
Figure 5-19. Improved immunoassay results with optimized conditions, at (a) 100 kHz and (b) 300 kHz, showing benefit of ACET stirring and reduced nonspecific bindings. Differences between positive and negative samples reached 6x and 4x, respectively.

115

without signal), and reduced non-specific binding of 2nd antibody (with and without serum). With diluted concentration of 2nd antibody, saturation time moved from 20 seconds to around 50 seconds. In the first 50 seconds (before saturation), intensity increased linearly, similar to simulation prediction (see figure 4-3 in chapter 4), indicating intensity change was mainly caused by the binding reaction on surface. After 50 seconds, there were some fluctuation in the curves and this could be caused by photobleaching or autofluorescence phenomena.

5.6.3. Understanding ac voltage effect on immunoassay

For all the immunoassay tests, ac voltage applied to electrodes was 10 V_{pp} (converts to 3.5 V_{rms}). There are detailed discussions in chapter four on how voltage affects preconcentration through numerical study. ACET effect originates from Joule heating in the fluid bulk and scales with 4th power with applied voltage (Equation (11) in chapter three). The higher the applied ac voltage, the stronger the vortices generated in fluid, enhancing the transport of target molecules towards reaction sites.

A voltage sweep test was performed to study its impact on immunoassay binding. From the optimized immunoassay conditions, the binding of 2nd antibody to antigen-antibody pair would saturate within one minute, limited by the least concentrated serum antibodies. So the test was focused in the first 60 seconds after introducing 2nd antibody. Positive serum sample was used for the voltage sweep, because theoretically only the positive serum could bind to antigen, and then induce 2nd antibody binding. Figure 5-20 and 5-21 present the test results from voltage sweep.

116
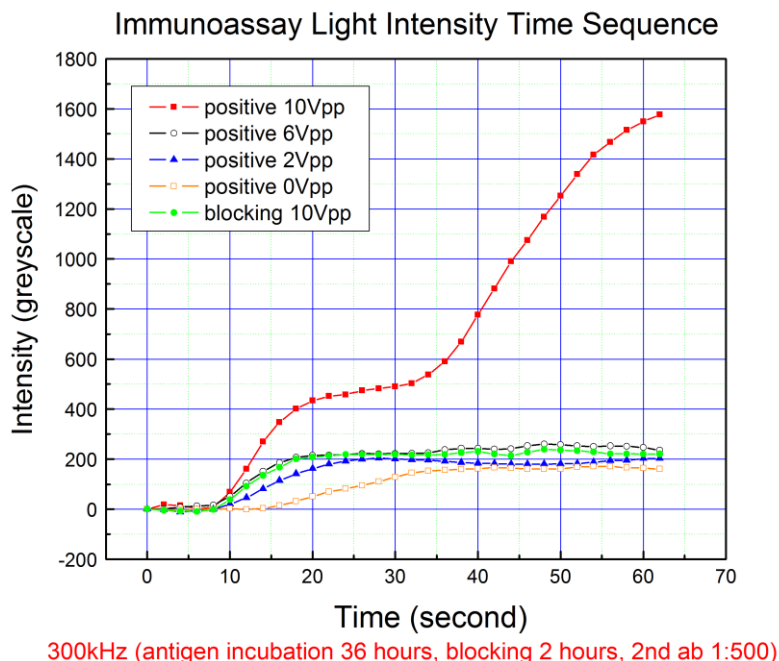
Figure 5-20. Immunoassay light intensity time sequence with voltage sweep at 300 kHz.

The time sequences of fluorescence intensity for ACET immunoassay light were plot in figure 5-20, with applied voltages of 10 Vpp, 6 Vpp, 2 Vpp, 0 Vpp, as well as a control test (blocking buffer instead of serum at 10 Vpp). Each data point was acquired every 5 seconds, and intensity was calculated by averaging over a 696x520 pixel image. Again, background noise intensity was subtracted, so all curves started from 0. It took roughly 10 seconds (between 5 and 10) for the target molecules to be pumped from reservoir inlet to reaction sites. So the light intensity remained unchanged for all curves in the first 10 seconds. Once the 2nd antibody molecules reached the active electrode areas, ACET effect started to influence binding. Higher AC voltage (10 Vpp) would result in higher light intensity response. As expected, light intensity increased

117

less quickly with reduced ac voltage (6 Vpp and 2 Vpp). The 0 Vpp case is equivalent to the transport and reaction processes by pressure driven flow and pure diffusion, and it showed much less intensity increase. In the control test, blocking buffer was used to replace positive serum and it showed how much non-specific binding contributed to final intensity. From the plot, it can be seen that at AC voltage up to 6 Vpp, there is not sufficient binding event to differentiate the positive and negative primary antibodies. Positive 10 Vpp curve reaches a small plateau at 20 seconds, which can be explained by transport limited reaction from simulation discussed in chapter four. Before saturation, each curve exhibited linear intensity increase, which agreed well with numerical simulation predictions and first-order reaction assumption.

Figure 5-20 focused on the first 60 seconds before intensity saturation. And figure 5-21 showed light intensity measured after 3 minutes of introducing 2nd antibody. Background noise was subtracted so all curves showed net increase by ACET effect or pressure driven diffusion (for control test). With 3 minutes of ACET stirring, 10 Vpp gave an increase of 1326, about 5.4x the intensity of 0 Vpp (245). 10 Vpp control curve had intensity of 218, indicating reduced noise level of nonspecific binding with optimized conditions. The benefit of ACET has been justified by the immunoassay experiments.

Numerical simulation has showed a 9x increase in preconcentration binding at 10 Vrms, and in experiments, 3.54 Vrms ac signal can give an increase factor of 5.4. There are differences between simulation and immunoassay tests, such as sample concentration, molecule diffusivity, and fluid conductivity. Increasing the ac voltage

118
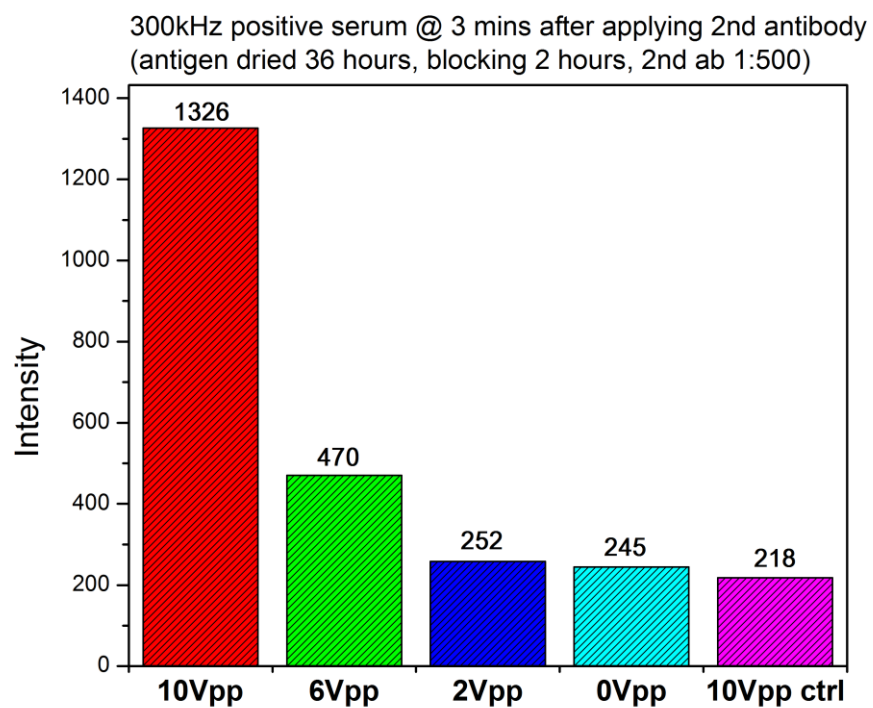
Figure 5-21. Immunoassay light intensity after 3 minutes with voltage sweep at 300 kHz.

above 10 Vpp would exert stronger guiding force in fluid, and the benefit of ACET effect can be greater. However, this could also increase the nonspecific binding. Also power consumption should be an important consideration for the design of portable devices. 10 Vpp (3.54 Vrms) can be easily realized by a Lithium-Ion battery of 3.7 V commonly used in cell phone with a dc to ac converter. So 10 Vpp ac signal would be enough in immunoassay to tell disease status while keep power consumption low.

5.7 Conclusions

In this chapter, development of an ACEK enhanced immunoassay lab-chip for accelerated diagnosis is discussed in detail. With the help of ACET electrodes for micropumping and mixing, the disease status can be determined within minutes, instead of hours of incubation by conventional procedures. Preliminary results showed the feasibility of using ACEK to enhance immunoassay process and further optimizations were performed to better differentiate different samples. The experimental results obtained agreed well with numerical simulation and theoretical predictions. The design of immunoassay lab-chip has contributed to a comprehensive understanding of how ACET flow can affect the biomolecule transport and concentration.

Chapter Six: Conclusions and Future work

6.1 Conclusions of this research work

In this dissertation, the emerging ACET technology is used to enhance the pumping and trapping of micro/nano-particles in high conductive solutions for microfluidic devices. Numerical study on preconcentration has provided the insight and understanding on how binding of particles to specific sensor location is impacted by microchannel and electrode geometry, signal potential and frequency, flow rate, as well as molecule diffusivity. The sensitivity enhancement is independent of the specific type of sensing method used, so numerical optimization can serve as a guide line for future sensor design. An ACET enhanced immunoassay lab-chip was designed for Johne's disease detection in this research work. Rapid and sensitive nanoparticle detection is achieved by employing ACET electrode patterns for fast pumping and effective mixing of flows with target particles. Detection time for determining disease status has reduced to a few minutes instead of hours, and this enables fast diagnostics with improved sensitivity. Microfluidic immunoassay enhanced by AC electrokinetics would greatly reduce sample consumption (in a few μL), waste generation, and reduce cost per analysis (2nd antibody is very expensive) and save labor work, making it possible for point-of care diagnostics applications that require portability and automation.

This research work has contributed to the advancement of microfluidic preconcentration design and how ACEK technology can affect biomolecule transport

and biosening mechanisms in microfluidics. More research work remains to be done to further optimize the current design for a more mature commercial product.

6.2 Future work

6.2.1 Multi-disease detection in a single channel

Current research work can be extended further in many aspects. One of the directions is to achieve multi-disease detection in a single channel. In chapter five, an immunoassay lab-chip was designed for the determination of Johne's disease status in cattle. The immunoassay chip used ACET effect to enhance molecule transport and antigen antibody bindings. It is universal as long as other disease antigen and antibody are available. So a multi-disease detection in a single channel is proposed, as shown in figure 6-1(a). Instead of coating only one type of antigen in the reaction channel, five different antigens are coated in the channel, with some distance apart. It follows the same procedure as one disease detection chip. This method takes advantage of immunoassay's highly selective binding characteristics. With a single run of test, multi-disease status can be determined. It can save cost and time, improving efficiency of work. In the immunoassay test for Johnes' disease, five locations in the reaction channel were monitored, and there were very little variance in intensity, indicating the feasibility of multi-disease detections.

6.2.2 Flow control optimization and automation

The layout of flow control channels was not optimized in the first design of

(a)

antibody

antigen A   antigen B   antigen C   antigen D   antigen E

1159.7   1206.7   1148.6   1161.6   1187.6

(b)   positive serum, 250 kHz, 10 Vpp, average intensity 1172.8
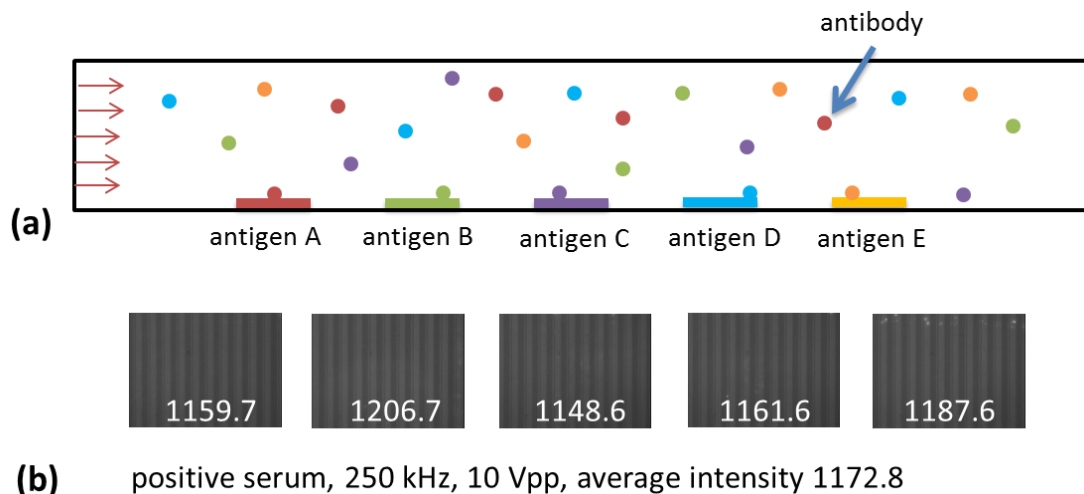
Figure 6-1. Multi-disease detection in a single channel with immunoassay. (a) Conceptual schematic of multiple antigen coating and antibody binding in the channel. (b) Uniform intensity distribution through the channel (5 locations as illustrated in (a)) for Johne's disease immunoassay.

immunoassay chip (figure 5-5). The areas of the reservoirs are too small so the natural pressure driven flow will be strong, making it hard to control the dispensing of each reagent separately and sequentially. In order to reduce natural flow by make pumping channel longer and reservoir wider, a new way to arrange pumping electrodes and microchannel is proposed, as shown in figure 6-2. The old straight line layout of channel will take up a lot of space, leaving small areas for reservoirs. The new design will use the c. In this way, channel can be longer for increased flow resistance, while leaving more space on the side for larger reservoirs. At the same time, pumping electrodes need to be rearranged so the pumping direction is always from narrow to wide electrodes, accommodating ACET pumping effect.

123

5/5/25/25 electrode configuration
Pumping direction: narrow->wide
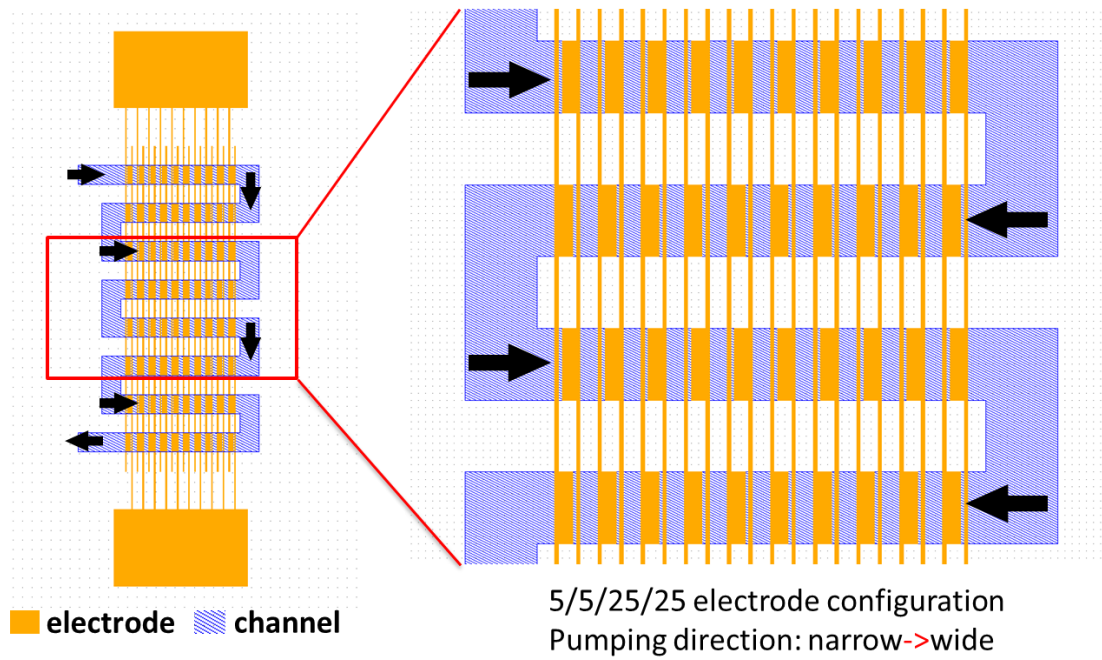
electrode ▨ channel

Figure 6-2. New flow control unit design of serpentine shape for microchannel to save space and leave more area for reservoir. The electrode patterns are modified to accommodate ACET pumping effect.

With the optimization of immunoassay reaction and flow control designs, a portable immunoassay lab-on-a-chip device for accelerated diagnosis is conceived, as shown in figure 6-3. When the pre-coated chip is inserted in position, the battery powered immunoassay device electrically controls reagent delivery, enhanced reaction, and washing processes. Light detection module based on LED optical system is embedded for real time data collection and read out. The device is portable and energy efficient. The disease status can be determined in minutes in field, instead of hours back in biological labs.
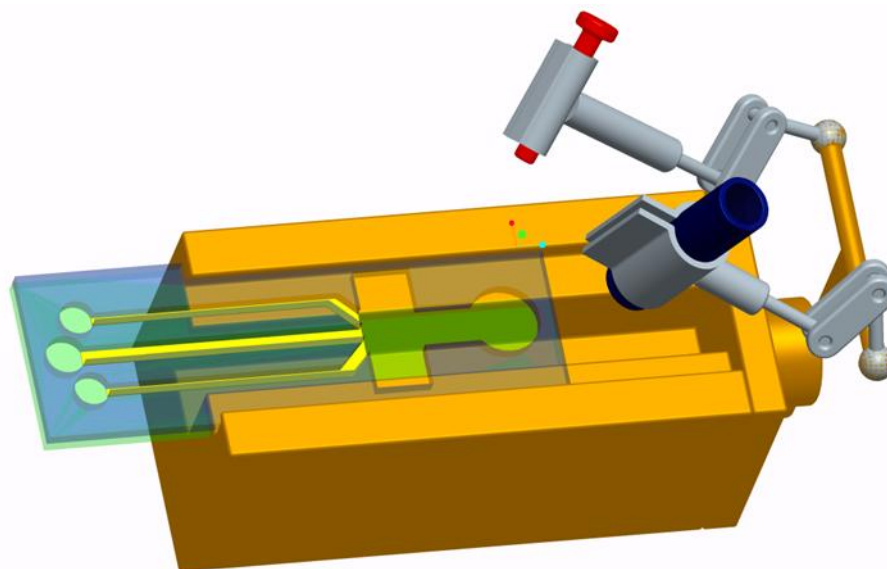
Figure 6-3. Conceived fully automated immunoassay lab-on-a-chip device for accelerated diagnosis.

LIST OF REFERENCES

Chapter One:

[1] S. Choi, M. Coryll, LY Sin, P.K. Wong, and J. Chae, Microfluidic-based biosensors toward point-of-care detection of nucleic acids and proteins, Microfluidics and Nanofluidics, Volume 10, Number 2, 231-247, 2011

[2] Z. Li, Y. Chen, X. Li, T. I. Kamins, K. Nauka, and R. S. Williams, Sequence-specific label-free DNA sensors based on silicon nanowires, NANO Letters, 2004, 4 (2), 245-247.

[3] P. E. Sheehan, and L. J. Whitman, Detection Limits for Nanoscale Biosensors, Nano Lett., 2005, 5 (4), 803-807.

[4] D. R. Kim and XL. Zheng, Numerical Characterization and Optimization of the Microfluidics for Nanowire Biosensors, Nano Lett., 2008, 8 (10), pp 3233-3237.

[5] T. M. Squires, R. J. Messinger, and S. R. Manalis, Making it stick: convection, reaction and diffusion in surface-based biosensors, Nature Biotechnology 26, 417- 426 (2008)

[6] M. Lian, N. Islam and J. Wu, AC electrothermal manipulation of conductive fluids and particles for lab-chip applications, IET Nanobiotechnology 2007; 1(3): 36-43.

[7] H. C. Feldman, M. Sigurdson and C. D. Meinhart, AC electrothermal enhancement of heterogeneous assays in microfluidics, Lab Chip, 2007, 7, 1553–1559.

[8] M. Sigurdson, D. Wang and C. D. Meinhart, Electrothermal stirring for heterogeneous immunoassays, Lab Chip, 2005, 5, 1366-1373

[9] K.R. Huang, JS. Chang, S. D. Chao, KC Wu, CK. Yang, CY. Lai, and SH. Chen, Simulation on binding efficiency of immunoassay for a biosensor with applying electrothermal effect, J. Appl. Phys. 104, 064702, (2008).

[10] K. Yang and J. Wu, In situ Electrokinetic Preconcentrator for Conductive Biofluids, ASME 2nd Micro/Nanoscale Heat & Mass Transfer Int'l Conf., Dec. 18-21, 2009.

[11] K. Yang and J. Wu, Numerical Study of In Situ Preconcentration for Rapid and Sensitive Nanoparticle Detection, Biomicrofluidics, 4, 034106 (2010)

[12] M. A. Burns, B. N. Johnson, S. N. Brahmasandra, K. Handique, J. R. Webster, M. Krishnan, T. S. Sammarco, P. M. Man, D. Jones, D. Heldsinger, C. H. Mastrangelo, and D. T. Burke, An Integrated Nanoliter DNA Analysis Device, Science 16 October 1998, Vol. 282. no. 5388, pp. 484 – 487

[13] Y. Gao, G. Hu, F. Y. H. Lin, P. M. Sherman and D. Li, An Electrokinetically-Controlled Immunoassay for Simultaneous Detection of Multiple Microbial Antigens, Biomedical Microdevices, Volume 7, Number 4, 301-312, 2005

[14] Q. Xiang, G. Hu, Y. Gao, and D. Li, Miniaturized immunoassay microfluidic system with electrokinetic control, Biosensors and Bioelectronics, 21 (2006), Pages 2006-2009

[15] Y. Gao, F. Y.H. Lin, G. Hu, P. M. Sherman, and D. Li, Development of a novel electrokinetically driven microfluidic immunoassay for the detection of Helicobacter pylori, Analytica Chimica Acta 543 (2005) 109-116

127

Chapter Two:

[1] A. Ashkin, J. M. Dziedzic, J. E. Bjorkholm, and S. Chu, Observation of a single-beam gradient force optical trap for dielectric particles, Opt. Lett. 11, 288-290 (1986)

[2] D. G. Grier, A revolution in optical manipulation, Nature 424, 810–816 (2003)

[3] K. C. Neuman and S. M. Block, Optical trapping, Rev. Sci. Instrum. 75, 2787 (2004)

[4] A. H. J. Yang, S. D. Moore, B. S. Schmidt, M. Klug, M. Lipson, and D. Erickson, Optical manipulation of nanoparticles and biomolecules in sub-wavelength slot waveguides, ibid. 457, 71 (2009)

[5] P. Y. Chiou, A. T. Ohta, and M. C. Wu, Massively parallel manipulation of single cells and microparticles using optical images, Nature 436, 370-372, (2005)

[6] C. Gosse and V. Croquette, Magnetic Tweezers: Micromanipulation and Force Measurement at the Molecular Level, Biophys. J. 82, 3314 (2002)

[7] H. Lee, A. M. Purdon, and R. M. Westervelt, Manipulation of biological cells using a microelectromagnet matrix, Appl. Phys. Lett. 85, 1063 (2004)

[8] J. Yan, D. Skoko, and J. F. Marko, Near-field-magnetic-tweezer manipulation of single DNA molecules, Phys. Rev. E 70, 011905 (2004)

[9] H. M. Hertz, Standing‐wave acoustic trap for nonintrusive positioning of microparticles, J. Appl. Phys. 78, 4845 (1995)

[10] M. Evander, L. Johansson, T. Lilliehorn, J. Piskur, M. Lindvall, S. Johansson, M. Almqvist, T. Laurell, and J. Nilsson, Noninvasive Acoustic Cell Trapping in a Microfluidic Perfusion System for Online Bioassays, Anal. Chem. 79, 2984 (2007)

[11] H. M. Hertz, Standing‑wave acoustic trap for nonintrusive positioning of microparticles, J. Appl. Phys. 78, 4845 (1995)

[12] M. Evander, L. Johansson, T. Lilliehorn, J. Piskur, M. Lindvall, S. Johansson, M. Almqvist, T. Laurell, and J. Nilsson, Noninvasive Acoustic Cell Trapping in a Microfluidic Perfusion System for Online Bioassays, Anal. Chem. 79, 2984 (2007)

[13] B. R. Lutz, J. Chen, and D. T. Schwartz, Hydrodynamic Tweezers: 1. Noncontact Trapping of Single Cells Using Steady Streaming Microeddies, Anal. Chem. 78, 5429 (2006)

[14] C. M. Lin, Y. S. Lai, H. P. Liu, C. Y. Chen, and A. M. Wo, Trapping of Bioparticles via Microvortices in a Microfluidic Device for Bioassay Applications, ibid. 80, 8937 (2008)

[15] M. Tanyeri, E. M. Johnson-Chavarria, and C. M. Schroeder, Hydrodynamic trap for single particles and cells, Appl. Phys. Lett. 96, 224101 (2010)

[16] D. Di Carlo, L. Y. Wu, and L. P. Lee, Dynamic single cell culture array, Lab Chip 6, 1445 (2006)

[17] A. M. Skelley, O. Kirak, H. Suh, R. Jaenisch, and J. Voldman, Microfluidic control of cell pairing and fusion, Nat. Methods 6, 147 (2009)

[18] W. H. Tan and S. Takeuchi, A trap-and-release integrated microfluidic system for dynamic microarray applications, Proc. Natl. Acad. Sci. U.S.A. 104, 1146 (2007)

[19] J. Khandurina, T. E. McKnight, S. C. Jacobson, L. C. Waters, R. S. Foote, and J. M. Ramsey, Integrated system for rapid PCR-Based DNA analysis in microfluidic devices, Anal. Chem. 2000, 72 (13), 2995–3000

[20] B. Jung, R. Bharadwaj, and J. G. Santiago, Thousand-fold Signal Increase using Field Amplified Sample Stacking for On-Chip Electrophoresis, Electrophoresis, 2003, 24(19-20), 3476-3483

[21] N. P. Beard, C.X. Zhang, and A. J. DeMelloIn, column field-amplified sample stacking of biogenic amines on microfabricated electrophoresis devices, Electrophoresis, 24, 732-739

[22] H. Yang and R.L. Chien, Sample stacking in laboratory-on-a-chip devices, J. Chromatogr A, 2001, 924(1-2), 155-63

[23] P. H. Humble, R. T. Kelly, A. T. Woolley, H. D. Tolley, and M. L. Lee, Electric Field Gradient Focusing of Proteins Based on Shaped Ionically Conductive Acrylic Polymer, Anal. Chem. 2004, 76(19), 5641–5648

[24] B. Jung, Y. Zhu, and J. G. Santiago, Detection of 100 aM Fluorophores Using a High-Sensitivity On-Chip CE System and Transient Isotachophoresis, Anal. Chem. 2007, 79 (1), 345–349

[25] A. E. Cohen and W. E. Moerner, Method for trapping and manipulating nanoscale objects in solution, Appl. Phys. Lett. 86, 093109 (2005)

[26] A. E. Cohen, Control of Nanoparticles with Arbitrary Two-Dimensional Force Fields, Phys. Rev. Lett. 94, 118102 (2005)

[27] M. D. Armani, S. V. Chaudhary, R. Probst, and B. Shapiro, Using feedback control of microflows to independently steer multiple particles, J. Microelectromech. Syst. 15, 945 (2006)

[28] N. G. Green, A. Ramos, and H. Morgan, Ac electrokinetics: a survey of sub-

micrometre particle dynamics, J. Phys. D: Appl. Phys. 33 632 (2000)

[29] R. Pethig, Dielectrophoresis of Biological Cells, Encyclopedia of Surface and Colloid Science, Pp. 1719-1736, 2006, Taylor & Francis

[30] H. Li, and R. Bashir, Dielectrophoretic separation and manipulation of live and heat-treated cells of Listeria on microfabricated devices with interdigitated electrodes, Sensors and actuators B 86 (2002) 215-221

[31] D. J. Bakewell, and H. Morgan, Dielectrophoresis of DNA: time- and frequency-dependent collections on microelectrodes, IEEE Trans Nanobioscience. 2006 Mar;5(1):1-8

[32] N. Markarian, M. Yeksel, B. Khusid, and K. Farmer, Limitations on the scale of an electrode array for trapping particles in microfluidics by positive dielectrophoresis, Appl. Phys. Lett. 82, 4839 (2003)

[33] A. R. Minerick, R. Zhou, P. Takhistov, and H.-C. Chang, Manipulation and characterization of red blood cells with alternating current fields in microdevices, Electrophoresis 2003, 24, 3703-3717

[34] H.-C. Chang, Electro-Kinetics: A Viable Micro-Fluidic Platform for Miniature Diagnostic Kits, the Canadian Journal of Chemical Engineering, volume 84, APRIL 2006

[35] H. Morgan, D. Holmes, and N.G. Green, 3D focusing of nanoparticles in microfluidic channels, IEE Proc.-Nanobiotechnol. Vol. 150, No. 2, November 2003

[36] J. Suehiro and R. Pethig, The dielectrophoretic movement and positioning of a biological cell using a three-dimensional grid electrode system, J. Phys. D: Appl. Phys.

31 (1998) 3298-3305

[37] PK. Wong, CY. Chen, TH. Wang and CM. Ho, Electrokinetic bioprocessor for concentrating cells and molecules, Analytical Chemistry 2004; 76 (23): 6908-6914

[38] J. Wu, Biased AC electro-osmosis for on-chip bioparticle processing, IEEE Trans Nanotech, VOL. 5, NO. 2, MARCH 2006

[39] J. Wu, Y. Ben, D. Battigelli, and H.-C. Chang, Long-Range AC Electroosmotic Trapping and Detection of Bioparticles, Industr. Eng. Chem. Research, 2005, 44(8), pp. 2815 – 2822

[40] N. Islam and J. Wu, Microfluidic Transport by AC Electroosmosis, Journal of Physics: Conference Series 34 (2006) 356–361

[41] K. H. Bhatt, S. Grego, and O. D. Velev, An AC electrokinetic technique for collection and concentration of particles and cells on patterned electrodes, Langmuir 2005; 21 (14): 6603-6612

[42] M. Lian, N. Islam and J. Wu, AC electrothermal manipulation of conductive fluids and particles for lab-chip applications, IET Nanobiotechnology 2007; 1(3): 36-43

[43] N. Islam, M. Lian, and J. Wu, Enhancing Cantilever Capability with Integrated AC Electrokinetic Trapping Mechanism, J. Microfluidics & Nanofluidics, 2007, 3(3), pp. 369-375

[44] J. Wu and N. Islam, A Simple Method to Integrate In Situ Nano-Particle Focusing With Cantilever Detection, IEEE Sensors Letters, 7(6), pp. 957-958, 2007

[45] D. Holmes, N. G. Green, and H. Morgan, Microdevices for Dielectrophoretic Flow-Through Cell Separation, IEEE Eng Med Biol Mag. 2003 Nov-Dec;22(6):85-90

[46] T. Müller, G. Gradl, S. Howitz, S. Shirley, Th. Schnelle, and G. Fuhr, A 3-D microelectrode system for handling and caging single cells and particles, Biosensors and Bioelectronics 14 (1999) 247-256

[47] K. F. Hoettges, M. P. Hughes, A. cotton, N. A. Hopkins, and M. B. McDonnell, Optimizing particle collection for enhanced surface-based biosensors, IEEE Eng Med Biol Mag. 2003 Nov-Dec;22(6):68-74

[48] M. R. Brown and C. D. Meinhart, AC electroosmotic flow in a DNA concentrator, Microfluid Nanofluid (2006) 2: 513–523

[49] Z. Gagnon and H.-C. Chang, Aligning fast alternating current electroosmotic flow fields and characteristic frequencies with dielectrophoretic traps to achieve rapid bacteria detection, Electrophoresis 2005, 26, 3725–3737

[50] J.R. Du, Y.J. Juang, J.T. Wu, and H.H. Wei, Long-range and superfast trapping of DNA molecules in an ac electrokinetic funnel, Biomicrofluidics 2, 044103 (2008)

[51] P. Pham, I. Texier, A.-S. Larrea, R. Blanc, F. Revol-Cavalier, H. Grateau, F. Perraut, Numerical design of a 3-D microsystem for bioparticle dielectrophoresis: The Pyramidal Microdevice, J. Electrostatics 65 (2007) 511-520

[52] S. Park, M. Koklu, and A. Beskok, Particle Trapping in High-Conductivity Media with Electrothermally Enhanced Negative Dielectrophoresis, Anal. Chem. 2009, 81 (6), pp 2303–2310

[53] H. C. Feldman, M. Sigurdson and C. D. Meinhart, AC electrothermal enhancement of heterogeneous assays in microfluidics, Lab Chip, 2007, 7, 1553–1559

[54] Z. Gagnon, J. Mazur, and H.-C. Chang, Integrated AC electrokinetic cell

separation in a closed-loop device, Lab Chip, 2010, 10, 718-726

[55] J. A. Wood, B. Zhang, M. R. Tomkins, and A. Docoslis, Numerical investigation of AC electrokinetic virus trapping inside high ionic strength media, Microfluid Nanofluid (2007) 3:547–560

Chapter Three:

[1] H. Morgan and N. G. Green, AC Electrokinetics: Colloids and Nanoparticles

[2] A. Ramos, H. Morgan, N. G. Green, and A. Castellanos, Ac electrokinetics: a review of forces in microelectrode structures, J. Phys. D: Appl. Phys. 31 (1998) 2338-2353

[3] J. Wu, Interactions of Electrical Fields with Fluids: Laboratory-on-a-chip Applications, IET Nanobiotechnology, 2(1), pp. 14–27, 2008.

[4] N. Islam and J. Wu, Microfluidic Transport by AC Electroosmosis, Journal of Physics: Conference Series 34 (2006) 356–361

[5] J. Wu, Y. Ben, and H.-C. Chang, Particle detection by electrical impedance spectroscopy with asymmetric-polarization AC electroosmotic trapping, Microfluid Nanofluid (2005) 1: 161–167

[6] Pohl, H. A. (1978) Dielectrophoresis, Cambridge University Press, Cambridge

[7] R. Pethig, Dielectrophoresis of Biological Cells, Encyclopedia of Surface and Colloid Science, Pp. 1719-1736, 2006, Taylor & Francis

[8] P. R. C. Gascoyne and J. V. Vykoukal, Dielectrophoresis-Based Sample Handling in General-Purpose Programmable Diagnostic Instruments, Proc IEEE Inst Electr Electron Eng. 2004 Jan 1;92(1):22-42

[9] R. Pethig, Dielectrophoresis: Status of the theory, technology, and applications, Biomicrofluidics 4, 022811 (2010)

[10] N.G. Green, A. Ramos and H. Morgan, AC electrokinetics: a survey of sub-micrometer particle dynamics, J. Phys. D: Appl. Phys. 33 (2000), pp. 632–641

[11] A. Ramos, H. Morgan, N. G. Green, and A. Castellanos, Ac electrokinetics: a review of forces in microelectrode structures, J. Phys. D: Appl. Phys. 31 (1998) 2338-2353

[12] A. Castellanos, A. Ramos, A. González, N.G. Green, and H. Morgan, Electrohydrodynamics and dielectrophoresis in microsystems: scaling laws, J. Phys. D: Appl. Phys. 36 (2003) 2584-2597

Chapter Four:

[1] T. Gervais and K. F. Jensen, Mass transport and surface reactions in microfluidic systems, Chem. Eng. Sci. 61 (2006) 1102-1121.

[2] K. Pappaert, P. Van Hummelen, J. Vanderhoeven, G. V. Baron, and G. Desmet, Diffusionreaction modelling of DNA hybridization kinetics on biochips, Chem. Eng. Sci. 58 (2003) 4921-4930.

[3] K. Yang and J. Wu, Numerical Study of In Situ Preconcentration for Rapid and Sensitive Nanoparticle Detection, Biomicrofluidics, 4, 034106 (2010)

Chapter Five:

[1] Wild D (2008) The immunoassay handbook. 3rd edn. Elsevier, Oxford

[2] Q. Xiang, G. Hu, Y.Gao, D. Li, Miniaturized immunoassay microfluidic system with electrokinetic control, Biosensors and Bioelectronics. 21 (10) (2005) 2006-2009.

[3] A. Bange, H.B. Halsall, W. R. Heineman, Microfluidic immunosensor systems, Biosensors and Bioelectronics. 20 (12) (2005) 2488-2503.

[4] W. G. Lee, Y. G. Kim, B. G. Chung, U. Demirci, A. Khademhosseini, Nano/Microfluidics for diagnosis of infectious diseases in developing countries, Advanced Drug Delivery Reviews. 62 (4-5) (2010) 449-457.

[5] C. C. Lin, J. H. Wang, H. W. Wu, G. B. Lee, Microfluidic Immunoassays, Journal of the Association for Laboratory Automation. 15 (3) (2010) 153-274.

[6] A. Hatch , A. E. Kamholz , K. R. Hawkins , M. S. Munson , E. A. Schilling , B. H. Weigl and P. Yager, A rapid diffusion immunoassay in a T-sensor, Nature Biotechnology 19, 461–465 (1 May 2001)

[7] T.-K. Lim, H. Ohta, and T. Matsunaga, Microfabricated On-Chip-Type Electrochemical Flow Immunoassay System for the Detection of Histamine Released in Whole Blood Samples, Anal. Chem., 2003, 75 (14), pp 3316–3321

[8] S. Thorslund, O. Klett, F. Nikolajeff, K. Markides and J. Bergquist, A hybrid poly (dimethylsiloxane) microsystem for on-chip whole blood filtration optimized for steroid screening. Biomedical Microdevices, Volume 8, Number 1, 73-79, 2006

[9] B. S. Lee, J.-N. Lee, J.-M. Park, J.-G. Lee, S. Kim, Y.-K. Cho and C. Ko, A fully automated immunoassay from whole blood on a disc, Lab Chip, 2009, 9, 1548-1555

[10] J. Kong, L. Jiang, X. Su, J. Qin, Y. Du and B. Lin, Integrated microfluidic immunoassay for the rapid determination of clenbuterol, Lab Chip, 2009, 9, 1541-1547

[11] H. Huang, X. Zheng, J. Zheng, J. Pan and X. Pu, Rapid analysis of alpha-fetoprotein by chemiluminescence microfluidic immunoassay system based on super-paramagnetic microbeads, Biomedical Microdevices, Volume 11, Number 1, 213-216, 2009

[12] T. G. Henares, S.-I. Funano, S. Terabe, F. Mizutani, R. Sekizawa, H. Hisamoto, Multiple enzyme linked immunosorbent assay system on a capillary-assembled microchip integrating valving and immunoreactions functions, Analytica Chimica Acta (2007), Volume: 589, Issue: 2, Pages: 173-179

[13] D. R. Shankaran, N. Miura, Trends in interfacial design for surface plasmon resonance based immunoassays. J Phys D Appl Phys Volume: 40, Issue: 23, 2007

[14] W. Laiwattanapaisal, T. Songjaroen, T. Maturos, T. Lomas, A. Sappat, A. Tuantranont, On-chip immunoassay for determination of urinary albumin, Sensors 2009, 9, 10066-10079

[15] S. J. Yoo, Y. B. Choi, J. II Ju, G.-S. Tae, H. H. Kim and S.-H. Lee, Microfluidic chip-based electrochemical immunoassay for hippuric acid, Analyst, 2009, 134, 2462-2467

[16] T. Frisk, N. Sandström, L. Eng, W. Wijngaart, P. Månsson and G. Stemme, An integrated QCM-based narcotics sensing microsystem, Lab Chip, 2008, 8, 1648-1657

[17] H. Jiang, X. Weng and D. Li, Microfluidic whole –blood immunoassays, Microfluid Nanofluid, Volume 10, Number 5, 941-964, 2011

VITA

Kai Yang was born in Zhangjiagang, a small town along east coast of Jiangsu Province, People's Republic of China (PRC). He was admitted to Shanghai Jiao Tong University (SJTU) after graduation from high school in 2001 and received Bachelor of Engineering degree in Electronics Science and Technology in 2005. He came to the US in 2006 to persue graduate degree at the University of Tennessee, Knoxville and received Master of Science degree in May, 2008, and Doctor of Philosophy degree in August, 2011, both in Electrical Engineering. His research interests include: design and fabrication of microfluidic devices using ACEK technique to manipulate micro/nano-sized particles for transportation, concentraton, separation, and detection; optimizing designs using computer simulation modeling; biosensor and immunosensor design for portable devices and lab-on-a-chip applications.